Flinders University
School of Computer Science, Engineering and Mathematics

DESIGN AND THERMAL SIMULATION OF AN ENERGY STORAGE SYSTEM FOR FLINDERS UNIVERSITY'S SOLAR ELECTRIC VEHICLE

By

ALLAN MANKAVIL

A thesis submitted for the degree of Bachelor of Engineering (Robotics) (Honours) and Master of Engineering (Electronics)

Project Supervisors
Dr. Vlatka Zivotic-Kukolj
Dr. Stuart Wildy

October, 2016

Submitted to the School of Computer Science, Engineering, and Mathematics in the Faculty of Science and Engineering in partial fulfilment of the requirements for the degree of Bachelor of Engineering (Robotics) (Honours) and Master of Engineering (Electronics) at Flinders University - Adelaide Australia.

DECLARATION OF ORIGINALITY

I certify that this work does not incorporate without acknowledgment any material previously submitted for a degree or diploma in any university; and that to the best of my knowledge and belief it does not contain any material previously published or written by another person except where due reference is made in the text.

Signed: Allan Mankavil **Date:** 17-10-16

ABSTRACT

Flinders University (FU) will be constructing its first ever Solar Electric Vehicle (SEV), to compete within the 2017 World Solar Challenge (WSC). The WSC is a biennial SEV race across 3,022 km from Darwin to Adelaide. A major subsystem of the FU's SEV (FUSEV) is the Energy Storage System (ESS), used to store, monitor, and manage the energy drawn from the grid and solar panels, to power the electrical/electronic systems of the FUSEV. The ESS is composed of various sub-systems such as the Battery Management System (BMS), Battery Charger (BC), and the Battery Array (BARR).

This thesis describes the design and thermal simulation of an ESS for the FUSEV. As part of the design process, a literature review, market study, and competitor analysis was conducted to select the most appropriate and interoperable commercial off-the-shelf products. Following this, the design of FUSEV's BARR composed of 126 lithium-ion 18650 cells was developed. As per the WSC regulations and Australian Design Rules (ADRs) to ensure the safety of FUSEV's occupants, the BARR needs to operate within the manufacturer's recommended temperature range and be contained within an enclosure. As a result of the size constraints imposed by the FUSEV and the decision to implement forced air convection cooling using axial case fans to cool the BARR, an enclosure had to be custom-made. To develop an effective enclosure design, the thermal response of FUSEV's BARR within different types of enclosure designs was simulated using ANSYS Fluent. The results of the thermal analysis, validated through a baseline study revealed that the most optimal enclosure design decreased the cell temperature by 7.20% to 26.10% from its initial temperature. As a result, this design was selected for FUSEV's use.

The 3D models and mechanical drawings of the battery modules, BARR, and ESS enclosure were developed using Autodesk Inventor. To ensure that the ESS enclosure could withstand the crash acceleration as specified within the ADRs, the enclosure was also subjected to finite-element stress analysis using Inventor to ensure no design failures occurred. The work done thus far enables for the project's continuity in the future, through the establishment of an adaptable and modularized ESS design.

ACKNOWLEDGEMENTS

I would like to express sincere gratitude towards my parents for their love and unwavering support during the course of my degree.

The progress I have made within this project thus far was possible thanks to the help provided by members of the project team. In particular, I would like to extend my appreciation towards Anthony Stivahtaris, Steven Park, and Syed Wahb Mehdi for their input during the design and development process.

I would also like to thank all members of the engineering department, particularly Damian Kleiss, and Richard Stanley for providing technical advice during the course of the project. I would also like to thank my supervisors Dr. Stuart Wildy and Dr. Vlatka Zivotic-Kukolj for their guidance and support throughout the project. This opportunity that they have provided me with has allowed me to gain invaluable experience for my future as a practising engineer.

CONTENTS

LIST OF FIGURES

LIST OF TABLES

ACRONYMS AND ABBREVIATIONS

Acronyms/Abbreviations	Full Form/Description
ABS	Acrylonitrile Butadiene Styrene
ACF	Axial Case Fan
ADR	Australian Design Rules
BARR	Battery Array
BC	Battery Charger
BEV	Battery Electric Vehicle
BMS	Battery Management System
CAD	Computer Aided Design
CANBUS	Controller Area Network Bus
CFD	Computational Fluid Dynamics
CMU	Cell Management Unit
COTS	Commercial Off-The-Shelf
CSEM	School of Computer Science, Engineering and Mathematics
DPTI	Department of Planning, Transport and Infrastructure
ECM	Equivalent Circuit Model
ESS	Energy Storage System
EV	Electric Vehicle
FAST	Flinders Automotive Solar Team
FCEV	Fuel Cell Electric Vehicles
FEA	Finite Element Analysis
FEM	Finite Element Method
FU	Flinders University
FUSEV	Flinders University's Solar Electric Vehicle
FVM	Finite Volume Method
GHG	Greenhouse Gases
HEV	Hybrid Electric Vehicle
IC	Internal Combustion
ICVS	Individually Constructed Vehicles Standards
IPCC	Intergovernmental Panel on Climate Change
N/A	Not Applicable/Not Available
PBT	Polybutylene Terephthalate

PHEV	Plug-In Hybrid Electric Vehicle
SA	South Australia
SEV	Solar Electric Vehicle
TMS	Thermal Management System
UN	United Nations
UNFCCC	United Nations Framework Convention on Climate Change
VF	Ventilation Filter
WSC	World Solar Challenge

NOMENCLATURE

Variable/Abbreviation	Definition/Description
$\dot{q}_t$	Rate of internal heat generation per unit volume, $\left(\frac{W}{m^3}\right)$
°C	Degree Celsius
a	Thermal diffusivity, $\left(\frac{m^2}{s}\right)$
A	Surface area of the solid, (m^2)
Bi	Biot Number
C_1	Parallel Capacitor
CH_4	Methane
CO_2	Carbon Dioxide
Cp	Heat capacity of the solid, $\left(\frac{J}{m^3 \cdot K}\right)$
DOD	Depth of Discharge
E_m	Electromotive force of main branch
h	Surface heat transfer coefficient, $\left(\frac{J}{m^2 \cdot K}\right)$
k	Thermal conductivity, $\left(\frac{W}{m \cdot K}\right)$
L_c	Characteristic length (m)
LCM	Lumped Capacitance Model
$LiCoO_2$ / LCO	Lithium Cobalt Oxide
$LiFePO_4$ / LFP	Lithium Iron Phosphate
Li-ion	Lithium Ion
$LiNiCoAlO_2$ / NCR / NCA	Lithium Nickel Cobalt Aluminium Oxide
$LiNiMnCoO_2$ / NMC	Lithium Nickel Manganese Cobalt Oxide
$LiMn_2O_4$ / LMO	Lithium Manganese Oxide
Li-S	Lithium Sulphur
N_2O	Nitrous Oxide
NiCd	Nickel Cadmium
NiMH	Nickel Metal Hydride
p	Mass of the solid, $\left(\frac{kg}{m^3}\right)$
Pa	Pascal
PDE	Partial Differential Equation
Ps	Power dissipated within the cell, (W)

R_0	Series Resistor
R_1	Parallel Resistor
RC	Resistor-Capacitor
RT	Convection Resistance, $\left(\frac{W}{m^2 \cdot K}\right)$
s	Laplace transform variable
S/m	Siemens per meter
SOC	State of Charge
T	Temperature of the solid, (K)
t	Time, (s)
T_a	Ambient temperature, (K)
$T_{S,1}$	Surface temperature of first object, (K)
$T_{S,2}$	Surface temperature of second object, (K)
V	Volume of the solid, (m^3)
x	Spatial direction along x-axis
y	Spatial direction along y-axis

1 INTRODUCTION

Humanity's primordial desire for the freedom of mobility has facilitated the rapid growth of the automotive industry prior to the present technological age [1]. The convenience of personal mobility comes at a hefty price that is the depletion of natural resources, and environmental degradation due to air pollution. The major contributors to air pollution is not only the manufacturing industry, but also automobiles powered by Internal Combustion (IC) engines. These engines burn non-renewable resources like petroleum and natural gas to generate energy [2-5]. Greenhouse Gases (GHG) such as, Carbon Dioxide (CO_2), Methane (CH_4), and Nitrous Oxide (N_2O) are emitted by these automobiles as a by-product of the combustion process [6-8]. CO_2 is known to be a major cause of global warming, as it is the most prevalent of the GHG as shown in Figure 1-1 [7]. Global warming is the phenomenon where the average global temperature rose by 1.1 °C over the past century, and is projected to rise another 0.3 °C to 4.8 °C over the next century. Fluctuations in the average global temperature could contribute to the on-going natural planetary cycle-life which can translate to large and potentially dangerous shifts in climate, thus endangering all life on Earth [9].

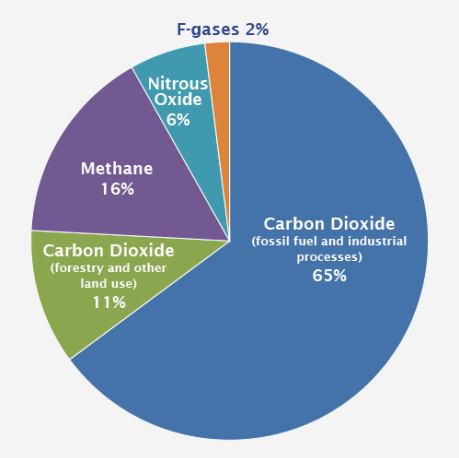

Figure 1-1. Intergovernmental Panel on Climate Change's (IPCC) estimates of global GHG emissions in 2010 [7].

This is of concern as global CO_2 emissions from fossil fuels has increased significantly since 1900 as shown in Figure 1-2 [7]. This can be attributed to the global population growth that occurred from 1900 to 2000, during which the population grew from 1.6 billion to 6.1 billion people. Though the rate of population growth is now receding, the United Nations (UN) predicts that the population is likely to exceed 8 billion people by 2030. It is projected that this increase in population would result in there being over two billion vehicles active on the roads by 2050 [10]. Consequently, the GHG emissions of transportation accounting for almost 14% of global GHG emissions, is expected to double by 2050 [7]. To diverge from the impending catastrophe, global emissions of GHG especially that of industrialized countries needs to be reduced by 50-80%, below the CO_2 levels in 1990s. It is expected that this would enable countries within the United Nations Framework Convention on Climate Change (UNFCCC) to meet their global objective of containing the average global temperature increase to 2 °C by 2050, through reliance on low-carbon energy resources [11].

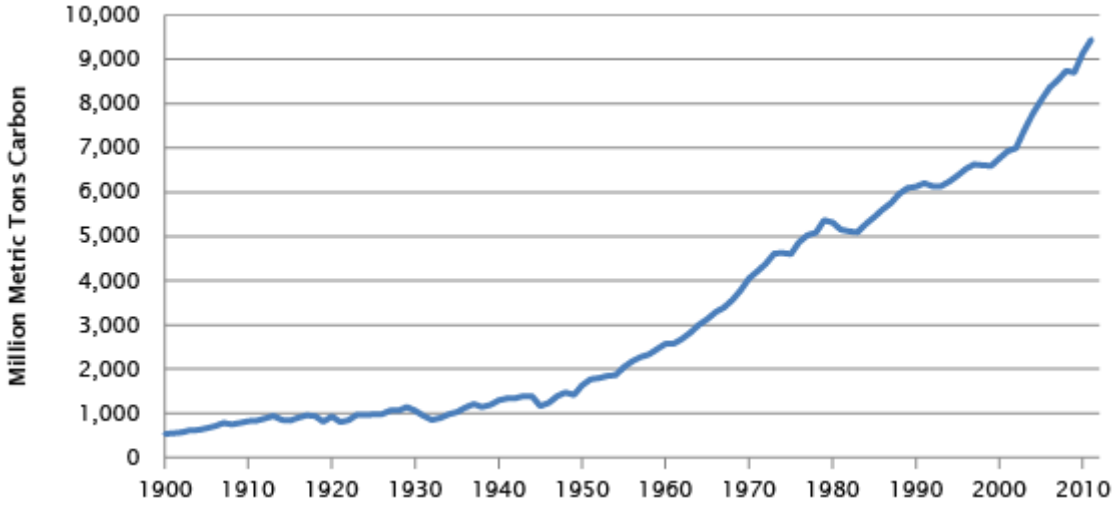

Figure 1-2. U.S. Department of Energy's previous estimate of global fossil-fuel carbon emissions from 1900-2011 [7].

Worldwide, concerns of governments and industries regarding global warming has reignited the automotive industry's interest in developing low-carbon technologies that enable sustainable transportation. This has resulted in the commercial introduction of a variety of Electric Vehicles (EVs) such as Hybrid Electric Vehicles (HEV), Plug-In Hybrid Electric Vehicles (PHEV), Battery Electric Vehicles (BEV) and Fuel Cell Electric Vehicles (FCEV) [11, 12]. HEVs use both IC and electric engines. These vehicles self-charge by converting kinetic energy to electricity using regenerative braking. Like HEVs,

PHEVs also use both IC and electric engines. However, PHEVs unlike HEVs can charge off the grid. BEVs and FCEVs only use electric engines. BEVs can charge off the grid and has a longer electric driving range than HEVs and PHEVs. FCEVs operate using electricity generated by built-in fuel cells that combines hydrogen and oxygen from the air. These fuel cells can be recharged by refilling the vehicle with hydrogen. HEVs, PHEVs, BEVs, and FCEVs while running the electric motor have zero tailpipe emissions [12-14]. Although these EVs themselves do not emit GHGs, in most cases emissions still occur while generating the electricity required to power these vehicles [11, 12].

Since the Industrial Revolution during the 18th century, electricity was primarily generated by relying on cheap and abundant fossil fuels with the virtual abandonment of renewable resources. Natural resources like water has been used to generate hydroelectric power; however, the sun and wind have yet to be used widely. When considering the fact that the Earth receives more energy from the sun in an hour than the global population uses each year, it is evident that solar energy has a larger technical potential than all renewable and non-renewable resources for producing power. However, making this resource viable for efficient power production will require overcoming both technical and economic challenges [15].

Nevertheless, this was shown to be possible when in 1982, Hans Tholstrup and Larry Perkins, embarked on a journey across Australia from west to east in their home-built Solar Electric Vehicle (SEV), the *Quiet Achiever*. Inspired by this achievement and pioneering vision, Hans urged others to explore the possibilities of solar powered transportation. This led to the establishment of the World Solar Challenge (WSC), which first occurred in 1987 [16].

1.1 Background

1.1.1 The World Solar Challenge

The Bridgestone WSC is a biennial SEV race held in Australia, where participants have to travel 3,022 kilometres from Darwin to Adelaide. The participants include schools, universities, and technical institutions from all over the world [17-19].

Figure 1-3. The official route followed by participants of the WSC [20].

The purpose of this competition is to stimulate research into the development of sustainable carbon-free transportation, meaning that the WSC is primarily a design competition [17-19]. The design and construction of the SEV has to classify under one of the following classes:

- **Challenger Class** SEVs are designed for efficiency and carry only the driver. The winner of the Challenger Class will be the first Challenger Class SEV to complete the course, no other factors are taken into consideration [21].
- **Cruiser Class** SEVs are designed for practicality and must carry two or more occupants. The winner of the Cruiser Class will be judged on external energy use, the time taken to complete the course, payload carried, and practicality [22].
- **Adventure Class** SEVs are ones that had met the requirements of a previous recognised event, but does not comply with the requirements of the Challenger Class. Adventure Class vehicles must meet the safety requirements of this event [23].

1.1.1.1 Winning Criteria

To win the Cruiser Cup the team must traverse the prescribed route to arrive at Adelaide within the allocated time period, and have the highest score S, the value of which is determined using Equation 1.0 [24].

$$S = 80 \times \frac{E}{E*} + 20 \times \frac{P}{P*} \qquad \textit{Eq. 1.0}$$

In Equation 1.0, E is the team's energy efficiency score, E* is the highest energy efficiency score of any Cruiser team, P is the team's practicality score, and P* is the highest practicality score of any Cruiser team. The energy efficiency calculated using Equation 1.1 [24].

$$Energy\ efficiency = \frac{person - kilometre\ distance}{nominal\ external\ energy} \qquad \textit{Eq. 1.1}$$

Person-kilometre distance is the sum of the distances travelled by occupants within the SEV during the race. Person-kilometres will be counted for each seat that is occupied for a complete leg between consecutive control stops. Nominal external energy use of a Cruiser solar car will be calculated using Equation 1.2 [24].

$$Nominal\ external\ energy = (n + 1)\,Q \qquad \textit{Eq. 1.2}$$

Where n is the number of times the ESS is charged from external sources during the race, and Q is the nominal energy capacity of the ESS. The nominal energy capacity of a rechargeable electrochemical battery is the sum of the nominal cell masses in kilograms multiplied by [24]: $330\ Whkg^{-1}$ for Li-S cells; $250\ Whkg^{-1}$ for Li-ion cells; $250\ Whkg^{-1}$for Li-polymer cells; or, $125\ Whkg^{-1}$ for LiFePO4 cells.

The practicality score for a Cruiser team will be determined by a panel of judges appointed by the organiser. Factors that contributes to the practicality score include [24]:

- ease of access and egress,
- occupant space and comfort,
- ease of operation (driving and charging),
- versatility,
- style,
- and suitability for the declared purpose.

In accordance with WSC rules and regulations, for a team to place within the competition all of the aforementioned aspects have to be considered within the design.

1.1.2 Flinders Automotive Solar Team

Flinders University (FU), South Australia (SA), Australia will be competing within the WSC for the first time in 2017. FU will be participating in the Cruiser Class. In anticipation for the WSC, the Flinders Automotive Solar Team (thus forth referred to as the team or *FAST*) was founded by Dr. Stuart Wildy, a faculty member of FU's School of Computer Science, Engineering and Mathematics (CSEM). Dr. Wildy, currently acting as the Team Director with the support of a board of faculty members from the Engineering Department, supervises the project. In preparation for the WSC, Dr. Wildy assembled a team consisting of graduate and undergraduate students in 2016, to design and develop the Flinders University's Solar Electric Vehicle (FUSEV).

1.2 Problem Description

Following numerous discussions and the collective agreement that FU's has a lack of experience with the design and manufacture of automobiles, it was decided that FUSEV's design should closely resemble that of the teams that had won previously [25]. In addition to this, it was decided that due to the imposed time constraints, aside from the mechanical components, the FUSEV should be composed mainly of Commercial Off-The-Shelf (COTS) products.

1.3 Project Objectives

As part this Masters/Honours thesis, research was conducted for the design, development, and thermal simulation of an Energy Storage System (ESS) for the FUSEV. The purpose of the ESS is to store, monitor, and manage the energy drawn from the grid and solar panels, to power the electrical/electronic systems of the FUSEV. The ESS is composed of various sub-systems such as the Battery Management System (BMS), Cell Management Units (CMU) (the need for CMUs depends on the capabilities of the BMS), a Battery Charger (BC), and the Battery Array (BARR). To ensure FUSEV's eligibility for competing within the WSC, and for on road use in Australia, the ESS must adhere to all of the imposed design constraints.

The deliverables for this project will include the research into how to develop the ESS, market research into suitable and interoperable COTS products, and the development of the most ideal ESS design for the FUSEV. It is intended that this project will provide background information and FAST's design decisions regarding the ESS to allow continuity for students working on the FUSEV in the future. The work breakdown that details the main tasks/goals that need to be accomplished to ensure the successful completion of this research is as shown below.

- Identify Existing Solutions
- Research and Select Battery Chemistry
- Research and Select Battery Form Factor
- Research and Identify Battery Interconnectivity Method and Materials Required
- Design Modularized Battery Array
- Develop 3D Model of Battery Modules
- Develop 3D Model of Battery Array
- Develop Manufacturing Drawings of Battery Modules and Battery Array
- Develop Parts List for Battery Array
- Research and Select Battery Management System
- Research and Select Battery Charger
- Research and Select Battery Cooling Mechanism
- Develop Thermal Model of ESS
- Analyse Thermal Model of ESS
- Design ESS Enclosure using Results of Thermal Model Analysis
- Develop 3D Model of ESS Enclosure
- Develop Manufacturing Drawings of ESS Enclosure

Extension Goals (time and funding permitting):

- Develop ESS prototype
- Test ESS prototype

The design constraints that restricts the successful completion of the above-mentioned tasks/goals is as detailed within the following section of this chapter.

1.4 Design Constraints

To be eligible for competing within the WSC, the FUSEV must adhere to the imposed design constraints by the 2017 WSC rules and regulations.

1.4.1 WSC Rules and Regulations

The most important constraints that directly relates to the design of the ESS are as detailed in Table 1-1.

Table 1-1. A summary of WSC regulations that affects the design of the ESS [24].

Clause	Condition
2.5.2	The total cell mass is not restricted for Cruiser SEVs.
2.5.7	The ESS must be contained within at most two packs.
2.5.8	Electrochemical cells must not operate outside of the operating ranges for voltage, current and temperature specified by the manufacturer.
2.5.13	The ESS must be mounted in the SEV so that they will be restrained in a 196.2 $^{m}/_{s^2}$ acceleration.
2.5.14	If the ESS is capable of spilling dangerous liquids when damaged, there must be a spill-proof barrier between that ESS and the occupants.
2.5.15	If the ESS is capable of emitting dangerous gases when damaged, the SEV must be designed so that any gases will be vented to the exterior of the SEV behind any occupant ventilation intake, to ensure occupant safety.
2.28.10	The ESS must be protected by a fuse or circuit-breaker rated to interrupt the short-circuit fault current of the pack. This fuse or circuit-breaker must be mounted in or on the ESS.
3.18.2	Cruiser SEVs may recharge from external sources at any time except during control stop time. The recharge energy will contribute to the energy efficiency score.
3.18.5	Damaged energy storage cells may be bypassed, but must not be removed from the ESS unless it would be unsafe to leave them in. If the SEV is unable to continue because too many cells have been damaged, the team may, with the event organiser's permission, replace cells and continue the event within another class.

1.4.2 Australian Design Rules

For the SEV to be road legal within Australia it has to comply with the Australian Design Rules (ADRs). SA's Department of Planning, Transport and Infrastructure (DPTI) collated the ADRs and South Australian Road Traffic Light Vehicle Standards into the Individually Constructed Vehicles Standards (ICVS) document. Adhering to the standards within the ICVS allows for the vehicle to be road legal within SA. By reviewing the ICVS, it was ascertained that the standards it contained were more applicable to the mechanical systems of the SEV rather than the electrical/electronic systems. Consequently, the National Guidelines for the Installation of Electric Drives in Motor Vehicles was referred to for standards pertaining to the electrical/electronic systems. The most important constraints that directly relates to the design of the ESS are as detailed in Table 1-2.

Table 1-2. A summary of Australian regulations that affects the design of the ESS [26].

Clause	Condition
2.2	Class A: The batteries do not contain (spillable) liquid and do not discharge gases into the atmosphere during normal operation. Class B: The batteries contain (spillable) liquid and/or discharge gas during normal operation.
2.3	The battery system must adequately withstand at least the following crash accelerations: Front impact - 20 g (i.e. 20 times the battery weight); Side impact - 15 g; Rear impact - 10 g; and Vertical (rollover) impact - 10 g
2.4	All batteries that must be vented (i.e. Class B batteries) must be fully sealed from the passenger compartment, so that the transmission of gases or flames is prevented. The sealed compartment should be made from corrosion resistant materials, or if this not practical, lined with corrosive resistant materials. Fully sealed (i.e. Class A batteries) need not comply with this section. All batteries must be enclosed to provide water resistance and exclusion of foreign objects.

For series strings of batteries, some form of charge or balance management should be implemented. The necessity of this requirement will be dependent on the battery chemistry and technology used in the vehicle. This is especially critical with lithium chemistry batteries which must be maintained within strict upper and lower voltage limits and upper temperature limits.

2.14

Some form of device to monitor these limits on each individual cell or group of parallel cells should be present. If a monitoring device is fitted, the monitoring device must be capable, of either audibly or visually by means of a flashing lamp, warning the driver of an impending disconnect with sufficient time for the driver to safely park the vehicle before disconnection occurs.

Firstly, the remainder of this thesis details the literature review, market study, and competitor analysis conducted for selecting a suitable battery chemistry and form factor, selecting a suitable cooling system and determining the most suitable method for the thermal modelling of the proposed ESS design. Secondly, the thesis outlines the work that was done to develop the design for an ESS enclosure using Autodesk Inventor and the thermal analysis and optimization of the design using ANSYS Fluent. Lastly, the most suitable ESS design is selected, the outcomes of the project are discussed, the limitations of the project are presented and the future work to be conducted on the project is provided.

2 LITERATURE REVIEW

2.1 Battery Technologies

This section provides a summary of battery composition, battery chemistries, battery form factors and the safety concerns associated with the use of batteries.

2.1.1 Components of a Cell

A battery is an electrochemical device that generates electricity from the energy released through spontaneous chemical reactions. The most basic element of a battery is a cell. Batteries are formed by wiring these cells in series to increase the voltage or in parallel to increase the capacity. The three main components of a cell are anode, cathode and electrode [27, 28].

The anode is a conductive electrode from which electrons always flows out towards the cathode through an external circuit. The chemical reaction where the electrons are removed from the anode is referred to as oxidation.

The cathode is a conductive electrode to which the electrons flow towards. The chemical reaction where the electrons are accepted by the cathode is referred to as reduction.

The electrolyte separates the anode and cathode electrodes. These electrodes are immersed within the electrolyte. The cell when connected to an external circuit completes the circuit loop within the electrolyte, by relying on ions for electrical conduction.

2.1.2 Chemical Systems

This section provides a summary of battery chemistries that are typically used within automobiles, focusing on their suitability, advantages, and disadvantages.

2.1.2.1 Lead-Acid

Lead-acid batteries are commonly used within conventional cars, for ignition and to power the on-board electronics. These batteries are hugely popular and hold a dominant position within the market due to its capacity to provide reasonable performance at a low cost with a relatively long-lasting cycle-life. Consequently, these batteries were used to power EVs, during the early stages of EV development. However, these batteries though inexpensive and reliable were soon replaced with nickel and lithium based batteries due to their higher energy density and specific energy [29, 30].

2.1.2.2 Nickel Cadmium

Nickel Cadmium (NiCd) batteries are used for its larger charge-discharge rates and have a much higher energy and power density than lead-acid batteries, while being maintenance free over a wide temperature range and providing a long life cycle [29-32]. The biggest drawback to the NiCd batteries is its toxicity. Cadmium is a highly toxic metal, the use of which is being eliminated due to the adverse effects it has on the environment [31]. Another major disadvantage of using NiCd batteries, is its susceptibility to the memory effect which reduces its performance [29-32].

2.1.2.3 Nickel Metal Hydride

Nickel Metal Hydride (NiMH) batteries are a relatively new technology with characteristics similar to that of NiCd batteries. The principle difference is that the NiMH uses hydrogen, absorbed in a metal alloy, for the active negative material in place of the cadmium used within the NiCd. The NiMH is considered to be one of the two leading battery chemistries that are used within EVs, due to its ability to hold more energy than lead-acid batteries, whilst providing a longer life-cycle and being much lighter in weight. This battery has high self-discharge rate and is capable of delivering rapid power bursts. However, the battery's cycle-life will be reduced if it experiences repeated rapid discharges with a high load in order to give rapid power bursts. Therefore, this type of battery is more suitable in HEVs rather than BEVs which typically experiences deep discharge cycles [29-32].

2.1.2.4 Lithium-Ion

Lithium-Ion (Li-ion) is considered to be the other of the two leading battery chemistries, aside from NiMH that are typically used within EVs, due to its high cell voltage, and high energy density. There are numerous types of lithium battery chemistries available. The use of different material combinations within these batteries provides them with different properties and each combination is designed for a specific application [29, 30, 33, 34].

2.1.2.4.1 Lithium Cobalt Oxide

Lithium Cobalt Oxide (LCO) or $LiCoO_2$ offers good electrical performance, has high energy density, is easily prepared, has good safety properties, and is relatively insensitive to process variation and moisture. However, with its low discharge capacity and poor thermal stability on abuse, it is more suitable for implementation within laptops, mobile phones and other personal electronic devices that require high energy density with a low discharge rate. Consequently, it is not suitable for use in EVs or other industrial applications which require a high discharge rate [30, 33].

2.1.2.4.2 Lithium Manganese Oxide

Lithium Manganese Oxide (LMO) or $LiMn_2O_4$ offers a higher safety factor than LCO and comes at a lower cost. However, due to its limited cycle-life it is only suitable for smaller applications until there is a significant technological breakthrough [30, 33].

2.1.2.4.3 Lithium Iron Phosphate

Lithium Iron Phosphate (LFP) or $LiFePO_4$ is the most balanced of all the lithium chemistries due to its safety factor, high power density, long cycle-life and lower cost. However, its energy density is significantly lower than other lithium-based chemistries [30, 33].

2.1.2.4.4 Lithium Nickel Manganese Cobalt Oxide

Lithium Nickel Manganese Cobalt Oxide (NMC) or $LiNiMnCoO_2$ is a commonly used battery chemistry within the industry. NMC was developed to supply a similar or higher achievable specific capacity than LCO and similar operating voltage, at lower cost due to the reduced Cobalt content [35].

2.1.2.4.5 Lithium Nickel Cobalt Aluminium Oxide

Lithium Nickel Cobalt Aluminium Oxide (NCA/NCR) or $LiNiCoAlO_2$ has found widespread commercial use, particularly those manufactured by Panasonic for use in the ESS of the Tesla EVs. NCA has high usable discharge capacity and long storage calendar life compared to conventional Cobalt-based oxide chemistries. However, it was reported that with this chemistry, capacity fade may be severe at elevated temperatures (40-70° C) [35].

2.1.2.4.6 Lithium Titanate Oxide

Lithium Titanate (LTO) or $Li_4Ti_5O_{12}$ has been successfully commercialized because it provides superior thermal stability, relatively high volumetric capacity, and high cycle-life. However, these benefits are overshadowed by the higher cost of Titanium, reduced cell voltage, and lower capacity compared to other Li-ion based battery chemistries [35].

2.1.2.4.7 Lithium Sulphur

Lithium Sulphur or Li-S was developed to revolutionize the electric transportation industry. These batteries can store four times more energy than current Li-ion batteries per unit of weight. Consequently, they could extend the range of an electric vehicle to that of a traditional gasoline powered vehicle. Li-S is also significantly lower in cost than Li-ion batteries as sulphur is inexpensive, creating the potential for rapid and high market penetration. However, as the issues with overcoming the short cycle-life and volume changes still needs to be addressed, they have not yet been distributed on a commercial scale [36].

2.1.3 Chemistry Comparison

The specifications of the aforementioned battery chemistries were compiled into Table 2-1, to conduct a comparison to determine which chemistry would be best suited for use within the FUSEV. Ideally, both the maximum and nominal voltage of the battery must be as high so that fewer batteries can be interconnected to achieve the required voltage. The specific energy of the batteries must also be high to reduce the number of batteries used within the ESS to reduce the overall weight of the FUSEV. The cycle-life of the batteries must also be high to allow for repeated charge and discharge cycles without performance degradation [33].

Table 2-1. Comparative background data for battery chemistries.

Battery Chemistry	**Maximum Voltage (V)**	**Nominal Voltage (V)**	**Specific Energy (Wh/kg)**	**Cycle-life**
Lead Acid [37]	2.40	2.0	30-50	200-300
Nickel Cadmium/NiCd [37]	1.40	1.2	45-80	1000
Nickel Metal Hydride/NiMH [37]	1.40	1.2	60-120	300-500
Lithium Cobalt Oxide/LCO [38]	4.20	3.6	150-240	500-1000
Lithium Manganese Oxide/LMO [38]	4.20	3.7	100-150	300-700
Lithium Iron Phosphate/LFP [38]	3.65	3.2	90-120	1000-2000
Lithium Nickel Manganese Cobalt Oxide/NMC [38]	4.20	3.6	150-220	1000-2000
Lithium Nickel Cobalt Aluminium Oxide/NCA/NCR [38]	4.20	3.6	200-260	500
Lithium Titanate Oxide/LTO [38]	2.85	2.4	70-80	3000-7000
Lithium Sulphur/ [39]	2.50	2.1	550	40-50

From Table 2-1, it is evident that the NCA battery chemistry should be selected, as it is best suited for use within the FUSEV. This chemistry has the best overall specification. It has a high maximum and nominal voltage with the second highest specific energy, and a reasonable cycle-life meaning that fewer of these batteries would be required in the construction of the BARR, which reduces the system's complexity and FUSEV's overall weight.

2.1.4 Form Factors

Batteries are available in the cylindrical, prismatic or pouch form factors. The form factor selected is entirely dependent on its application within the design.

2.1.4.1 Cylindrical

Cylindrical cells pictured in Figure 2-1, are widely used within the electronics industry in many standardized formats from AA and AAA, to 18650 and 26650. Cylindrical cells have high specific energy, good mechanical stability, long cycle and calendar-life, and added safety features that are not possible with other formats at a much lower cost. The only disadvantage of using these cells is in its less than ideal packaging density due to the space cavities that would be present in between these cells. However, these cavities can be used as a pathway for coolant flow to improve the thermal performance of these cells [30, 33, 40].

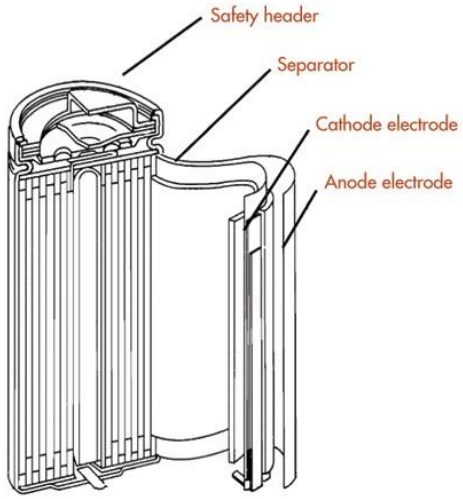

Figure 2-1. The cross section of a cylindrical 18650 cell, which is most commonly adopted by Li-ion cells [41].

The 18650 form factor has the highest energy density of all cylindrical form factors, even more so than both the prismatic and pouch form factors. The advantages offered by the 18650 form factor is evident in its use within the ESS of the Tesla EVs [30, 33, 40].

2.1.4.2 Prismatic

Prismatic cells pictured in Figure 2-2, are predominantly found within mobile phones, tablets and low-profile laptops. Large formats of these cells are also used within the ESS of EVs [30, 33, 40].

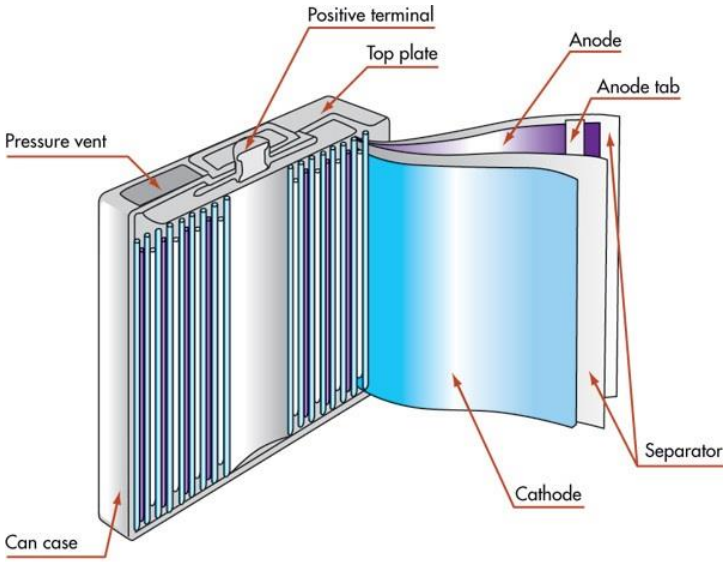

Figure 2-2. The cross section of a prismatic cell, which is cost effective and comes in a large variety of sizes [41].

These cells do not have standardized dimensions. Consequently, each manufacturer custom makes them for specific applications. The design flexibility that these cells offer over cylindrical cells allows for better space utilization. However, compared to cylindrical cells these cells are more expensive to manufacture, has a lower energy density, decreased mechanical stability, are less efficient and have a shorter cycle-life. As these cells provide a higher packaging density, ESS that use these cells tend to be less thermally efficient than ESS that use cylindrical cells. Any ESS designed using these cell formats needs include adequate cell spacing to account for volumetric expansion due to swelling [30, 33, 40].

2.1.4.3 Pouch

Pouch cells pictured in Figure 2-3, use a laminated architecture, which allows for the most efficient use of space, whereby achieving 90-95% packaging efficiency, the highest among battery packs [30, 33, 40].

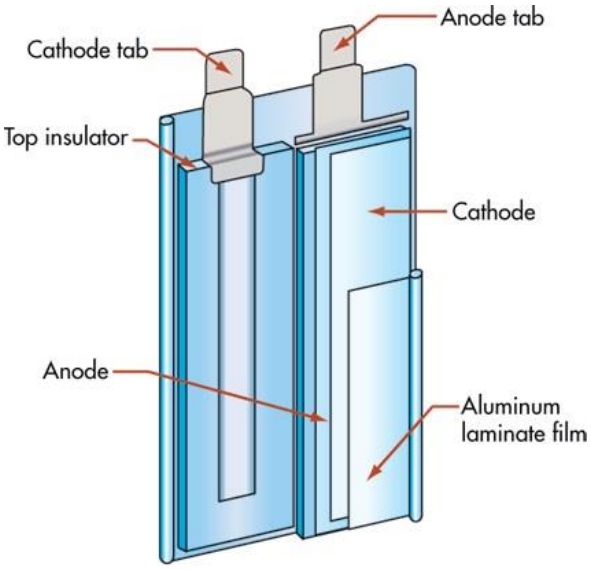

Figure 2-3. The cross section of a pouch cell, which is useful for space constrained applications [41].

These cells serve similar applications to prismatic cells, while being a lightweight and cost-effective alternative. However, the disadvantages of using these cells over prismatic or cylindrical cells is that any exposure these cells have to humidity or high temperature can significantly shorten its cycle and calendar-life. In addition to this, these cells have a tendency for a swelling of up to 8-10% after 500 cycles which needs to be accounted for in any ESS designs. It is predicted that there will be a shift toward this cell format in the future due to its potential for greater capacity than the cylindrical format. However, this form factor still needs a significant breakthrough in design before it can be used within the ESS of EVs [30, 33, 40].

2.1.5 Comparison of Form Factors

The battery form factors were compared against one another with their advantages and disadvantages presented in Table 2-2.

Table 2-2. Comparison of form factors adopted by battery manufacturers.

	Cylindrical	**Prismatic**	**Pouch**
Advantages	• Light Weight • Lowest cost per watt hour • Provides greater area for thermal conduction • Good mechanical stability • High specific energy • Long cycle-life • Long calendar life • Standardized battery dimensions • Cheaper to manufacture than prismatic cells	• Higher packaging density than cylindrical •	• Highest packaging density of all form factors • Light weight
Disadvantages	• Battery interconnectivity more complex for high voltage/capacity systems • Low packaging density • System occupies more volume	• Non-standardized battery dimensions • Designs need to account for additional spacing to allow for expansion • Low energy density • Low mechanical stability • Short cycle-life • More expensive to manufacture than cylindrical	• Package swelling is expected • Exposure to high temperatures or humidity shortens cycle-life

From Table 2-2, it is evident that the advantages offered by the cylindrical form factor outweighs those offered by both prismatic and pouch form factors. In particular, cells of the 18650 cylindrical form factor would be best suited for FUSEV's BARR as it has the highest energy density of all form factors. Selecting this form factor in conjunction with the NCA chemistry would significantly reduce the weight of the BARR thereby FUSEV's ESS.

2.2 Performance and Safety Concerns

Consumer safety has been a serious concern with the use of ESS within EVs. This section provides a summary of performance and safety concerns such as thermal runaway, over-charging, high temperature and low temperature that are associated with the use of the batteries within the ESS.

2.2.1 Thermal Runaway

Thermal runaway is a condition which occurs when the activation temperature of various exothermic chemical reactions inside cells, on charge or discharge is reached. The cell degrades with a large release of energy, leading to venting of cell contents and temperature increase. This increase in temperature changes the operational conditions in such a way that causes a further increase in temperature, which often leads to a destructive event like a fire or an explosion [30, 42].

2.2.2 Over-charging

Overcharging occurs when a cell is charged to a State-of-Charge (SOC) greater than 100%. In other words, overcharging a battery means that more ampere-hours of charge were put into the battery than was removed from the battery on the previous discharge. Batteries can be overcharged even by low rates of charge current. Overcharging causes irreversible internal cell degradation, which may lead to thermal runaway, cell swelling, venting and reduce battery performance and cycle-life. The robustness of various cell designs to overcharging varies with respect to its chemical composition, which must be taken into account for the design of the ESS [30, 42]. Overcharging can be handled through the use of a BMS.

2.2.3 High Temperatures

Internal cell heating can occur from excessive charge or discharge and exposure to high ambient temperatures or abnormal heat sources. The internal cell heating will increase the rate of cell degradation which in turn can lead to thermal runaway. The range of acceptable cell temperatures varies, but most cells begin to experience higher rates of degradation above 45-55 °C and at temperatures between 60-100 °C the likelihood of a destructive event like a fire or an explosion occurring increases significantly [30, 42]. The occurrence of high cell temperatures is of concern as the ambient temperature in Darwin typically range from 21.6-31.8 °C [43] and ambient temperature in Adelaide typically range from 11.8-22 °C during October (month the competition is held) [44].

2.2.4 Low Temperatures

Most cells have limited charging capabilities at lower temperatures. Charging at lower temperatures can lead to irreversible capacity loss due to plating of the anode and possibility of metallic growth within the cells, which may penetrate the separator causing an internal short circuit. The discharge capability is also limited at lower temperatures due to increased cell impedance. Many cell manufacturers recommend inhibiting charging below 0 °C and some permit low-rate charging down to -10 °C [30, 42]. The temperature ranges the batteries are exposed to during the competition while higher than that minimum recommended by the manufacturer is still below the optimal ambient temperature. This means that the batteries are still subjected to adverse effects caused by charging and discharging.

2.3 Thermal Management Systems

Given the various means for heat generation the ESS may be subjected to, a Thermal Management System (TMS) needs to be implemented to maintain the BARR temperature within the manufacturer's recommended temperature range. The fundamental goal of the TMS is to ensure that the BARR can deliver the required power whilst operating at an optimum average temperature and ensuring that there is minimal variation in temperature across the BARR [45, 46].

2.3.1 Thermal Management Techniques

This section provides a summary of the thermal management techniques such as passive convection air cooling, forced convection air cooling and indirect liquid cooling that are adopted within EVs.

2.3.1.1 Passive Convection Air Cooling

Passive convection air cooling is the dissipation of heat through the air at ambient temperature by means of conduction. This method is often used within consumer electronics like TVs, MP3 players, etc. by providing the means for ventilation on the product's enclosure to enable air at ambient temperature to enter, and heated air to freely leave the enclosure [47]. One such TMS designed by Chong, et al. for the ESS they had developed is pictured within Figure 2-4 and was used to verify that the thermal performance of a large scale TMS could be represented by a smaller subset composed of 24 batteries, while yielding reasonably reliable results [48].

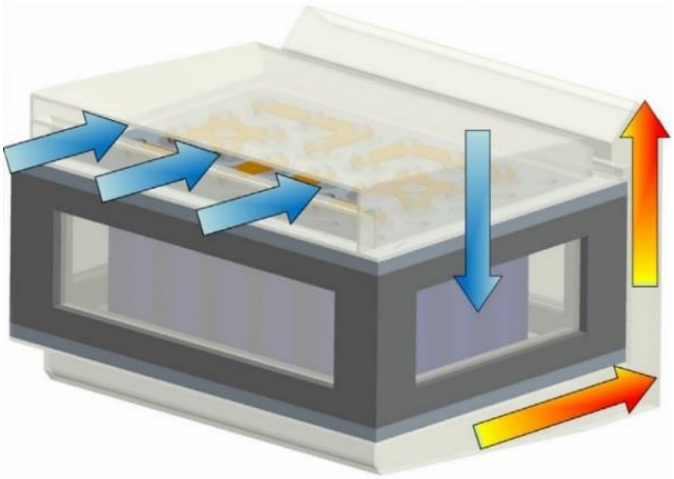

Figure 2-4. CAD model of a battery pack that uses passive convection air cooling, blue arrows indicate ambient input airflow and red arrows indicate output airflow [48].

2.3.1.2 Forced Convection Air Cooling

When passive convention air cooling is not adequate, forced convection air cooling is implemented using fans, pumps or a jet of air. Typically, in electronic systems, fans are a popular means of circulating air over hot surfaces. Consequently, fan selection is an important aspect to consider in forced convection. The primary considerations to make in the selection of a fan includes (1) the static pressure head of the system which is the total resistance an electronic system offers to air as it passed through, and (2) the volumetric rate of air-flow required for cooling [47].

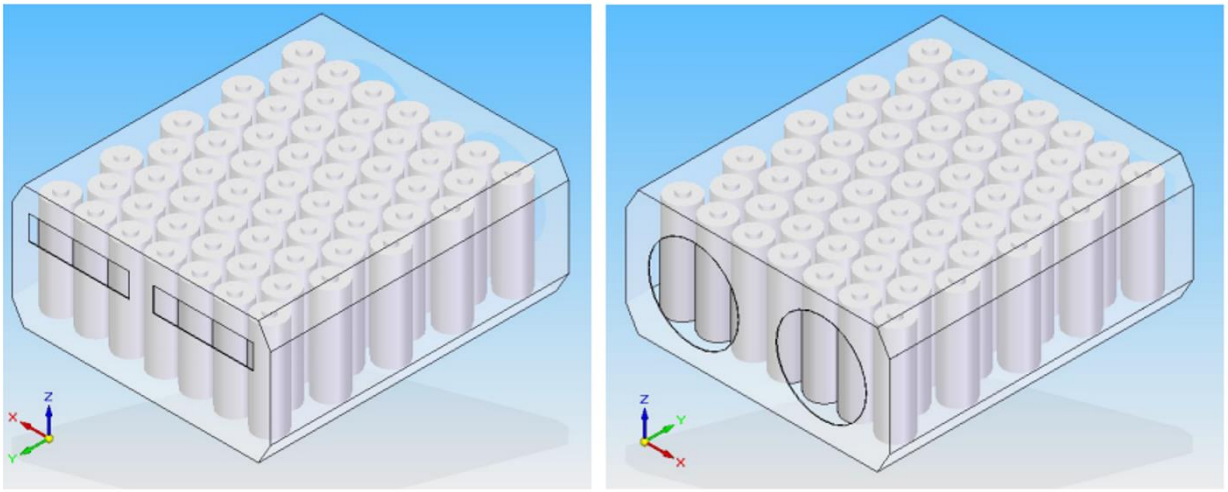

(a) (b)

Figure 2-5. CAD model of a battery pack that uses forced convection air cooling. (a) Inlet vent and (b) Outlet vent [49].

ESS that employ forced convention air cooling includes design provisions that takes the form of plenum spaces below and above the BARR, with cooling passages between the cells connecting the two plenums as shown in Figure 2-5. The construction provides a means for the external connection of a high-volume, low-pressure air source. Supplying air at 23 °C, will not only effectively cool an overheating BARR, it will also rapidly warm a cold BARR. The heat transfer coefficient from the battery core is improved up to 10 times by this technique [30].

2.3.1.3 Indirect Liquid Cooling

Indirect liquid cooling is used when it is crucial that there be no contact between the electronic component and the coolant. The coolant is directed along the walls of the jacket or enclosure of the ESS, to provide a medium for thermal conduction. Water or water/glycol solutions are preferred coolants for indirect liquid cooling because they have lower viscosity and higher thermal conductivity than most oils, resulting in higher heat transfer coefficients. Indirect liquid cooling is implemented within high performance computers and EVs. Although liquid cooling/heating is more effective than air cooling, it has its drawbacks such as significantly increased mass, potential for leaks, increased design complexity and increased maintenance cost [47]. A TMS that uses in-direct liquid cooling is pictured in Figure 2-6, in this TMS, the coolant is directed through the tubes along the cooling plate housed between the battery modules [50].

Figure 2-6. CAD model of a battery pack that uses indirect liquid cooling, blue arrows indicate coolant input and red arrows indicate coolant output [50].

2.3.2 Comparison of Thermal Management Techniques

The thermal management techniques were compared against one another with their advantages and disadvantages presented in Table 2-3.

Table 2-3. Comparison of TMS adopted by vehicle manufacturers [30].

	Passive Convection Air Cooling	**Forced Convection Air Cooling**	**Indirect Liquid Cooling**
Advantages	• Light Weight • Simple	• More effective than passive convection air cooling • Can be designed for low power consumption	• More effective heat transfer than either passive or forced convection air cooling • Average fluid temperature more consistent
Disadvantages	• Complicated distribution of air within pack • Incoming air must be free of dirt and water from road • Variable ambient temperature	• More power consumption than passive convection air cooling	• Increased weight • Elaborate module design • Higher average fluid temperature • High power consumption

From Table 2-3, it is evident that for the FUSEV's ESS either passive or forced convection air cooling is more suitable than indirect liquid cooling, as it would be lower cost, require less power, and be significantly lighter. In particular, it was decided that Axial Case Fans (ACFs) be used to implement the forced convection air cooling as it is effective and the TMS most BMSs employ include provisions for their use. The advantage of convection air cooling is that if specifically designed for it, the TMS can use both passive and forced methods for cooling. In addition to these advantages, the use of ventilations for convection air cooling means that the WSC regulations and ADR requirements for the need of ventilation to expel any hazardous gases the BARR may emit is also addressed.

2.4 Thermal Modelling

From the previous sections, it is evident that battery performance is significantly affected by the operating temperature of the BARR, and the temperature distribution across the BARR. Consequently, prior to manufacturing, a numerical or analytical thermal model of the ESS need to be developed to analyse the proposed design. The equations for thermal behaviour in these models are based on [51]:

- The energy balance equation,
- The heat generation equation - complex or simplified and,
- The boundary condition equations - linear/nonlinear, conduction, convection and or radiation.

Numerical and analytical models use Partial Differential Equations (PDE) to solve the energy balance equation. One of the core components of the internal heat generation within the ESS, is attributed to the temperature-current dependent over-potential, and SOC dependent change in entropy heat generation. Over-potential heat generation is always positive and is caused by the internal resistance within the battery, with the kinetic aspects and mass transport resultant of electrochemical reactions. Heat generation due to entropy change on the other hand can be positive or negative and is attributed to the reversible electrochemical reactions within the battery [51]. This section provides a summary of the thermal modelling techniques typically used by researchers, their advantages and disadvantages.

2.4.1 Lumped Capacitance Model

Lumped Capacitance Model (LCM) is a transient conduction approach that assumes that the temperature of the solid is spatially uniform at any instant during the transient process. This assumption entails that temperature gradients within the solid are negligible. In neglecting temperature gradients within the solid, the problem can no longer be considered from within the framework of the heat equation, since it is a PDE that governs the spatial temperature distribution within the solid. Instead, the transient temperature response is determined by formulating an overall energy balance on the entire solid. This balance relates the rate of heat loss at the surface to the rate of change of the internal energy and is represented by Equation 3.0 [51-53].

$$\boldsymbol{pVC_p\frac{dT}{dt} = -hA(T - T_a)} \qquad \textit{Eq. 3.0}$$

The application of LCM is valid for certain criterion such as steady-state conduction through the plane wall of area A extended to transient processes. One surface is maintained at a temperature $T_{s,1}$ and the other surface is exposed to a fluid of temperature $T_a < T_{s,1}$. The temperature of this surface will be some intermediate value $T_{s,2}$, for which $T_a < T_{s,2} < T_{s,1}$. Under steady state conditions the surface energy balance reduces to that represented by Equation 3.1 [51-53] .

$$\boldsymbol{\frac{kA}{L_c}\left(T_{s,1} - T_{s,2}\right) = hA\left(T_{s,2} - T_a\right)} \qquad \textit{Eq. 3.1}$$

By rearranging Equation 3.1, Equation 3.2 can be obtained.

$$\boldsymbol{\frac{T_{s,1} - T_{s,2}}{T_{s,2} - T_a} = \frac{\left(\frac{L_c}{kA}\right)}{\left(\frac{1}{hA}\right)} = \frac{hL_c}{k} \equiv Bi} \qquad \textit{Eq. 3.2}$$

The quantity Bi that appears in Equation 3.2 is the dimensionless parameter termed as the Biot (Bi) number. The Bi number plays a fundamental role in conduction problems that involve surface convection effects as it provides a measure of the temperature drop in the solid relative to the temperature difference between the solid's surface and the fluid. Research has shown that LCM is acceptable for situations with Bi < 0.1, as shown in Equation 3.3. A Bi significantly less than 1, conforms with the assumption

that spatial temperature is uniform within the solid. If Bi is >1, it means that there would be temperature gradients within the body, whereby invalidating the underlying assumption required for the application of this method [51-53].

$$Bi = \frac{hL_c}{k} < 0.1 \qquad \textit{Eq. 3.3}$$

The LCM approach has previously been adopted for the thermal modelling of Lead-Acid batteries using National Renewable Energy Laboratory's (NREL) Advanced Vehicle Simulator (ADVISOR) MATLAB plug-in models. These models integrated with battery performance information allows the user to predict the temperature changes in a EVs battery according to the drive cycle, air cooling flow rate and battery type. In these models the heat transfer equations were based on the fact that heat generation in the core of the battery occurs because of the electrochemical reactions and resistive heating collectively influencing the battery's temperature. The heat is conducted through the case material and then transferred through convection from the case's external surface to the surroundings. The battery core and case were modelled as two separate isothermal nodes. All the associated components inside the case such as the cathode, anode, separators, active materials etc. were assumed to be of a single homogenous material with averaged properties. Other assumptions made within this model were [51-53]:

i. The core and modules were assumed to be isothermal due to the high conductivity of the core.
ii. The temperature of the case was very close to that of the battery due to the low thermal mass of the case.

Hallaj, et al. conducted a study that utilised LCM to simulate temperature profiles within Li-ion cells under different operating conditions and cooling rates for scaled-up Li-ion cells using the Finite Element Method (FEM). FEM was used to solve the energy balance equation and accumulate a collection of simulated results. To ensure applicability of LCM the authors ensured that Bi was sufficiently low i.e. <0.1 and the simulated results were validated through a comparison of them to its experimentally measured equivalent [51-53].

2.4.2 Finite Element Method

The FEM or Finite Element Analysis (FEA), is a numerical method in which approximate solutions of large and complicated problems is determined through its discretization into smaller and simpler elements. In particular, a body of matter such as solid, liquid, or gas, is represented as an assemblage of subdivisions called finite elements. These elements are considered to be interconnected at specified joints called nodes. The nodes usually lie on the element boundaries where adjacent elements are considered to be connected. Since the actual variation of the field variable (e.g., displacement, stress, temperature, pressure, or velocity) inside the continuum is not known, we assume that the variation of the field variable inside a finite element can be approximated by a simple function. These approximating functions are defined in terms of the values of the field variables at the nodes. When field equations for the whole continuum are written, the new unknowns will be the nodal values of the field variable. By solving field equations, which are generally in the form of matrix equations, the nodal values of the field variable will be known. Once these are known, the approximating functions define the field variable throughout the assemblage of elements. In general, the spatial temperature distribution within the ESS can be represented by Equation 3.4 [51, 54].

$$\frac{d^2T}{dx^2} + \frac{d^2T}{dy^2} + \frac{\dot{q}_t}{k} = \frac{1}{a}\frac{dT}{dt} \qquad \textit{Eq. 3.4}$$

Unlike the LCM approach, the FEM approach requires in-depth knowledge on each of the materials used in the ESS to achieve accurate results. If this information was not provided by the manufacturers it was determined experimentally for its integration with the FEM model [51, 54]. The FEM approach has previously been used to determine the effectiveness of various TMS and for the optimization of ESS. In these applications, the boundary conditions were defined at the boundary of the thermal management media and the external boundary of the ESS [51, 54].

2.4.3 Finite Volume Model

Finite Volume Method (FVM) is a numerical technique that transforms PDEs representing conservation laws over differential volumes into discrete algebraic equations over finite volumes, elements or cells. Similar to FEM, the first step in the solution process is the discretization of the geometric domain into non-overlapping finite volumes. The PDEs are then transformed into algebraic equations by integrating them over each discrete element. The system of algebraic equations is then solved to compute the values of the dependent variable for each of the elements [55].

In FVM, some of the terms in the conservation equation are turned into face fluxes and evaluated at the finite volume faces. Because the flux entering a given volume is identical to that leaving the adjacent volume, the FVM is strictly conservative. This inherent conservation property of the FVM makes it the preferred method in Computational Fluid Dynamics (CFD). Finally, in the FVM it is quite easy to implement a variety of boundary conditions in a non-invasive manner, since the unknown variables are evaluated at the centroids of the volume elements, not at their boundary faces. These characteristics have made FVM quite suitable for the numerical simulation of a variety of applications involving fluid flow, heat and mass transfer. The developments in the method have been closely entwined with advances in CFD. From a limited potential at inception confined to solving simple physics and geometry over structured grids, the FVM is now capable of dealing with all kinds of complex physics and applications using CFD [55].

He, et al. developed a 2D CFD model using ANSYS FLUENT 14, for their investigation of the thermal management of multiple cells Li-ion modules. The results obtained were experimentally validated. However, authors have acknowledged that the underlying assumptions made for the application of FVM within their study was deemed to be valid for only a fixed range of ideal ambient temperatures and work is currently underway to generalise the approach for applications where the temperature varies in a wide range [51, 55].

2.4.4 Equivalent Circuit Model

Equivalent Circuit Models (ECM) composed of one voltage source, one series resistor, and RC blocks (a capacitor and resistor in parallel with one another) are capable of replicating the nonlinear electrochemical processes of cells whilst avoiding complex calculations. These models operate by establishing a correlation between the electrochemical processes within the cell and the circuit elements themselves. The thermal properties of the cell are represented by equivalent electrical quantities; temperature by voltage, heat flux by current, conductive resistance by conductive conductance, convective resistance by convective conductance and heat storage by capacitance [51, 56].

Depending on the characteristics of the problem to be analysed, the number of RC blocks typically ranges from one to two, since larger numbers increase computational effort without significantly improving model accuracy. In a study conducted by Ceraolo, et al. regarding the thermal dependence for the characterization and simulation of high power lithium batteries, the single RC block shown in Figure 2-7 was deemed adequate for modelling the system. The ECM was also previously been used within many problems of industrial relevance [51, 56].

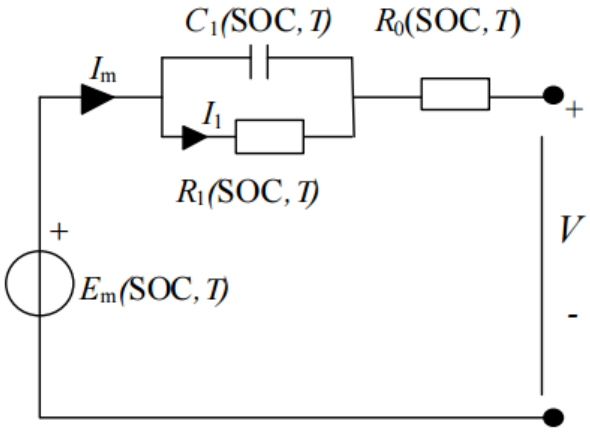

Figure 2-7. A typical single RC block ECM of an electrochemical cell [56].

The value of the independent ECM components E_m, R_0, R_1 and C_1 depends on SOC and inner cell temperature. The inner cell temperature is assumed to be uniform, and taken as the average temperature inside the cell. This cell temperature can be computed by solving the heat equation of a homogeneous body exchanging heat with the environment using Equation 3.5 [51, 56].

$$C_P \frac{dT}{dt} = -\frac{T - T_a}{R_T} + P_S \qquad \textit{Eq. 3.5}$$

Applying a Laplace transformation using a transform variable (s) on Equation 3.5 yields Equation 3.6 [51, 56].

$$T(s) = \frac{P_S R_T + T_a}{1 + R_T C_P s} \qquad \textit{Eq. 3.6}$$

This method was the ideal approach for the task of continuously monitoring the temperature distribution of an ESS in a study conducted by Xiao. In this study an ECM was used concurrently with a small number of physical sensors to estimate the temperature distribution throughout the remaining larger area of an ESS in real-time. The ECM used in the study estimated the thermal distribution of the battery with negligible error in less than 15 seconds [51, 56].

2.4.5 Comparison of Thermal Modelling Techniques

The thermal modelling techniques were compared against one another with their advantages and disadvantages presented in Table 2-4.

Table 2-4. Comparison of thermal modelling techniques used by vehicle manufacturers to analyse ESS [51-56].

Technique	Advantages	Disadvantages
LCM	• Simple and requires minimal component data to develop a satisfactory model. • Typically adopted in conjunction with other techniques to simplify complex problems.	• Physical constraint limits application to systems that satisfies Bi<1. • Hallaj et al. noted inaccuracy of their model at unusually high or low temperatures. • Less accurate than FVM/FEM as approximations are used.
FVM/FEM	• Higher level of accuracy compared to LCM and ECM. • Useful for optimization of the system designed. • CFD used within the industry for thermal modelling of ESS. • Provides a visual representation of system operation. • Mathematical functions used within the model are handled by CFD analysis software.	• Computational intensive. • Requires extensive information regarding chemical and material compositions for an accurate ESS representation. • Inflexible in that model created cannot easily be repurposed for other battery chemistries.
ECM	• Significantly faster, more flexible and easier to formulate solution than LCM and FVM/FEM. • Requires minimal component data regarding materials and thermo-physical properties of the cell.	• Similar to LCM, ECM is less accurate than FVM/FEM as approximations are used.

From the table it is evident that FEM in conjunction with CDF is best suited for the analysis of FUSEV's ESS as a visual representation of the heat distribution can be obtained from which regions of interest can be identified, the thermal model can be made more accurate, and the ESS design can be optimized for improved thermal response of the batteries.

3 Design Rational and Development

3.1 Competitor Analysis

The information regarding the ESS developed by teams that successfully completed WSC 2015 was collated and presented in Table 3-1, to perform the competitor analysis.

Table 3-1. Components used within the ESS developed by successful participants of WSC, 2015 and their specifications.

	Team		
	Eindhoven University of Technology [57]	University of New South Wales [58]	Bochum University of Applied Sciences [59]
Vehicle	Stella Lux	Sunswift	ThyssenKrupp SunRiser
Battery Make and Model	Panasonic NCR18650GA	Panasonic NCR18650BF	Panasonic NCR18650B
Number of Batteries Used	1224	1224	1227
Battery Array Capacity (kWh)	15.2	14.7	14.8
Battery Array Weight (kg)	58.75	56.92	59.51
Battery Management System Make and Model	Custom	Tritium IQ BMS and CMU	Custom
Battery Charger Make and Model	BRUSA Elektronik NLG513 Air	Thunderstruck TSM2500 Series	Eltek Valere EV Power Charger 220/3000 HE

From Table 3-1, its evident that the underlying design decisions made while teams developed their ESS was relatively consistent. All teams developed BARRs composed of NCA 18650 batteries, which support the findings of the literature review. All teams used batteries manufactured by Panasonic and the models used by each team only had minor variations in its electrical and mechanical specification. The primary design differences between the ESS designs were with the selection of the BMS and BC. Sunswift was the only SEV to use a COTS BMS within their ESS, while Stella Lux and SunRiser used custom made BMSs. All teams used COTS BCs within their ESS, the electrical specification of which are similar for use in Australia, with only their mechanical specification differing.

3.2 Market Study

As the ESS is to be constructed of COTS products, a market study was conducted that utilized both the literature review and competitor analysis to determine what components must be purchased.

3.2.1 Battery Selection

Selection of the battery is crucial, as it determines the electrical, mechanical, and chemical specifications of FUSEV's BARR. From the literature review and competitor analysis, it is evident that the search for suitable batteries should be limited to those of the 18650 form factor and NCA chemistry. The specification of the most popular COTS NCA 18650 batteries are presented within Table 3-2. The gravimetric energy density of these batteries was used to compare the batteries as it defines the capacity of the battery in terms of energy per kilogram.

Table 3-2. Specifications of COTS NCA 18650 batteries currently available within the market.

Make	Model	Maximum Voltage (V)	Nominal Voltage (V)	Nominal Capacity (Ah)	Weight (g)	Gravimetric Energy Density (Wh/kg) *
LG Chem	INR18650MH1 [60]	4.20	3.67	3.20	49.0	239.67
	INR18650HG2 [61]	4.20	3.60	3.00	47.0	229.79
	ICR18650E1 [62]	4.35	3.75	3.10	49.0	237.24
Panasonic	NCR18650B [63]	4.20	3.60	3.35	48.5	248.66
	NCR18650BF [64]	4.20	3.60	3.35	46.5	259.35
	NCR18650GA [65]	4.20	3.60	3.45	48.0	258.75
	NCR18650BD [66]	4.20	3.60	3.00	49.0	220.41
	NCR18650A [67]	4.20	3.60	3.00	47.5	227.37
	NCR18650BE [68]	4.20	3.60	3.00	48.5	222.68
Samsung	ICR18650-30B [69]	4.35	3.78	2.95	48.0	232.31
	ICR18650-30A [70]	4.30	3.70	3.00	48.0	231.25

* As the gravimetric energy density of not all cells were provided in their datasheet, it was calculated using the available information.

From Table 3-2, it is evident that the Panasonic NCR18650BF with the highest gravimetric energy density, is best suited for use within FUSEV's ESS as it is lightweight, has a high voltage, high capacity, and has previously been successfully adopted by SEVs within the WSC. Table 3-3, provides the mechanical and operational specifications of the NCR18650BF.

Table 3-3. Mechanical and Operational Specifications of the Panasonic NCR18650BF [64].

Max Height (mm)	Max Diameter (mm)	Charge Temperature Range (°C)	Discharge Temperature Range (°C)	Storage Temperature Range (°C)
65.30	18.50	0 ~ +45	-20 ~ +60	-20 ~ +50

3.2.2 Battery Management System Selection

The BMS ensures the safe operation of the batteries. It monitors the SOC, current and voltage of the cells, and protects the cells against over-voltage, under-voltage, over-current and over-temperature. Although most teams had built their own BMS, FASTs decision to use COTS products means that a market study had to be conducted. The search for a suitable BMS was limited to only those that in addition to the aforementioned features included active or passive cell balancing, and a programmable baud rate for compatibility with FUSEV's proposed Controller Area Network Bus (CANBUS) system. The information obtained through the study is presented within Table 3-4, to perform a product comparison.

Table 3-4. Specifications of COTS BMS currently available within the market.

	Make				
	Tritium [71]	Ewert Energy Systems [72]	Elithion [73]	Manzanita Micro [74]	Ventec iBMS [75]
Model	IQ BMS and CMU	Orion Standard Size BMS	Lithiumate Pro	MK3x12 Digital Lithium Regulator	8-18S
Cells Manageable	≥ 8	≥ 12	1-255	7-254	≥ 8
Cell Balancing	Yes	Yes	Yes	Yes	Yes
Communication Protocol and Number of Interfaces	CANBUS (x1)	CANBUS (x2)	CANBUS (x1)	REGBUS (x1)	CANBUS (x1)
Field Programmable	No	Yes	Yes	Yes	No
Thermal Management	ACF and Temperature Sensor	ACF and Temperature Sensor	N/A	ACF and Temperature Sensor	Temperature Sensor
Weight (kg)	0.190	2.430	0.940	0.054	N/A
Supply Voltage (V)	12	8-16	12	5	N/A

The product comparison was conducted during a FAST meeting, the proceedings of which are as follows:

- The MK3x12 would require both a communication interface between its REGBUS and FUSEV's CANBUS, and an additional DC to DC step down voltage converter to power the BMS, adding unnecessary system complexity through the inclusion of more components to enable integration.
- The Lithiumate Pro does not include provisions for a TMS to be implemented within the ESS, so one has to be custom built to fulfil this need.
- The 8-18S is not field programmable nor does it include provisions for controlling ACFs. This means that FUSEV's CANBUS must be designed around the 8-18S to enable its successful integration. Like the Lithiumate Pro, the 8-18S would require a custom built TMS to be implemented within the ESS.
- The Tritium BMS, while not field programmable had the advantage of compatibility with the other major components operating on FUSEVs CANBUS, as they too were manufactured by Tritium. The Tritium BMS was also previously used within WSC.
- The Orion BMS allows for design flexibility as it is field programmable, has two CANBUS interfaces that can be programmed with different baud rates and has a PC software that allows for the real-time monitoring of the ESS and data logging. This BMS is also designed for direct compatibility with a number of BCs. The only disadvantage of using the Orion BMS is in its weight due to the inclusion of a heatsink.

The Tritium BMS was considered the best choice; however, upon contacting the manufacturer to obtain quotes for its purchase, it was discovered that the company had ceased production. Consequently, the Orion BMS the secondary option was selected for integration into the FUSEV ESS.

3.2.3 Battery Charger Selection

The Battery Charger (BC) charges the ESS batteries using AC mains. To limit the search for a suitable COTS BC, only those that were compatible with the Orion BMS and the mains in Australia (rated at 230V and 50Hz) were selected. The information obtained through the market study is presented within Table 3-5, to perform a product comparison.

Table 3-5. Specifications of COTS BC currently available within the market.

	Make				
	ThunderStruck Motors [72, 76]	Manzanita Micro Charger [72, 77]	Zivan [72, 78]	Eltek Valere [72, 79]	Elcon/TC Charger [72, 80]
Model	TSM2500 and Charge Controller	PFC20-X	NG5	220/3000 HE EV Power Charger - IP67 G2	PFC 2500 Battery Charger TCCH-168-12
Output Power (kW)	3.0 ≥	4.8 ≥	4.8 ≥	3.0 ≥	2.0 ≥
Communication Protocol and Number of Interfaces	CANBUS (x1)	REGBUS (x1)	N/A	CANBUS (x1)	CANBUS (x1)
Field Programmable	Yes	Yes	N/A	Yes	Yes
Baud Rate (KBps)	250 and 500	N/A	N/A	125, 250 and 500	250
Thermal Management	ACF and Heat Sink	ACF	ACF	Water Cooled Cold-Plate (Optional)	ACF and Heat Sink
Weight (kg)	7.07	7.26	9.00	4.30	7.07

The product comparison was conducted during a FAST meeting, the proceedings of which are as follows:

- Both TSM2500 and 220/3000 HE have been previously used within the WSC. These products have similar operational specifications but different in the manner in which they are cooled; consequently, the 220/3000 HE is lighter than the TSM2500.
- The PFC 2500, was deemed not flexible enough to allow for any deviations in the future design of the ESS as it only has an output power of up to 2kW and its baud rate is fixed at 250KBps, which may require the establishment of a secondary CANBUS, as FUSEV's CANBUS currently operates at 500KBps.
- The NG5 is the least preferable option as it weighs the most and it does not include a CANBUS interface. It requires additional components to obtain the same information that is made available as a standard by the other BCs.
- The PFC20-X would require an intercommunication interface between its REGBUS and FUSEV's CANBUS, adding unnecessary system complexity through the inclusion of more components to enable integration.

It was collectively decided that the FUSEV should implement either the 220/3000 HE or the TSM2500 BC within its ESS. Though the 220/3000 HE is preferred, its selection is dependent on whether or not it can be mounted onto the chassis at a location where it receive adequate passive convection air cooling. However, as the design of the chassis has not yet been finalized, a decision cannot be made. Despite this setback, as a COTS product known as the Cellpro PowerLab 8 is to be purchased to charge and discharge the battery modules, it was decided that the BC will be purchased early 2017.

3.3 Prototyping Platform

As the FUSEV will not be manufactured prior to 2017, a Yamaha YDRE G22E golf cart was purchased to integrate it with prototypes of the FUSEV subsystems, to convert the golf cart into a SEV. Subsequently, a prototype of the FUSEV ESS needs to be made to replace the Trojan T-875 batteries the golf cart uses. The golf cart uses 6 Trojan T-875 batteries connected in series to drive its JU2-H1890-00 electric motor. The specification of the T-875 is presented in Table 3-6.

Table 3-6. Electrical, Mechanical, and Operational Specifications of the Trojan T-875 [81].

Chemistry	**Nominal Voltage (V)**	**Nominal Capacity (kWh)**	**Length (mm)**	**Width (mm)**	**Height (mm)**	**Weight (kg)**	**Operational Temperature Range (°C)**
Flooded/Wet Lead-Acid	8	1.51	259	180	283	29	-20 ~ +45

As the COTS products selected have the capacity to work under a range of operating conditions, they will be able to work with both the golf cart or FUSEV. Therefore, the same components will be used within the prototyping platform, with only the bus voltage and capacity of the golf cart's ESS being the primary difference from FUSEV's ESS. Consequently, for the remainder of this thesis FUSEV will refer to the golf cart.

3.3.1 Battery Configuration

The JU2-H1890-00 electric motor that drives the FUSEV is rated at 48V. Consequently, to meet the power requirement of the motor, the BARR must have a nominal bus voltage of 48V. The nominal bus voltage can be achieved using the Panasonic NCR18650BF by connecting the batteries in series by spot welding the positive terminal of each battery to the negative terminal of the next battery [82]. The calculation used to determine the nominal BARR voltage is as shown in Equation 4.0.

$$\textbf{Number of Series Cells} = \frac{\textbf{Nominal BARR Voltage}}{\textbf{Nominal Cell Voltage}} = \frac{48V}{3.6V} = 13.\dot{3} \qquad \textit{Eq. 4.0}$$

From this calculation it was determined that to achieve the nominal bus voltage 14 batteries should be connected in series. FAST had also collectively decided to limit the nominal capacity of the BARR to 30Ah to allow for quicker charge and discharge cycles. The nominal capacity can be achieved using the Panasonic NCR18650BF batteries by connecting the batteries in parallel by spot welding all the positive terminals together and spot welding all the negative terminals together [82]. The calculation used to determine the nominal ESS capacity is as shown in Equation 4.1.

$$\textbf{Number of Parallel Cells} = \frac{\textbf{Nominal BARR Capacity}}{\textbf{Nominal Cell Capacity}} = \frac{30Ah}{3.35Ah} = 8.955\ldots \qquad \textit{Eq. 4.1}$$

From this calculation it was determined that to achieve the nominal BARR capacity 9 batteries should be connected in parallel. Therefore, the FUSEV's BARR must have a 14s9p configuration to achieve the nominal bus voltage and nominal capacity. To modularize the design, it was decided that the batteries be interconnected into 1s9p modules to get modules with a voltage of 3.6V and capacity of 30Ah nominal. This means that 14 of such modules would need to be connected in series would cumulatively form the FUSEV's BARR.

3.3.2 Battery Assembly and Interconnection

Through a consultation with other competitors and FAST it was decided that the modules be built using the NCR18650BF cells, battery spacers, nickel plated copper tabbing material, copper busbars, fiberglass sheets, Anderson cables, brass nuts and bolts. The battery spacers are interlocking brackets that can be configured to contain any number of cells. Two sets of these brackets in a 3x3 configuration will be used to contain the cells as a rigid structure that allows for air-flow. The tabbing material will be spot welded using a capacitive discharge spot welder to interconnect the cells in parallel. Both the anode and cathode plates formed by the tabbing material will include a hole to allow bolts to be inserted through it, for connecting the modules in series using Anderson cables with ring terminals. The nuts are to be used to secure any wiring with ring terminals to the bolts on the modules. The copper busbars are used to interconnect various sets of modules and fiberglass sheets used to electrically insulate the terminals to avoid the occurrence of short-circuits. Figure 3-1 shows the 3D model of the battery module, Figure 3-2 shows the 3D model of the BARR, and Figure 3-3 shows the exploded view of the BARR; these models were designed within Autodesk Inventor. The mechanical drawings of the battery module, tabbing material dimensions, and BARR are included in Appendix E, F and G respectively.

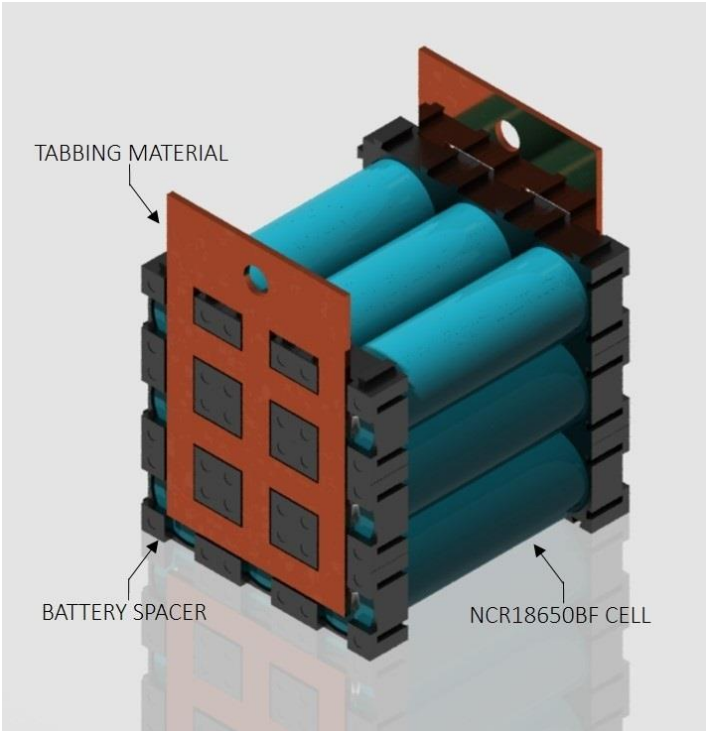

Figure 3-1. FUSEV's fully assembled 1s9p battery module at 3.6V and 30Ah Nominal.

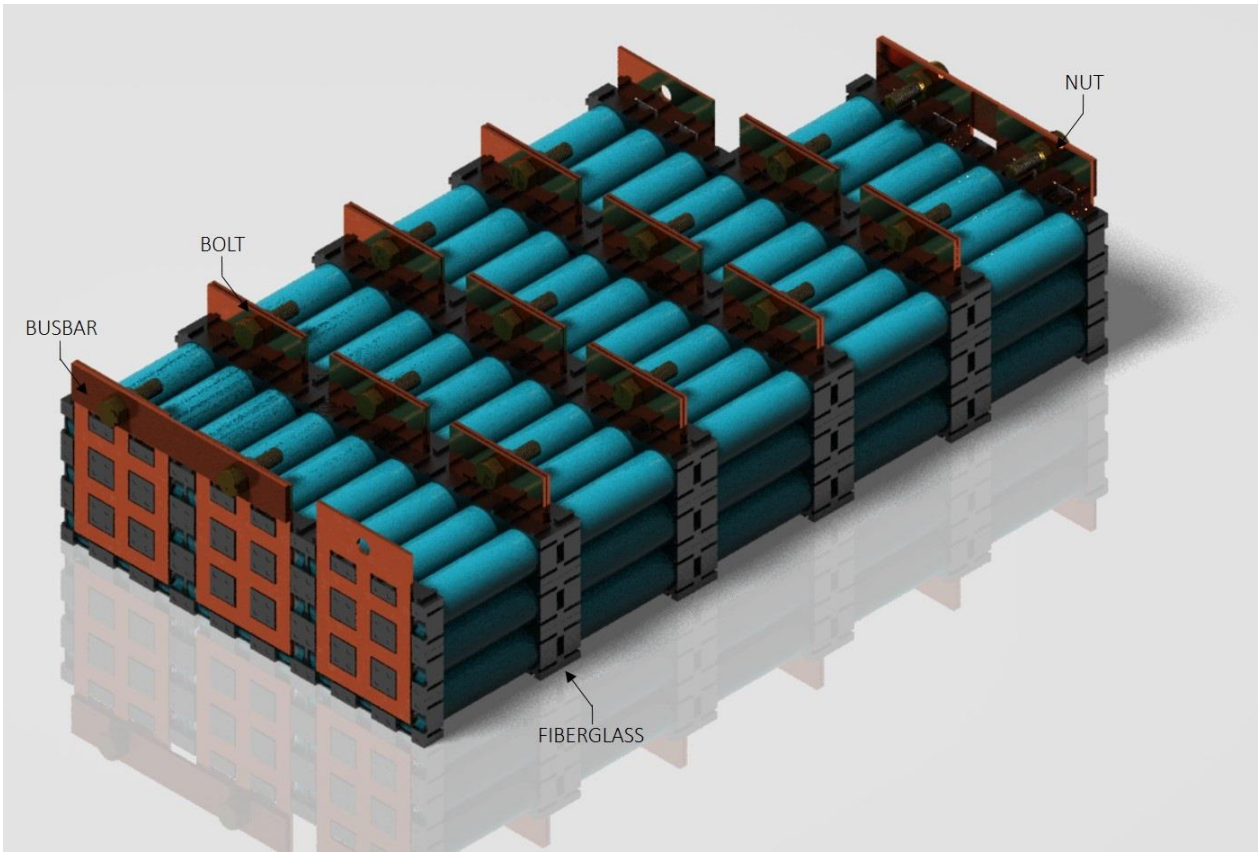

Figure 3-2. FUSEV's fully assembled 14s9p BARR at 50.8V and 30Ah Nominal.

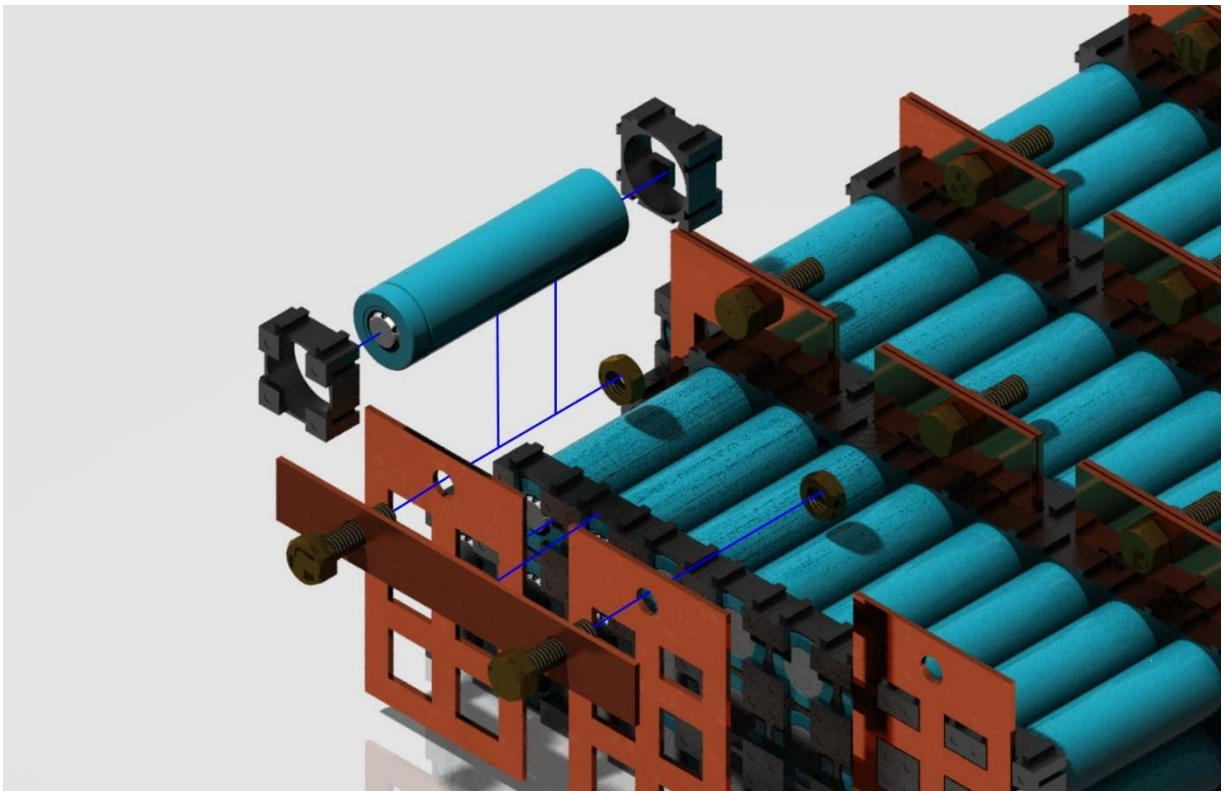
Figure 3-3. Exploded view of FUSEV's BARR at 50.8V and 30Ah Nominal.

The main advantage of this design for the BARR and modules is that the fundamental concepts used for its construction can be applied for the development of a BARR with any bus voltage and or capacity. The capacity of the module can be increased by connecting more cells in parallel and the bus voltage of the BARR can be increased by connecting more modules in series. This provides greater flexibility in the design of the ESS in that the modules can be repurposed for other uses, and the BARR configuration can be modified to meet the requirements of other COTS products employed within the FUSEV. Furthermore, such design allows for modules to be easily replaced or bypassed to comply with Clause 3.18.5 of the WSC regulations to ensure that team can continue to compete within the WSC despite the occurrence of any faults. The only disadvantage of using this design is that if any of the modules were to be malfunction due to a single cell, then the entire module needs to be dismantled to resolve the issue. The parts-list for the FUSEV's BARR is included within Appendix A and the mechanical drawings of the 1s9p battery module, 14s9p BARR and tabbing material is included within Appendix E, F and G respectively.

3.4 Computational Fluid Dynamics

As per Clause 2.4 of the regulations detailed within Table 1-2, the BARR has to be contained within an enclosure. This in addition to the imposed size constraint by the battery bracket within the FUSEV and the need for BARR cooling, means that the enclosure has to be custom-built. The design of the enclosure was determined by conducting a thermal FEA on the BARR using the ANSYS CFD software package. FEM was selected as per the reasoning mentioned within Table 2-4. Forced convection air cooling using ACFs and the TMS enabled by the Orion BMS was determined to be the method best suited for BARR cooling as per the reasoning mentioned within Table 2-3, ensuring that Clause 2.14 of the regulations detailed within Table 1-2 and Clause 2.5.8 and 2.5.14 of the regulations detailed within Table 1-1 are met. The following sections detail the baseline study conducted to ensure accuracy of results generated, the methodology used, the development of the CFD models, the settings used to obtain the results and the analysis of the results generated.

3.4.1 Baseline Study

A baseline study was conducted to ensure that the results generated closely match real-world performance, by replicating the thermal behaviour of an experimentally validated CFD model developed by Cicconi et al [49]. This model was used in conjunction with a study conducted by Hallaj, et al. [51, 83] in which the response of 18650 cell temperature under different cooling rates was simulated using FEM. Their study was experimentally validated and operated under the following assumptions [51, 83]; the body of the 18650 cell is thermally homogenous with effective thermo-physical properties; the properties of the 18650 cell are independent of temperature over the range of operating temperatures; heat is uniformly generated throughout the 18650 cell; the core and modules are isothermal due to the high conductivity of the core; and the temperature of the case is very close to the core/battery due to the low thermal mass of the case. In addition to this, the model they developed only considered the effects of radial heat transfer of the 18650 cell as it was experimentally proven to be substantially larger than the axial heat transfer of the 18650 cell.

The information made available from these researchers were amalgamated to produce the baseline CFD model shown within Figure 3-4 (b), which closely resembles the

CFD model developed by Cicconi shown within Figure 3-4 (a). A difference of only 0.65% and 0.35% was observed for the maximum and minimum temperatures between Cicconi's and the baseline model. Visually, the airflow within the baseline model has more turbulence along the sides of the enclosure; however, the airflow along the top of the cells, at the inlets and outlets are nearly identical.

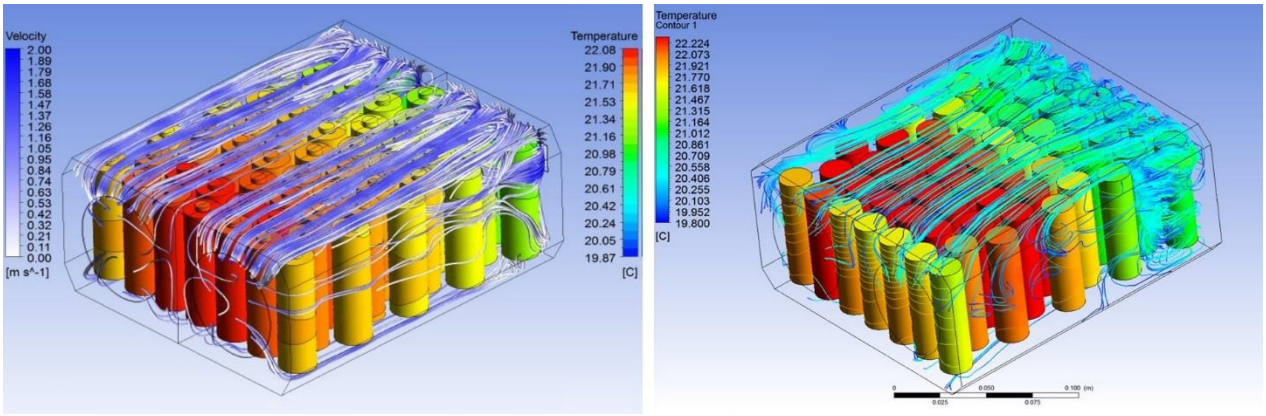

(a) (b)

Figure 3-4. Isometric-view of the airflow and heat distribution in (°C) of the CFD models used within the Baseline study.
(a) Cicconi's CFD model [49] and (b) baseline CFD model.

The volumetric heat distribution within Cicconi's model is shown in Figure 3-5 (a) and the baseline model is shown in Figure 3-5 (b) are also reasonably identical.

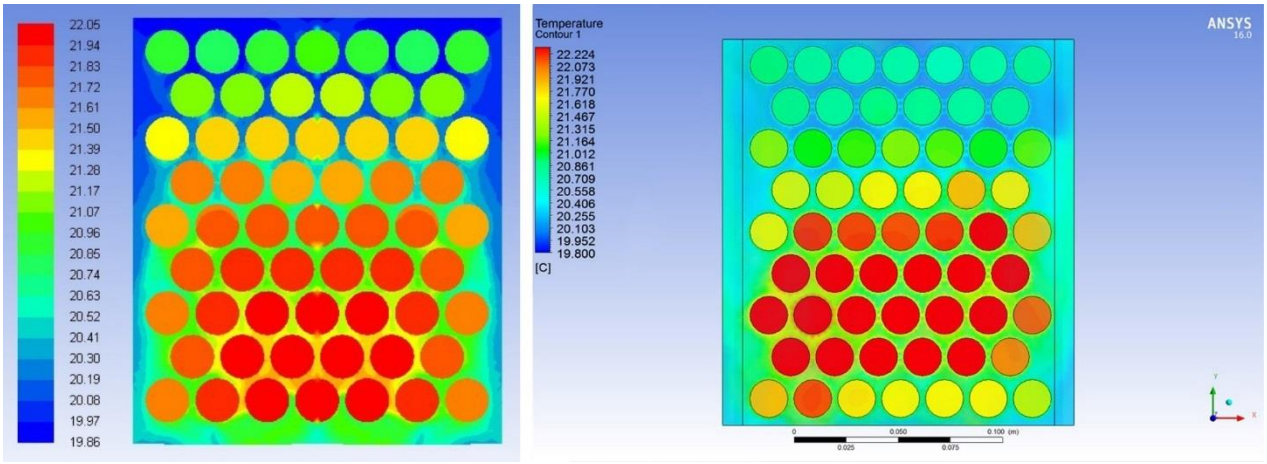

(a) (b)

Figure 3-5. Top-view of the volumetric heat distribution (°C) of the CFD models used within the Baseline study.
(a) Cicconi's CFD model [49] and (b) baseline CFD model.

As the maximum and minimum temperature of the baseline model is within a tolerance of ± 0.5 °C from its equivalent in Cicconi's model, the ANSYS configuration used to generate the baseline model was deemed to be reliable and representative of real-world

performance. The miniscule discrepancies between Cicconi's and the baseline model's air-flow and volumetric heat distribution can be attributed to the fact that several approximations had to be made as neither the exact settings used within FLUENT nor the exact dimensions of Cicconi's enclosure were provided.

As the baseline study validated the configuration used within FLUENT, this configuration was used for the development of all the CFD models during this project. The details regarding the configuration used is included in later sections of this chapter.

3.4.2 Methodology

Numerous methodologies adopted by other analysts were reviewed and the methodology shown in Figure 3-6, that incorporates both the Inventor and ANSYS environments was tailor-made for the purposes of this project. This methodology was used for the development of the thermal CFD models used within the baseline study and the thermal analysis of the ESS enclosure.

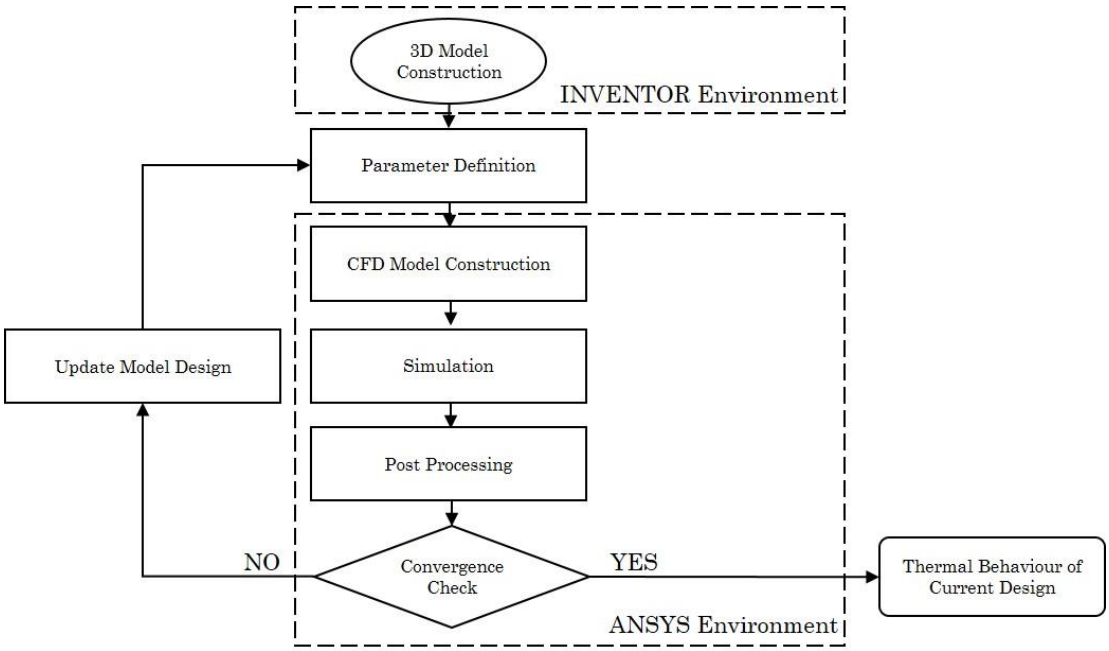

Figure 3-6. The tailor-made methodology for the thermal analysis of the FUSEV's ESS.

3.4.3 CFD Model Development

FUSEV's enclosure was designed with dimensions that allows for it to contain the BARR whilst using the restraining mechanism enabled by the FUSEV's battery bracket. In accordance with the imposed constraints, numerous variations of the enclosure design were developed; each with different inlet and outlet dimensions. The form and the dimensions of the inlets and outlets were limited to that of the standardized ACFs and Ventilation Filters (VF). This in conjunction with the allowable enclosure height restricts the inlets and outlets to a circular form with a diameter of 30mm, 40mm, 50mm or 60mm. The combination for the potential inlet and outlet dimensions gives 16 design variations of the ESS enclosure. One such design iteration is as shown in Figure 3-7.

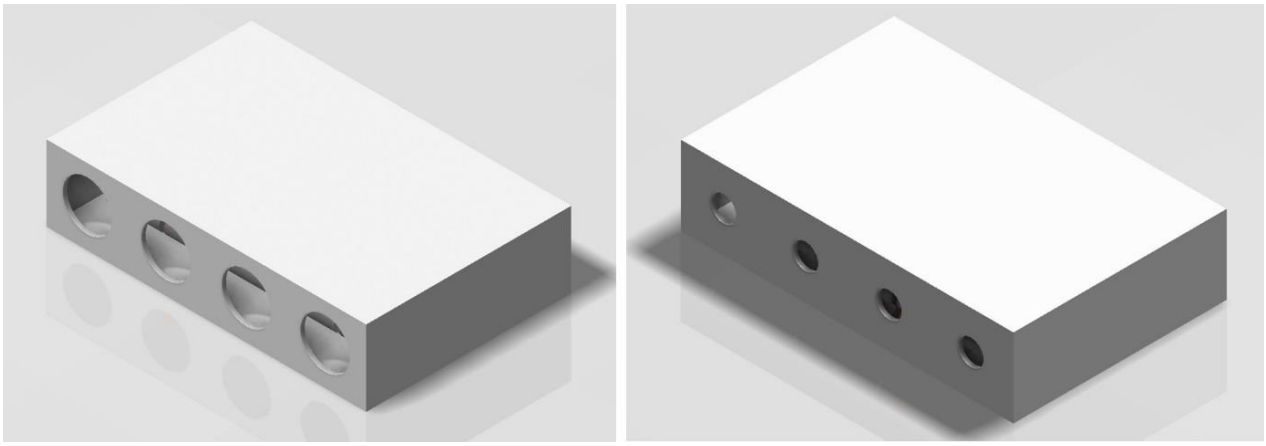

(a) (b)

Figure 3-7. CAD model of the enclosure design with openings for ACFs and VFs.
(a) 60mm Inlet vent and (b) 30mm Outlet vent.

Preliminary simulations revealed that the detailed BARR model shown within Figure 3-2, was computationally intensive and that the inclusion of battery spacers (composed of Acrylonitrile Butadiene Styrene or ABS), ACFs (composed of Polybutylene Terephthalate or PBT) and fiberglass were unnecessary due to their lack of thermal conductivity as shown in Table 3-8. Consequently, the detailed BARR model was replaced with the simplified BARR model shown in Figure 3-8, ensuring that the BARR was placed into each enclosure design variation at a fixed position for consistency.

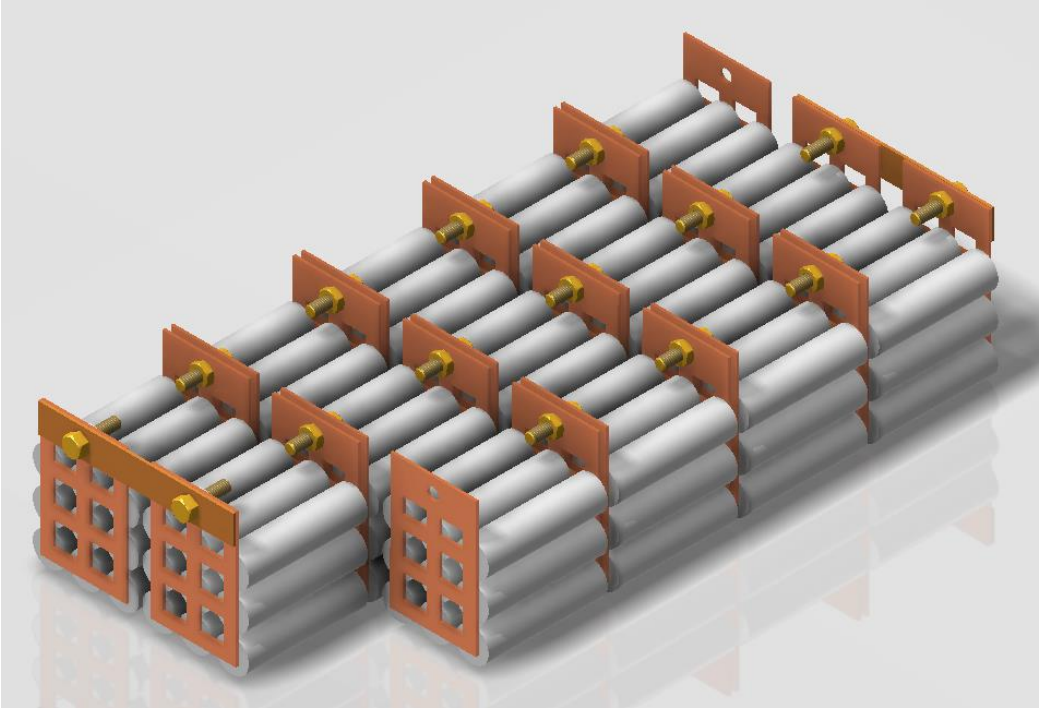

Figure 3-8. Simplified Model of FUSEV's fully assembled 14s9p BARR.

The 3D models of the simplified BARR and enclosure were developed in Autodesk Inventor and exported as IGES files. These files were imported into ANSYS ICEM DesignModeler and identical features of these models were grouped and labelled. To observe thermal behaviour within the enclosure, the DesignModeler was used to seal all openings with caps, and the internal flow geometry for the fluid region was defined using these caps. Figure 3-9, shows the caps and internal flow geometry defined for the enclosure in Figure 3-7.

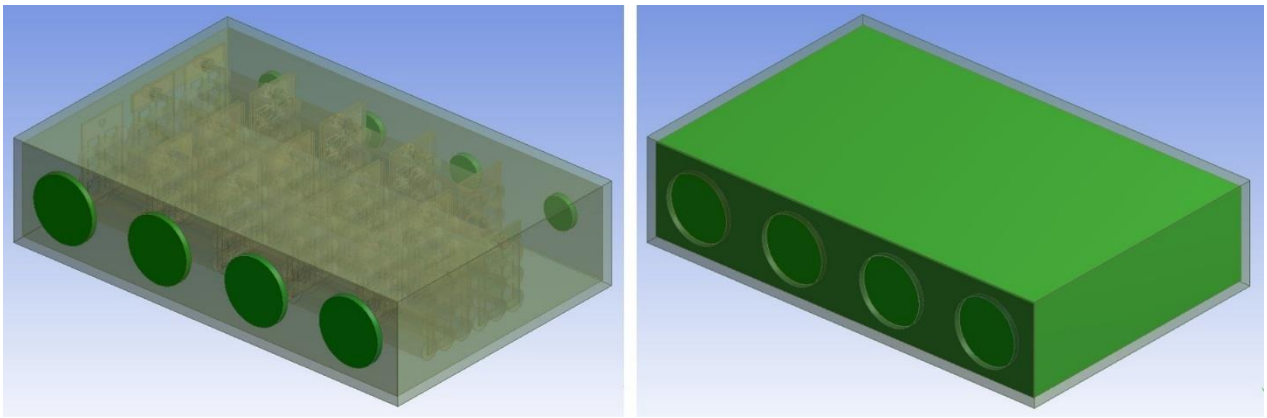

(a) (b)

Figure 3-9. Enclosure model with Inlet of 60mm and Outlet of 30mm.
(a) The caps used for sealing openings and (b) defined internal flow geometry.

3.4.4 Mesh Generation

The models within ANSYS ICEM DesignModeler were transferred into ANSYS ICEM Meshing. An unstructured mesh consisting of 5,875,931 tetrahedral elements was generated for the 204 bodies encompassed within 7.4784e+006 mm^3 of the ESS volume. A minimum mesh size of 0.25 mm and maximum mesh size of 45 mm were selected for the analysis, ensuring that regions of interest were represented with a fine mesh. Refining only select regions of the mesh helped yield accurate results while reducing computational effort. The settings used for mesh generation were kept consistent for each variation of the ESS enclosure design. Figure 3-10 shows the side-view, Figure 3-11 shows the top-view and Figure 3-12 shows the front-view of the ESS mesh generated.

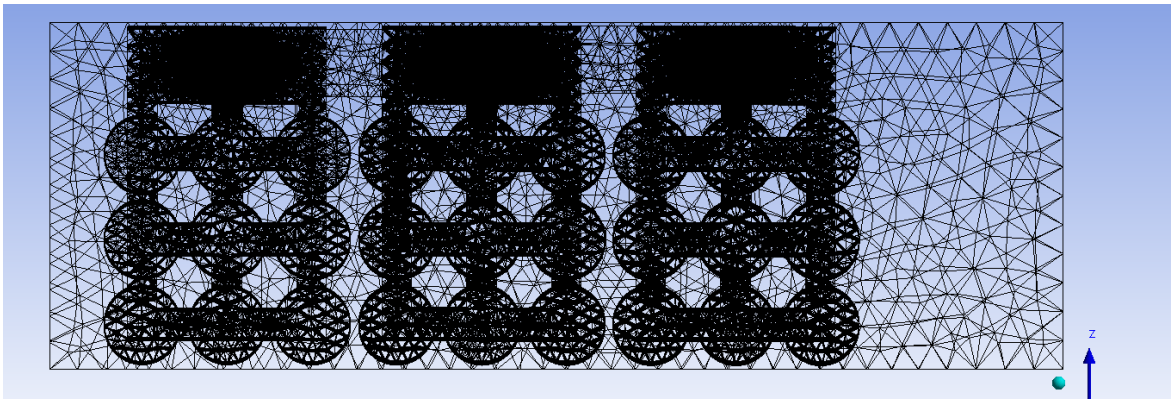

(a)

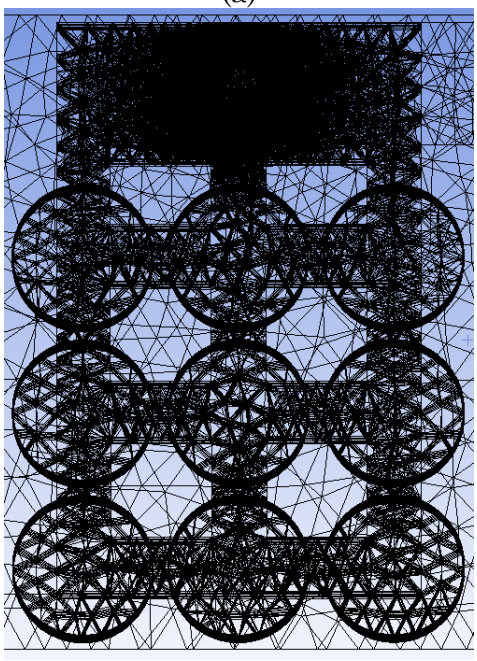

(b)

Figure 3-10. The side-view of the ESS mesh generated using ANSYS ICEM Meshing. (a) The BARR and (b) close-up of a single battery module.

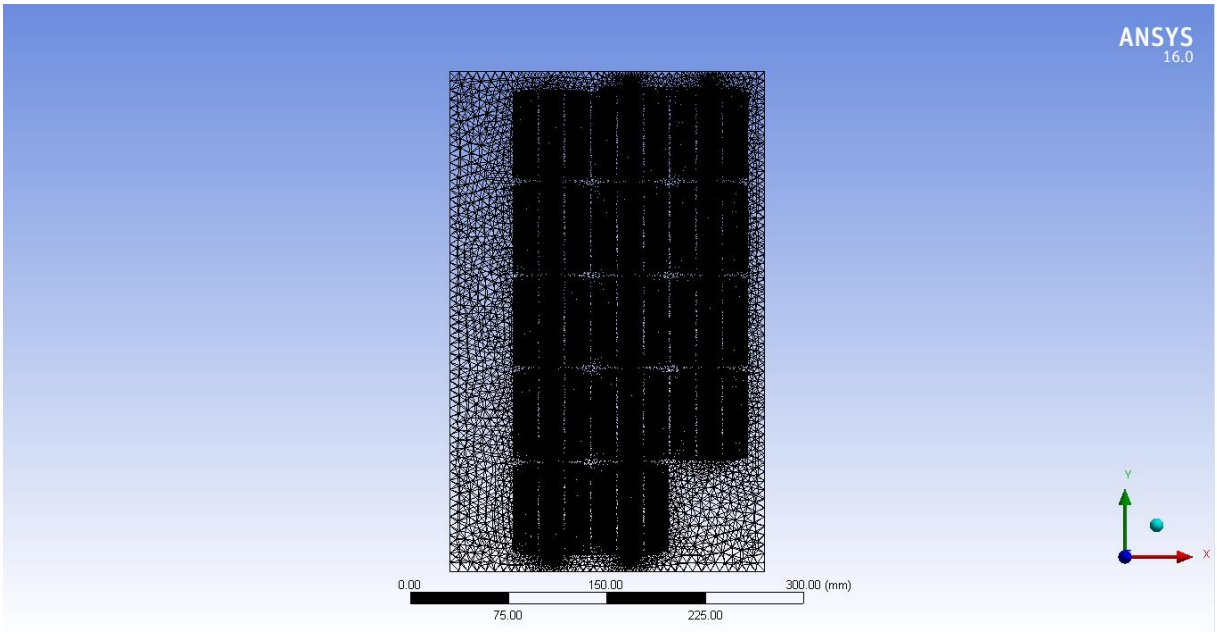

(a)

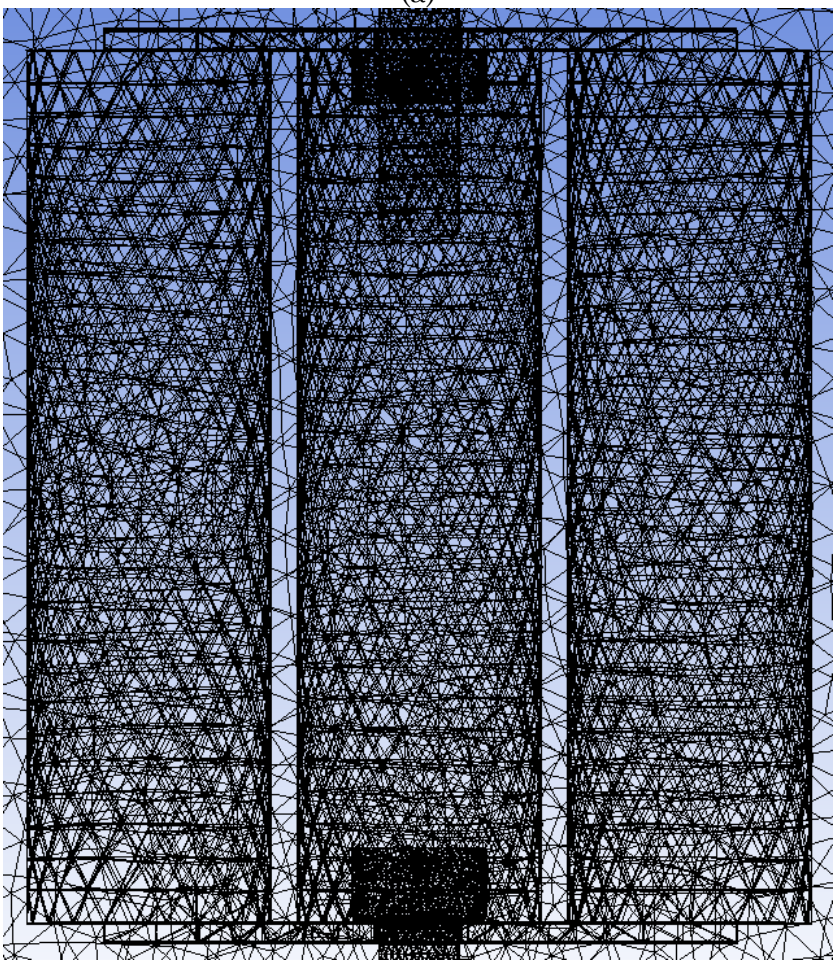

(b)

Figure 3-11. The top-view of the ESS mesh generated using ANSYS ICEM Meshing. (a) The BARR and (b) close-up of a single battery module.

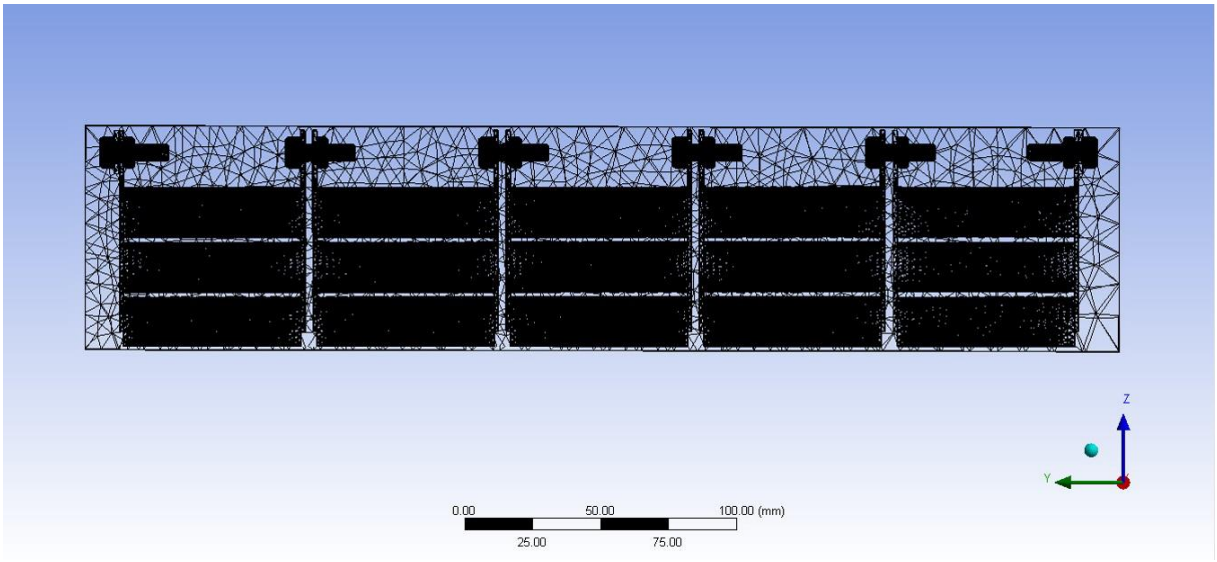

(a)

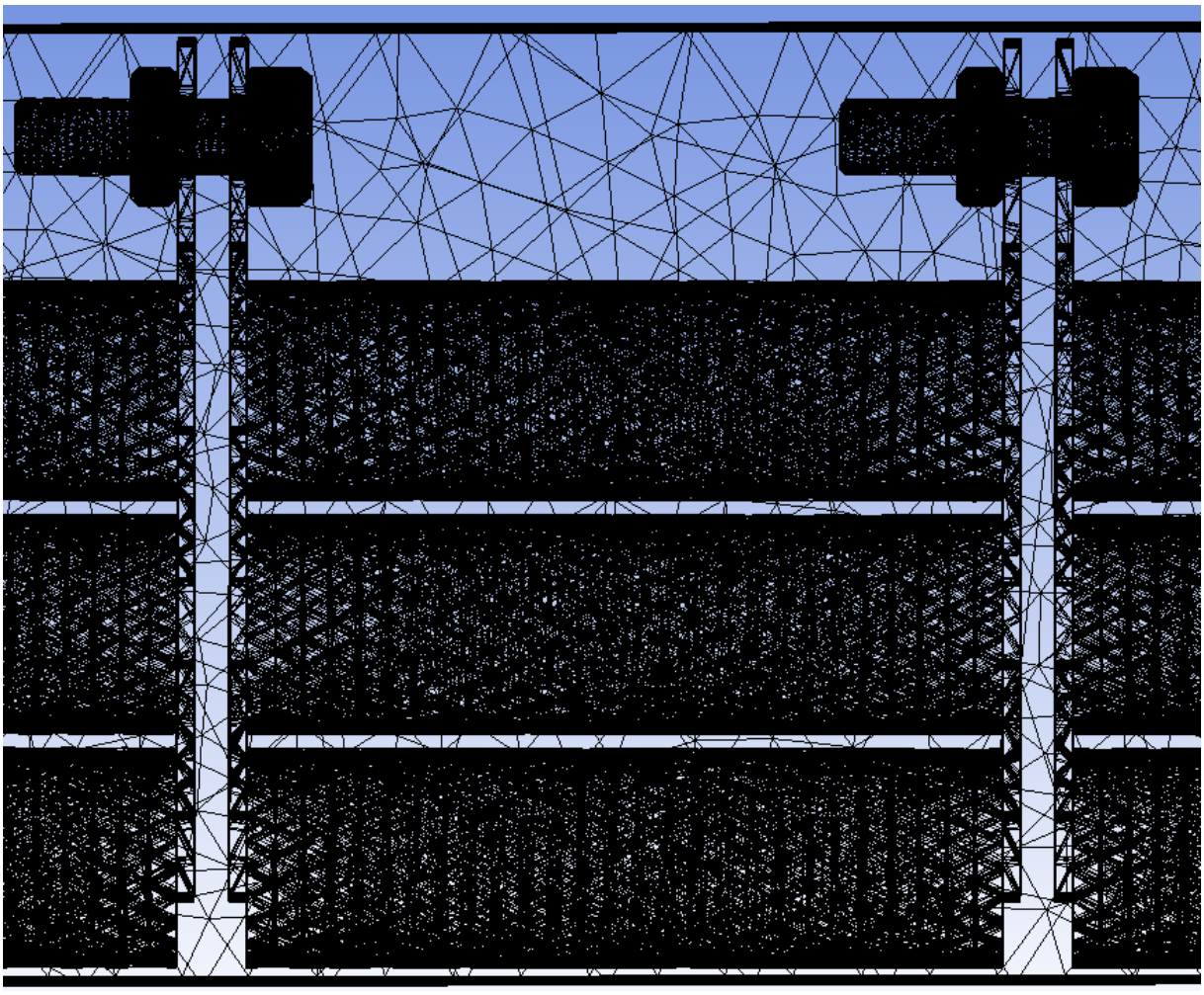

(b)

Figure 3-12. The front-view of the ESS mesh generated using ANSYS ICEM Meshing. (a) The BARR and (b) close-up of a single battery module.

3.4.5 Cell Zone, Boundary, and Initial Conditions

The configuration used for the thermal analysis of the FUSEV's enclosure was based upon the validated baseline model, and simulated with only minor changes made to its configuration. In particular, FLUENT was configured to simulate a real-world scenario in which normal operation of the ESS causes the bodies it encompasses to reach a global temperature of 26.85 °C. This prompts the temperature sensors within the enclosure to signal the BMS to turn on the ACFs which directs air at an ambient temperature of 20 °C at 2.64 m/s into the enclosure.

The above-mentioned scenario was simulated in an experimental manner whilst ensuring that the results obtained were consistent. This was done by keeping independent variables constant, to ensure that the results produced were solely reliant on the effects of select dependant variables. A pressure-based solver was used to solve all equations concerning the 3D volume defined by both the components and the fluid geometry internal to the enclosure. The energy equation was used to solve the heat transfer equations that concerns the cooling effect inherent of the heat dissipation resultant of the moving fluid domain which is at a lower temperature than the components. As the Rayleigh number calculated indicated a weak buoyancy-driven flow, the laminar viscous model was selected to be representative of the air-flow. Only the effects of the radial heat transfer of the components were considered because the magnitude of radial heat transfer is substantially bigger than axial heat transfer [51]. The general and model conditions defined for the thermal simulation were as detailed within Table 3-7.

Table 3-7. General and Model Conditions defined for the Thermal Simulation.

Category	**Option**
Solver Type Definition	Pressure-Based
Space Definition	3D
Energy	On
Viscous	Laminar
Radiation	Surface to Surface
Gravitational Acceleration	X: 0 m/s^2
	Y: 0 m/s^2
	Z: -9.81 m/s^2

As the components were composed of different materials they had to be assigned the thermophysical properties of said materials to observe realistic thermal behaviour. The thermophysical properties of the materials used within the simulation were as detailed within Table 3-8. The cell zone conditions that define their assignment to said components were as detailed within Table 3-9.

Table 3-8. Thermophysical properties of the BARR model materials.

Material	**Density (kg/m3)**	**Specific Heat (J/kg·K)**	**Thermal Conductivity (W/m·K)**	**Viscosity (kg/ms)**
Air	1.225	1006.43	0.0242	1.7894e-05
Stainless-Steel [84]	8060	530	17	-
Nickel	8900	460.60	91.74	-
Copper	8978	381	387.6	-
Brass [85]	8550	376	120	-
PBT [86]	1310	1000	0.25	-
ABS [87]	1060	1300	0.21	-
Fiberglass [88]	2600	805	1.35	-

Table 3-9. Cell Zone Conditions defined for Material Assignment.

Zone	**Material Definition**
18650 Battery Spacers	ABS
18650 Cells	Stainless-Steel
ACF	PBT
Bolts	Brass
Busbar	Copper
Fiberglass	Fiberglass
Nuts	Brass
Tabbing Material	Nickel

The operational specifications of the ESS used to simulate the aforementioned scenario with regard to the regions and bodies of interest were defined within the boundary conditions as detailed within Table 3-10. The under-relaxation factors used to stabilize the solution in order to reach convergence were as detailed within Table 3-11.

Table 3-10. Boundary Conditions defined for the Bodies and Areas of Interest.

Category	**Option**
Enclosure Inlet	
Type Definition	Velocity-Inlet
Velocity Magnitude	2.64 m/s
Initial Gauge Pressure	0 Pa
Temperature	20 °C
Enclosure Outlet	
Type Definition	Pressure-Outlet
Gauge Pressure	0 Pa
Temperature	20 °C
Enclosed Bodies	
Temperature	26.85 °C

Table 3-11. Under-Relaxation Factors defined for Solution Controls.

Category	**Option**
Pressure	0.3
Density	1
Body Forces	1
Momentum	0.7
Energy	1

3.4.6 Thermal Analysis Results

The thermal response of the BARR within each design iteration of the enclosure due to the conditions resultant of the aforementioned scenario is as presented within Table 3-12. In particular, it was the highest and lowest temperatures of the components used within the BARR after convergence, that was documented. The results of the thermal analysis showing the airflow and heat distribution throughout each design iteration of the enclosure is included within Appendix H.

Through a quantitative analysis of the component temperatures and a visual inspection of the airflow throughout the enclosure, the 16th iteration of the enclosure design was selected to be best suited for FUSEV's purposes. This design was selected as it had decreased the maximum cell temperature to the lowest temperature of all the designs analysed; it is crucial that the cell temperature be reduced to the lowest possible temperature to avoid the occurrence of thermal runaway. Specifically, with this design there was a decrease in cell temperature of 7.20% to 26.10%; decrease in busbar temperature of 16.80% to 19.10%; decrease in nut and bolt temperature of 13.30% to 20.20%; and decrease in tabbing material temperature of 7.00% to 20.10% from the initial global temperature of 26.85 °C.

Figure 3-13, shows that at the enclosure's inlets, the air-flow is widely distributed across the surface of the BARR along the inlet side. Consequently, as expected the temperature of the cells, busbar, nuts, bolts and tabbing material is at its lowest nearer to the inlet. Figure 3-14, shows the outflow of air occurs along the top and sides of the BARR. This behaviour is as expected due to the abrupt pressure variation across the enclosure, resultant of the limited internal volume and the BARR's displacement from the outlet. The nature of the airflow results in a reduced cooling effect on the cells located at the base. Figure 3-15, shows that the use of four inlets and four outlets allows for the airflow to adequately cover the BARR and internal enclosure volume. Figure 3-16, shows the distribution of cell temperature across the base of the BARR. The cells at the base of the battery modules located nearest to the outlets were least affected by the cooling employed. Figure 3-17 and Figure 3-18, show the front and rear of the enclosure. Figure 3-19, shows the heat distribution across the BARR, the differences in the thermal conductivity of the materials that compose the BARR, distribution of air-flow within the enclosure, and consequently, the effectiveness of the cooling it has across the BARR.

Table 3-12. The results from the CFD thermal analysis of all enclosure design iterations and the temperatures of all enclosed components.

			NCR18650BF Cells		**Busbar**		**Nuts and Bolts**		**Tabbing Material**	
Design Iteration	**Inlet Diameter (mm)**	**Outlet Diameter (mm)**	Max Temp (°C)	Min Temp (°C)	Max Temp (°C)	Min Temp (°C)	Max Temp (°C)	Min Temp (°C)	Max Temp (°C)	Min Temp (°C)
1	30	30	27.789	22.518	25.106	22.698	25.798	21.303	27.696	22.382
2	30	40	49.121	21.424	29.545	15.788	58.818	22.754	58.818	23.364
3	30	50	27.565	22.366	24.941	23.211	25.849	21.303	27.803	21.894
4	30	60	28.776	22.816	25.343	23.785	26.349	22.846	28.646	22.734
5	40	30	25.843	21.946	22.939	21.121	24.394	21.212	25.728	21.725
6	40	40	25.462	21.915	23.102	22.267	23.888	21.668	25.350	21.678
7	40	50	26.426	22.057	22.939	21.121	26.364	22.273	26.263	21.842
8	40	60	26.242	18.515	29.667	19.667	25.788	19.424	24.818	19.364
9	50	30	25.848	21.303	22.752	20.235	24.192	20.235	25.848	21.303
10	50	40	25.519	21.831	22.723	21.910	23.832	21.589	25.372	21.591
11	50	50	25.758	18.485	39.424	22.152	24.879	21.242	25.267	21.267
12	50	60	25.216	21.840	22.499	21.870	23.909	21.182	25.114	21.614
13	60	30	26.087	21.670	26.273	19.455	23.848	19.303	25.918	20.639
14	60	40	25.348	20.803	22.273	21.691	23.379	20.553	25.250	18.179
15	60	50	29.369	19.844	22.455	21.091	22.939	21.121	24.879	21.242
16	60	60	24.913	19.833	22.333	21.722	23.282	21.424	24.963	21.451

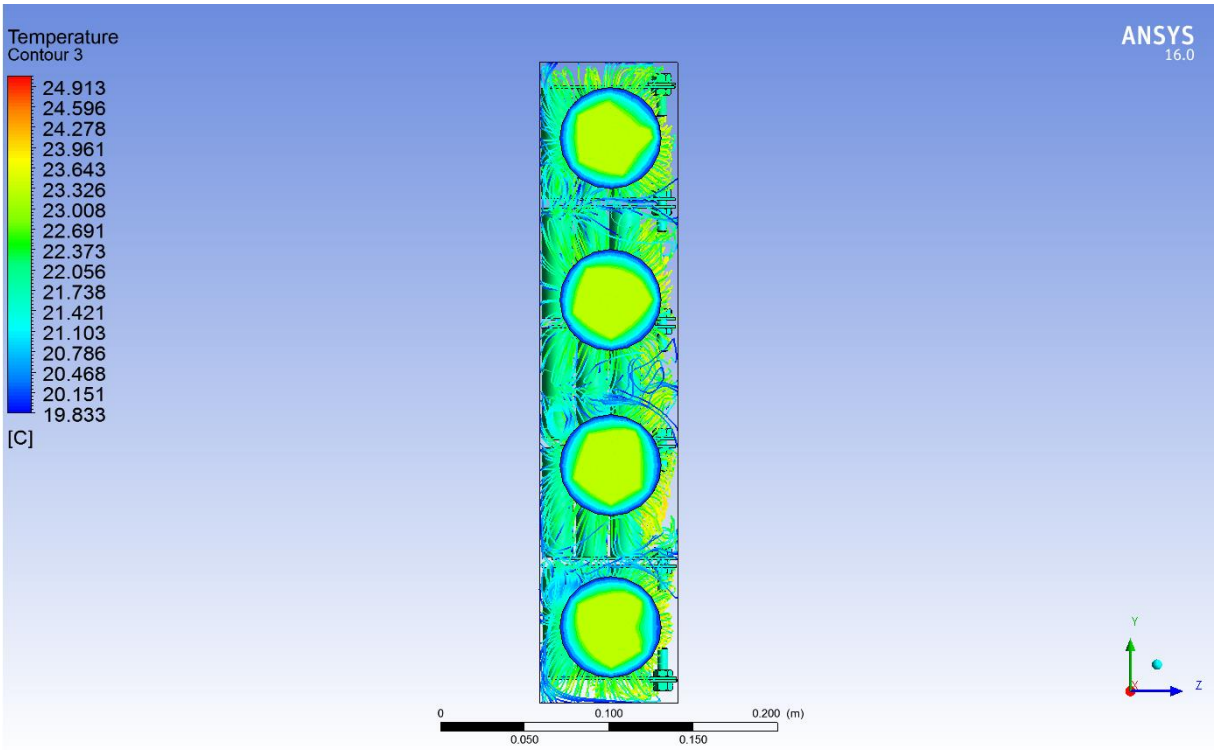

Figure 3-13. The side-view of the ESS enclosure with pressure distribution across its Inlets of 60 mm.

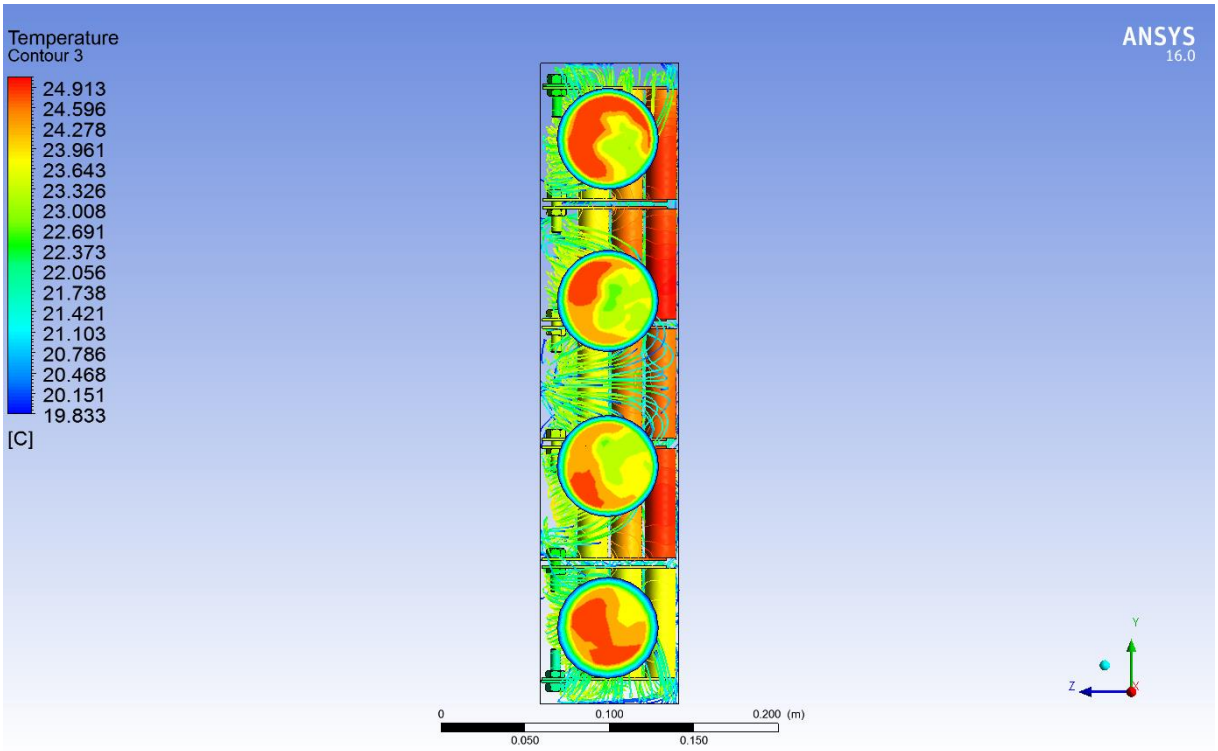

Figure 3-14. The side-view of the ESS enclosure with pressure distribution across its Outlets of 60 mm.

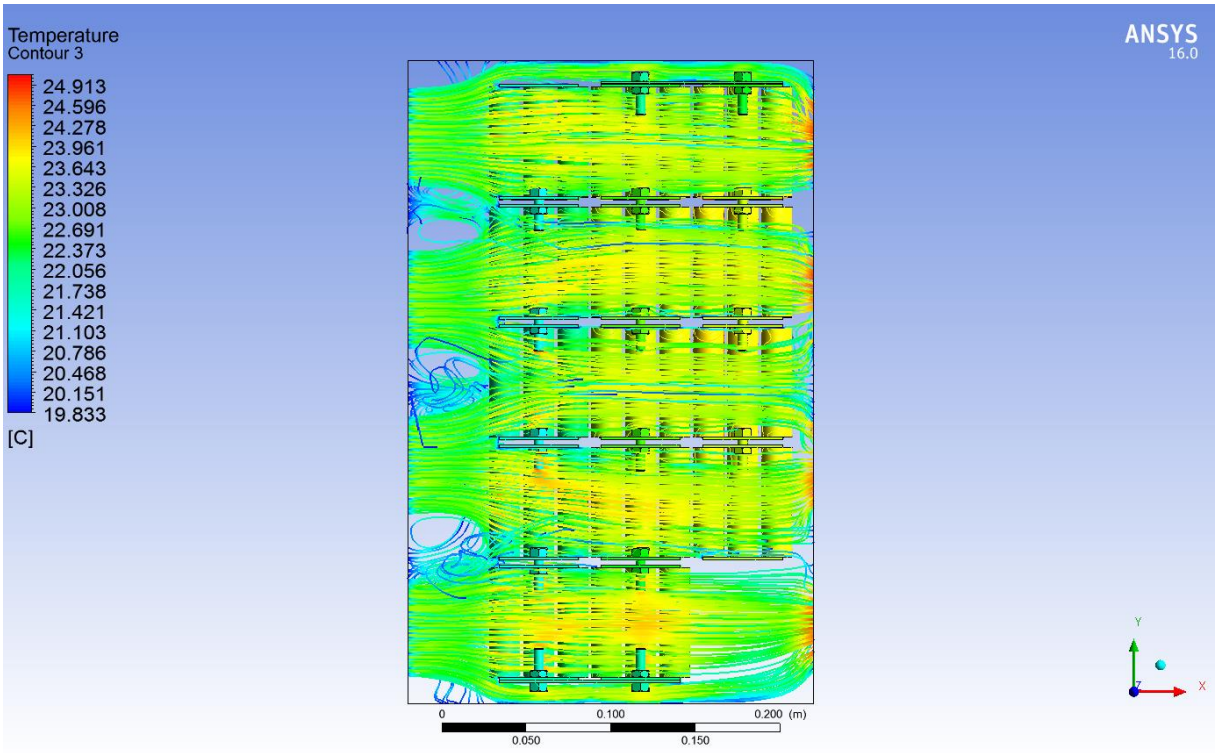

Figure 3-15. The top-view of the ESS enclosure with air-flow directed in through the Inlet of 60 mm and out through the Outlet of 60 mm.

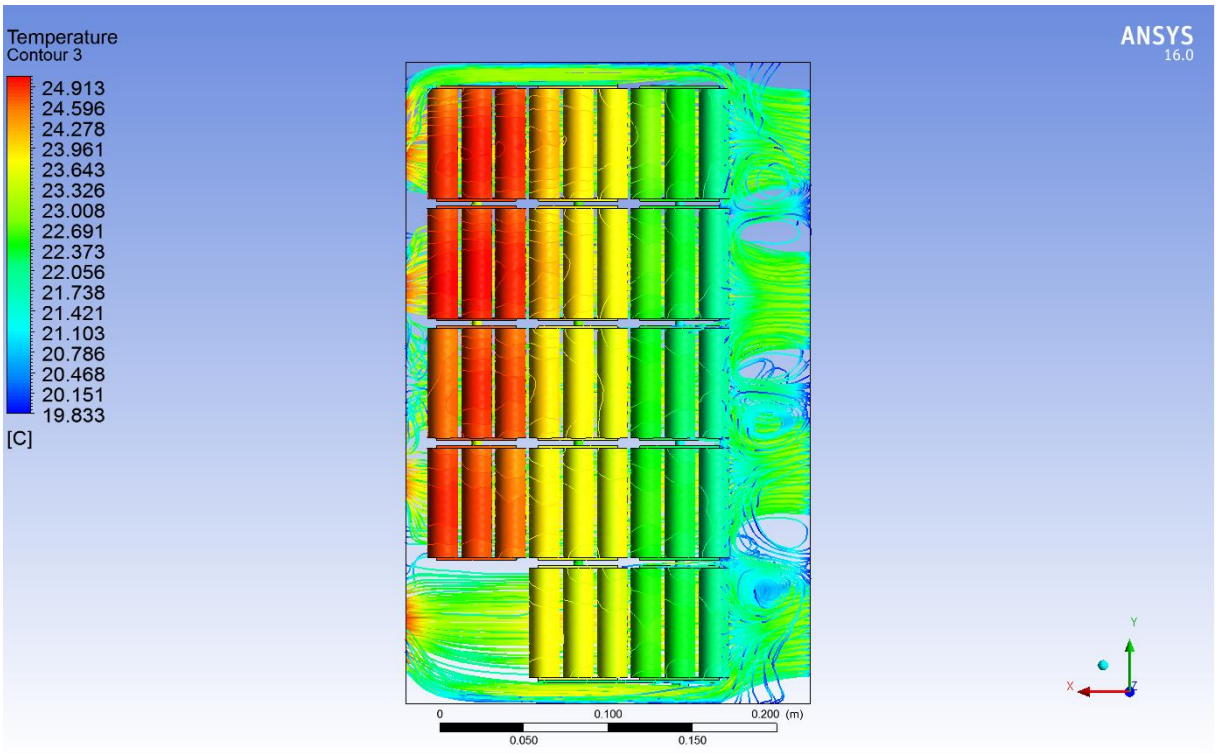

Figure 3-16. The base-view of the ESS enclosure showing the distribution of cell temperatures (°C) with respect to its positioning within the ESS enclosure.

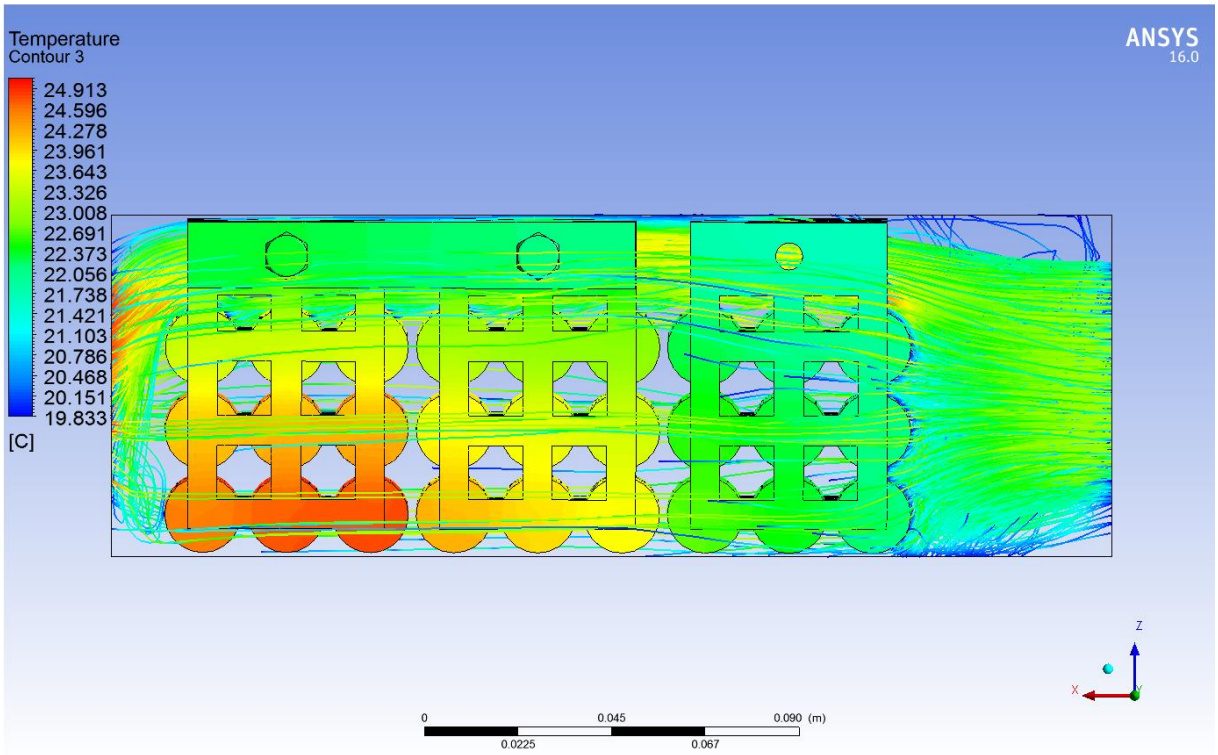

Figure 3-17. The front-view of the ESS enclosure showing the direction of air flow from the Inlet (right-side of the enclosure) to the Outlet (left-side of the enclosure) and the distribution of busbar, tabbing material, nut, and cell temperatures (°C).

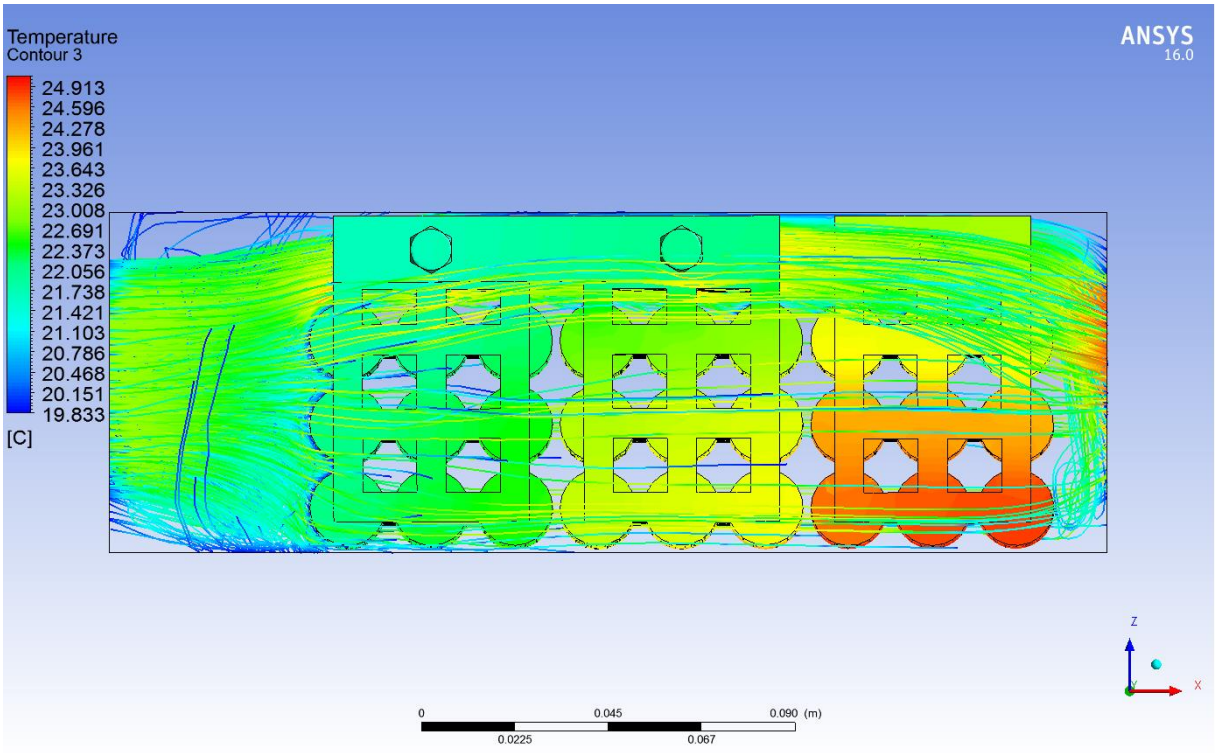

Figure 3-18. The rear-view of the ESS enclosure showing the direction of air flow from the Inlet (left-side of the enclosure) to the Outlet (right-side of the enclosure) and the distribution of busbar, tabbing material, nut, and cell temperatures (°C).

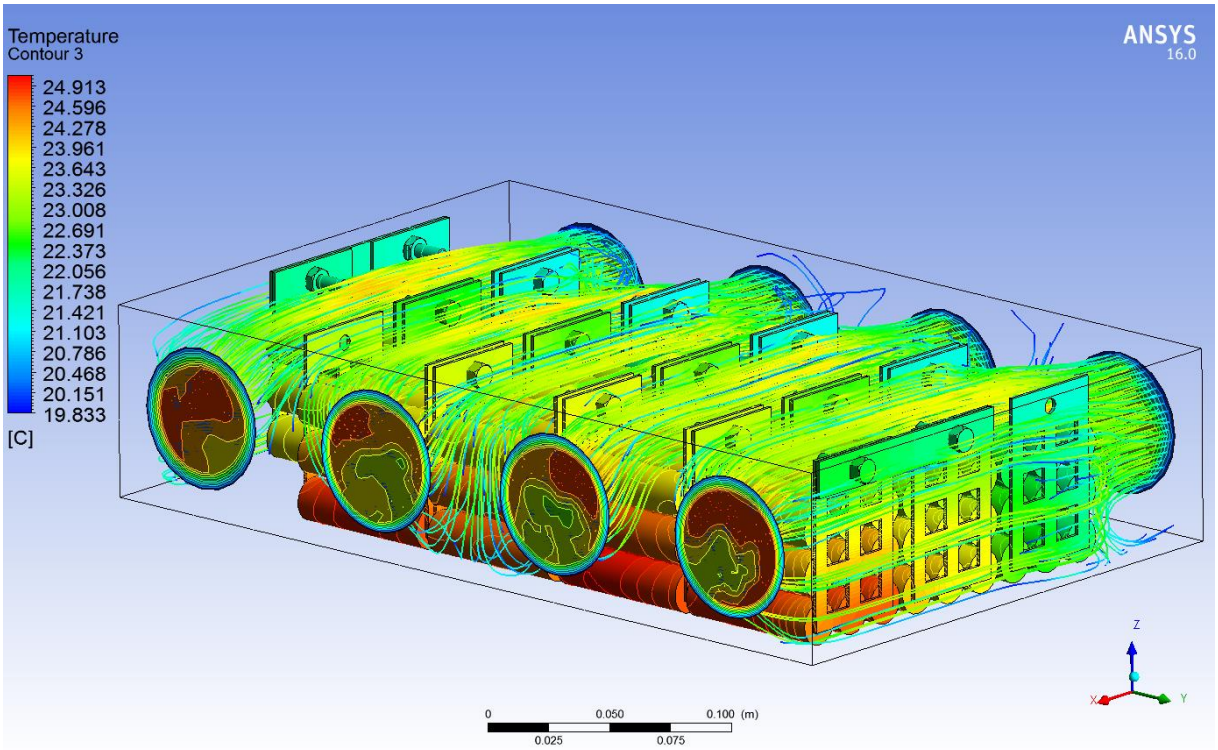

Figure 3-19. The isometric-view of the ESS enclosure showing the direction of air flow and the distribution of busbar, tabbing material, nut, bolt, and cell temperatures (°C).

3.5 Enclosure Design and Assembly

With the generic form of the ESS enclosure determined through the thermal analysis, a modular design for its manufacture had to be developed. After a consultation with FAST, it was decided that Aluminium-6061 sheet metal should be used for the construction of the ESS enclosure; as it is lightweight, has high strength, is resistant to corrosion, and easy to fabricate. In particular, the use sheet metal would increase manufacturability as it can be folded into the required forms. As aluminium is both a thermal and electrical conductor, once constructed the enclosure is to be lined internally with fiberglass for thermal and electrical insulation. It is intended that the fiberglass be bonded to the aluminium using the Cyberbond 2243 adhesive [89]. The following sections detail the design of the various parts required to build the ESS enclosure.

3.5.1 Base Plate

The enclosure when assembled has to form a rigid structure. Through the consultation it was decided that a single sheet of aluminium should be folded to form the base and sides of the ESS enclosure. The base plate was designed to support the weight of the BARR, have mounting points for all fixtures, and hold the ESS structure together. The base plate was designed to include inlet and outlet openings, the dimensions of which were determined through the thermal analysis of the ESS. The key design features of the base plate are shown within Figure 3-20, Figure 3-21, and Figure 3-22. The mechanical drawings of the base plate are included within Appendix I.

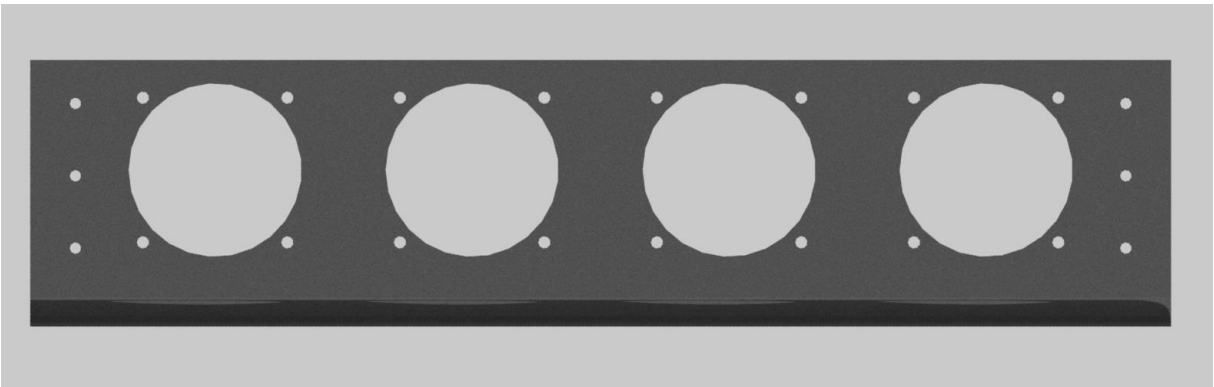

Figure 3-20. The side-view of the base plate, showing the ventilation openings of the enclosure and mounting points for the ACFs, front and rear plates.

Figure 3-21. The front-view of the base plate, showing the folded design feature of the base plate.

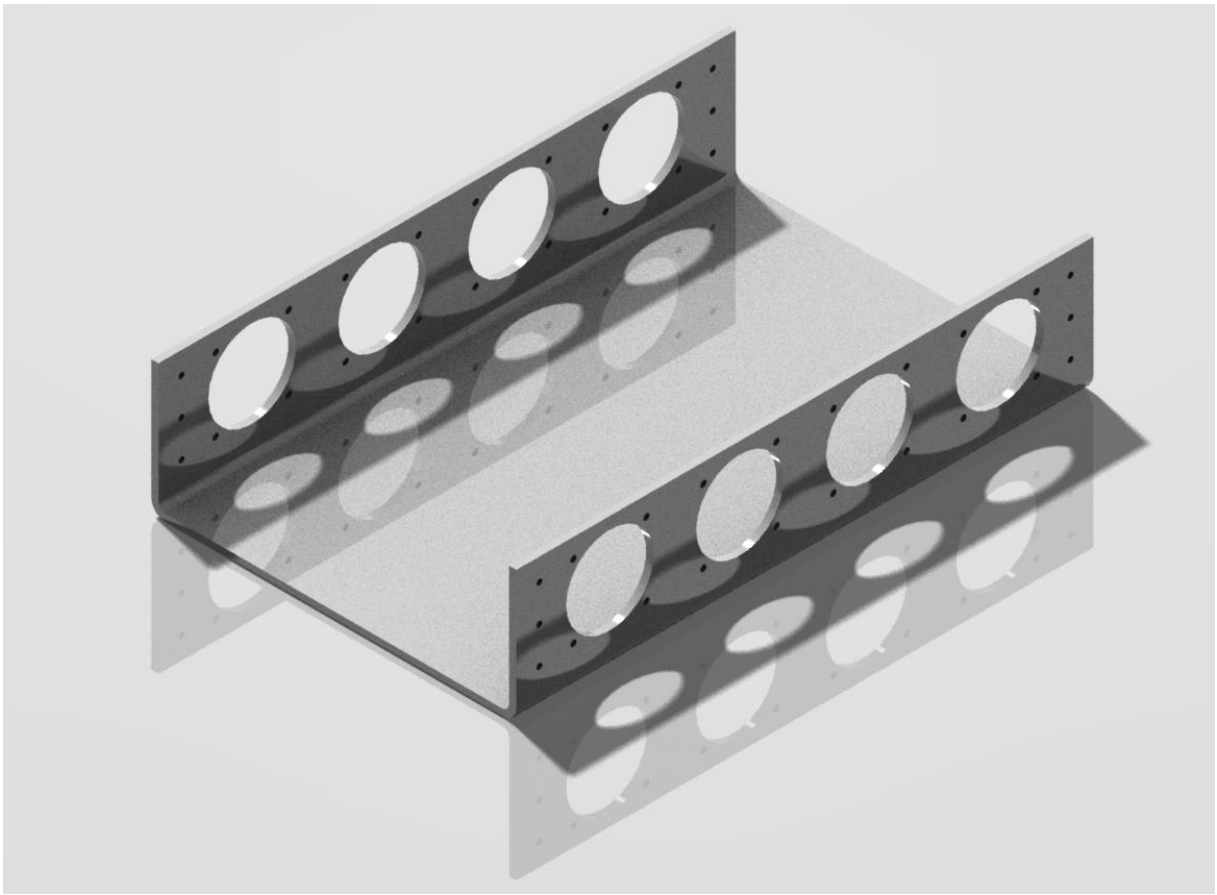

Figure 3-22. The isometric-view of the base plate.

3.5.2 Front and Rear Plates

The front and rear plates of the enclosure were designed to be fitted to the base plate whilst being easily removable to allow for direct access to the BARR. Furthermore, these plates were designed such that all of the cabling wired to the BARR enters the enclosure via the openings on these plates. These openings will include rubber cabling grommets to ensure that the cabling does not get damaged by sharp edges. The key design features of the front and rear plate are shown in Figure 3-23 to Figure 3-28. The mechanical drawings of the front and rear plates are included in Appendix K and J respectively.

Figure 3-23. The isometric-view of the front plate.

Figure 3-24. The top-view of the front plate.

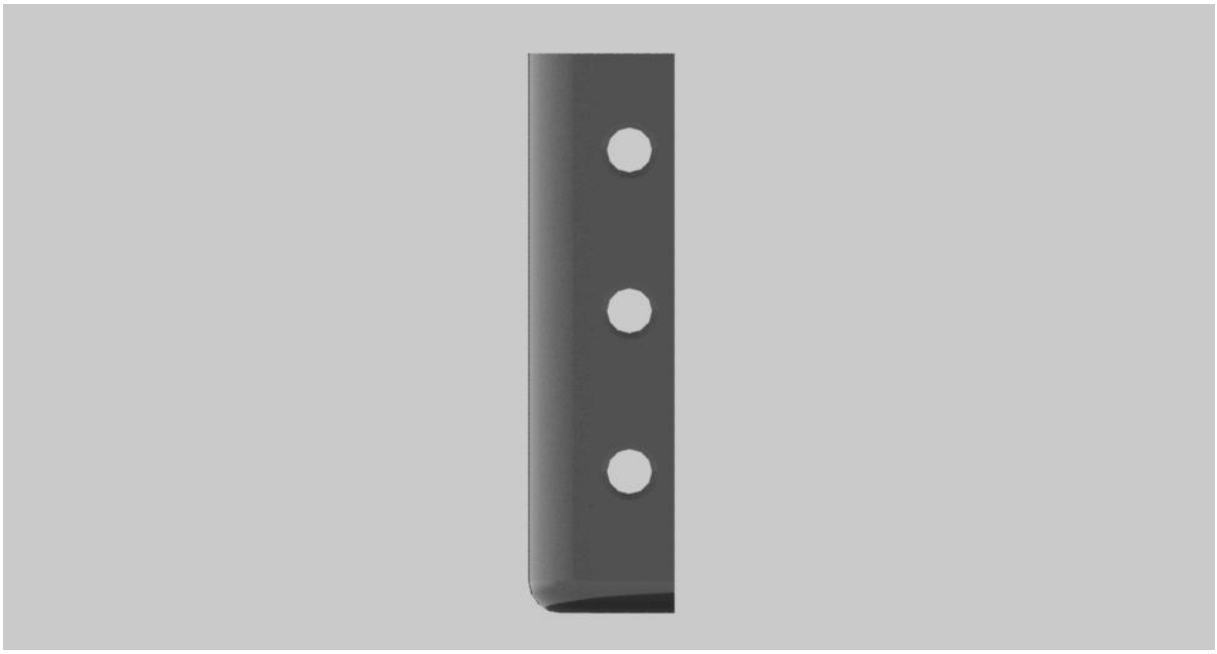

Figure 3-25. The side-view of the front plate.

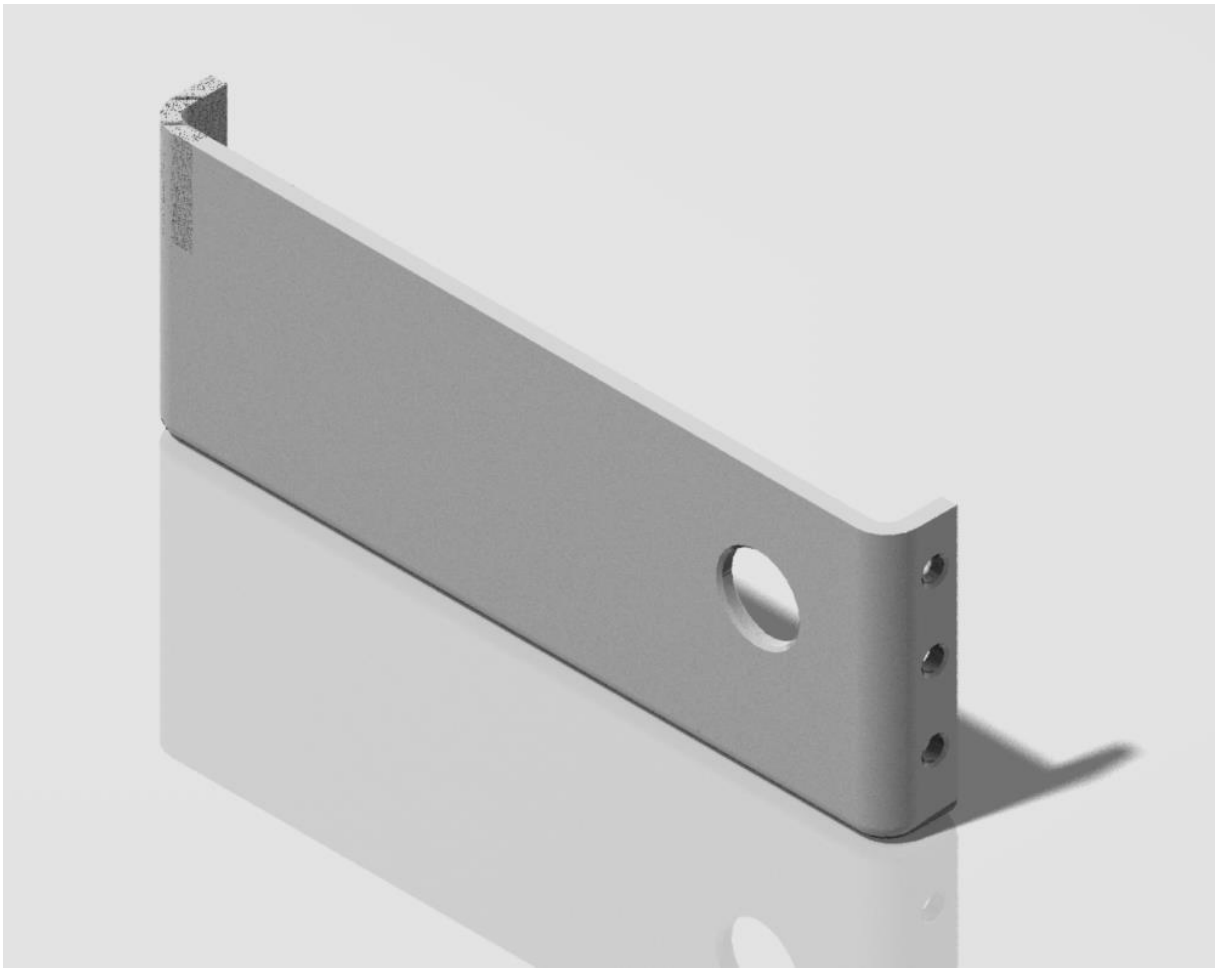

Figure 3-26. The isometric-view of the rear plate.

Figure 3-27. The top-view of the rear plate.

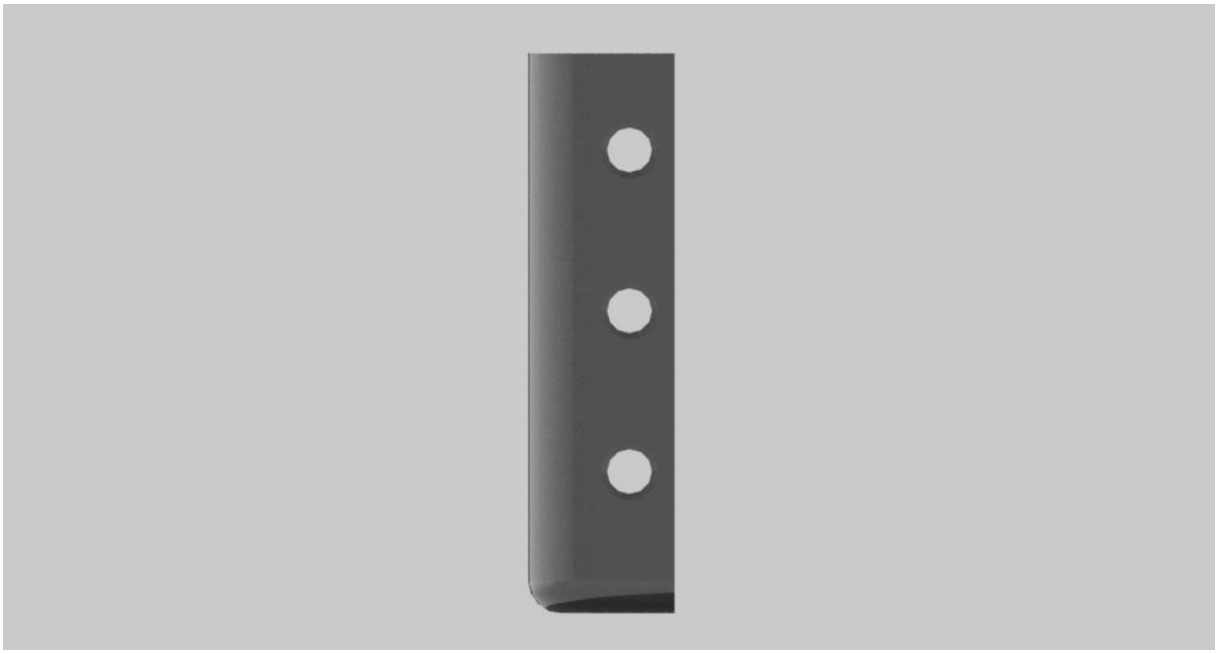

Figure 3-28. The side-view of the rear plate.

3.5.3 Top Plate

The top plate of the enclosure was designed to be easily removable for access to the BARR and the fixtures within the enclosure. The top plate was designed as a single aluminium sheet that uses two aluminium angles to hold the top plate in place to reduce movement and form a tight seal. The aluminium angles are to be welded onto the top plate. The top plate includes mounting points for the installation of a handle onto it, to allow for the top plate to be easily removed from the enclosure. Figure 3-29, shows the top plate of the ESS, Figure 3-30 shows the side view of the top plate, and Figure 3-31 shows the exploded view of the top plate.

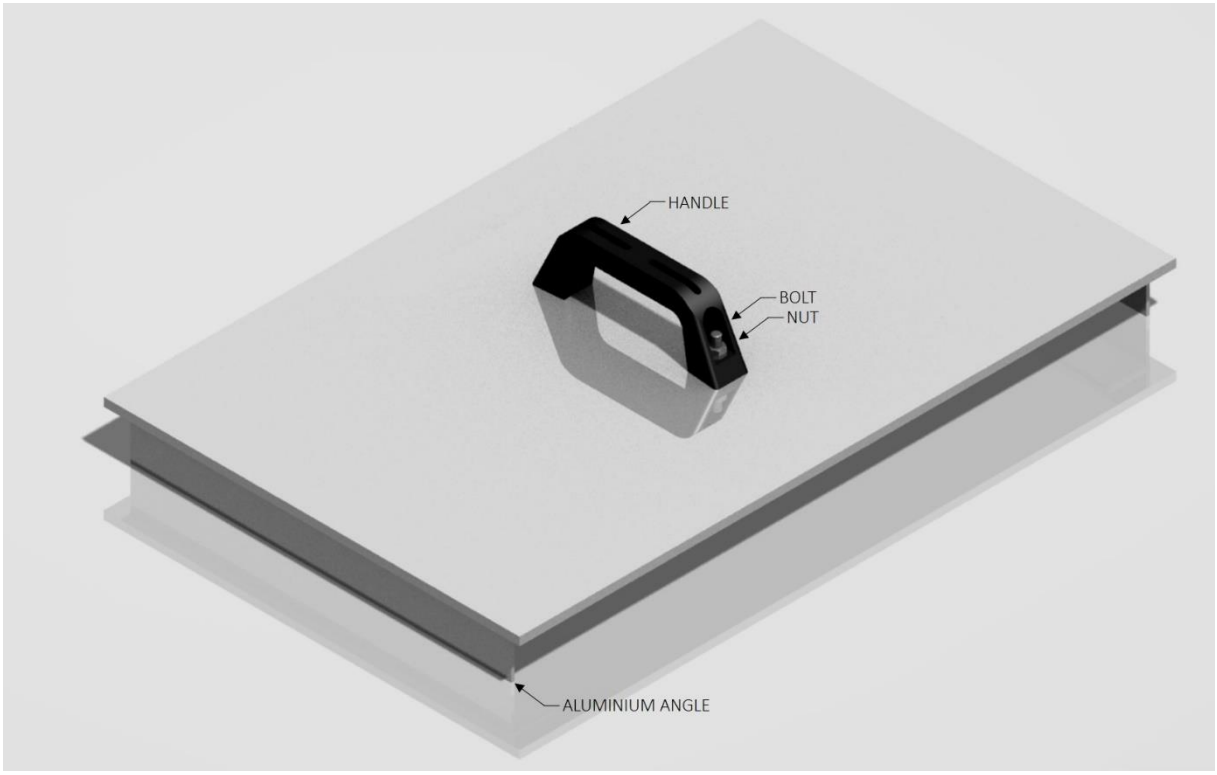

Figure 3-29. The isometric-view of the top plate.

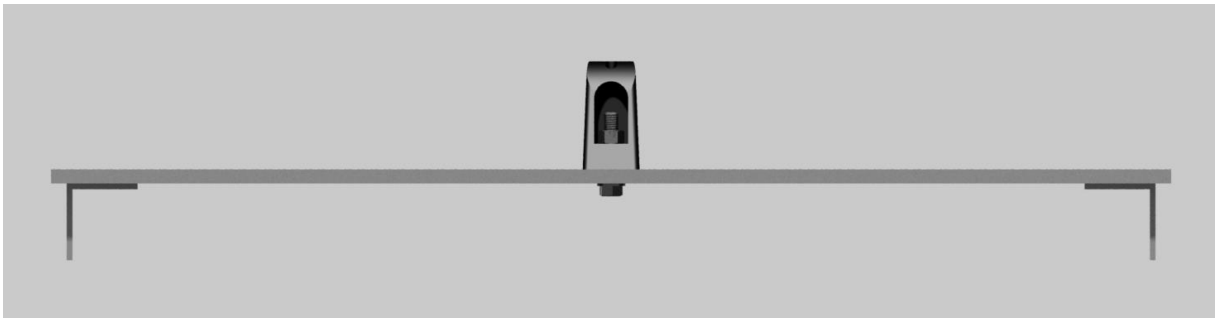

Figure 3-30. The side-view of the top plate, showing the positioning of the welded aluminium angles.

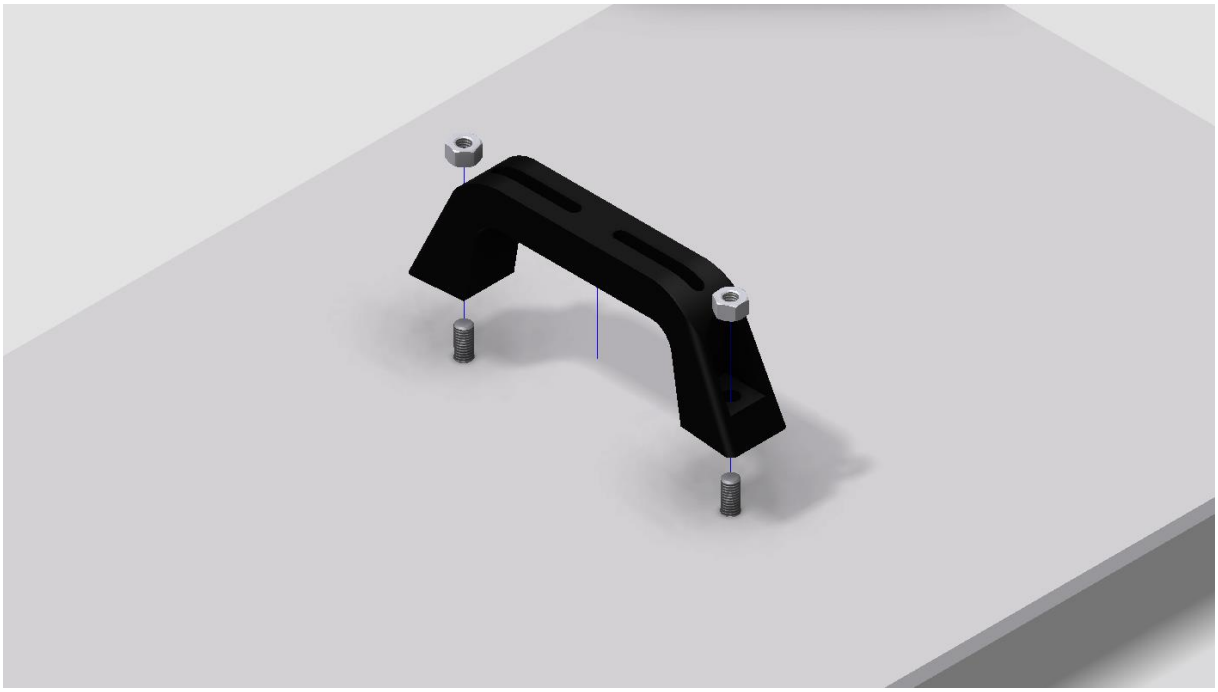

Figure 3-31. The exploded view of the top plate, showing the assembly of the top plate.

3.5.4 Enclosure Assembly

It was ascertained that the front and rear plates need be installed using stainless-steel rivet nut inserts as shown in Figure 3-32 to Figure 3-36. Without the use of the rivets, repeated insertion or removal of metal threaded screws would cause the ingrained threads on the enclosure to wear out as it is composed of aluminium. As the enclosure was designed to be assembled of standardized components, all of the required parts listed within Appendix D can be locally sourced.

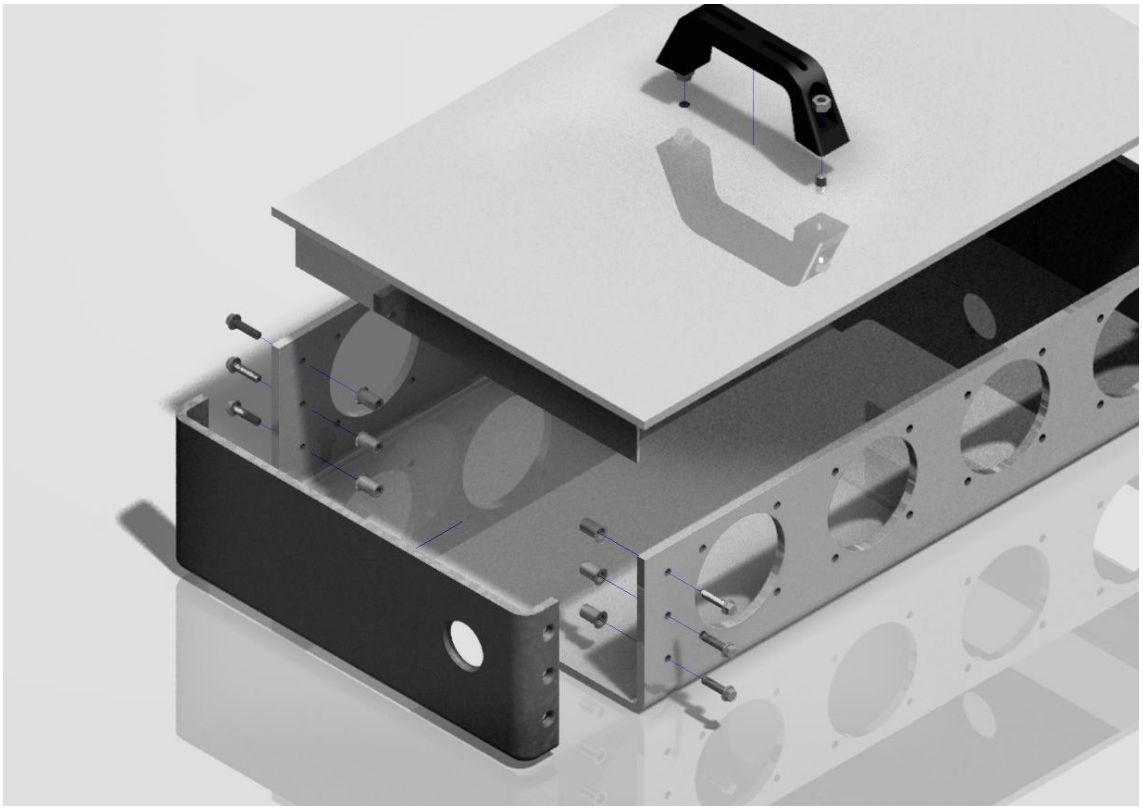

Figure 3-32. The exploded-view of the fully assembled ESS enclosure.

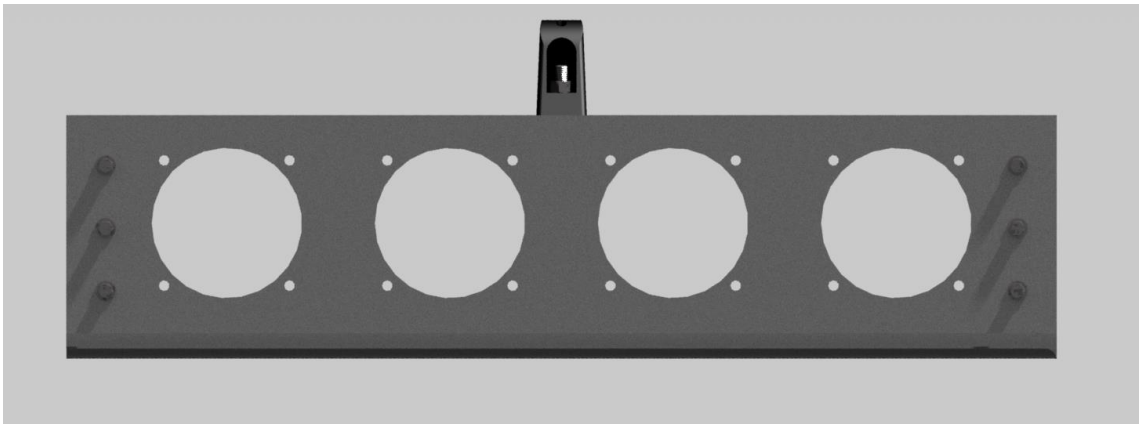

Figure 3-33. The side-view of the fully assembled ESS enclosure.

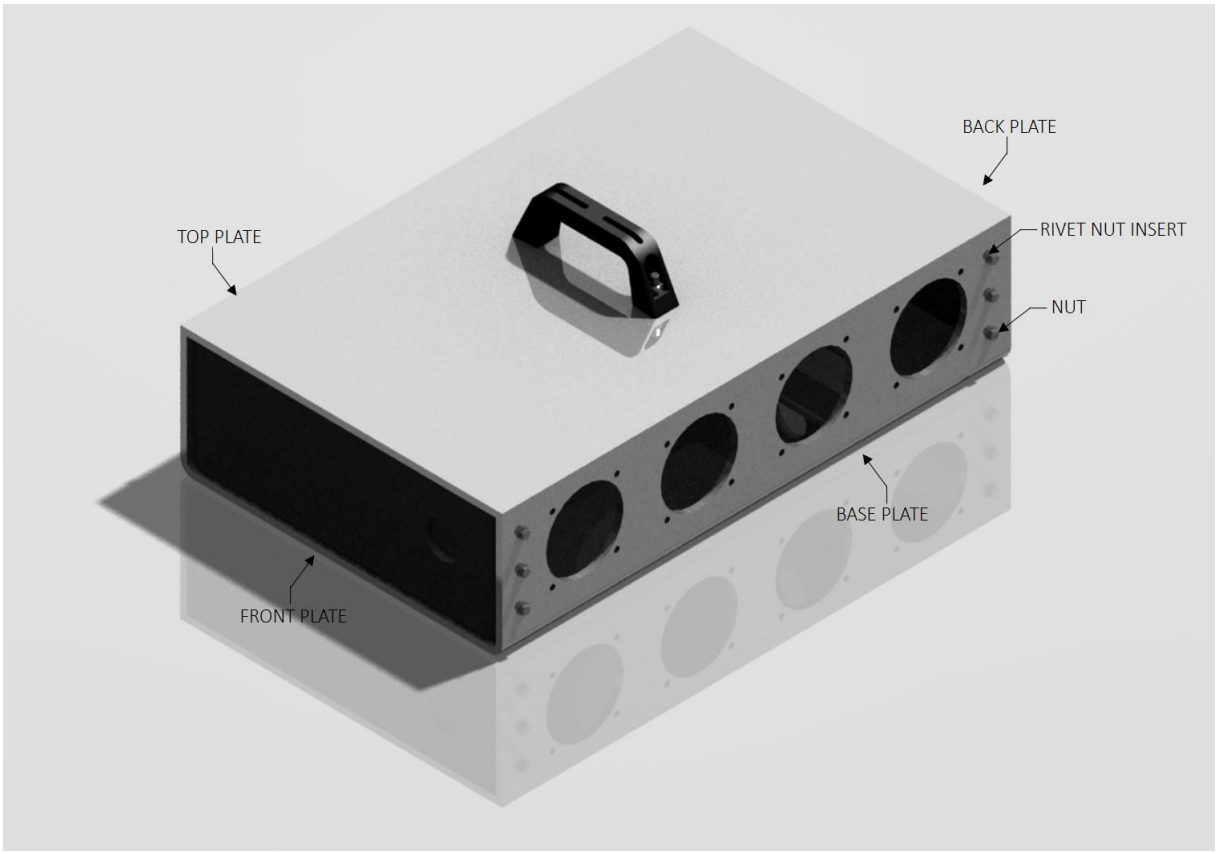

Figure 3-34. The isometric-view of the fully assembled ESS enclosure.

Figure 3-35. The back-view of the fully assembled ESS enclosure.

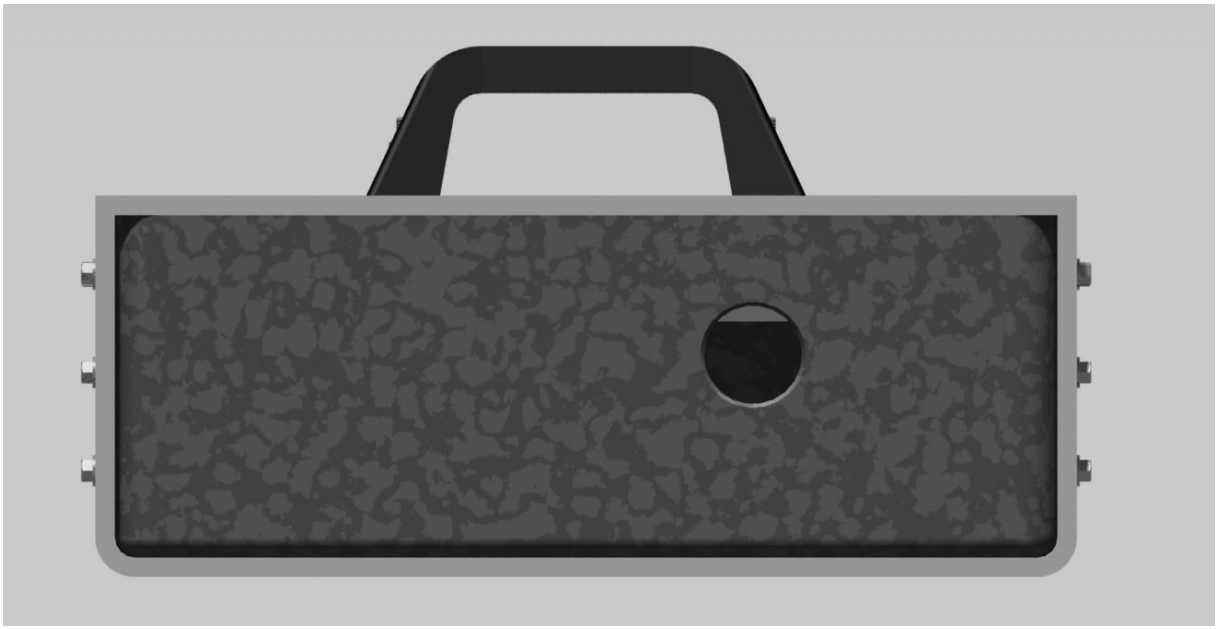

Figure 3-36. The front-view of the fully assembled ESS enclosure.

3.5.5 ESS Assembly

The ESS when fully assembled will be inclusive of the enclosure, BARR, finger guards, ACFs and VFs. Consequently, the ESS will resemble the assembly shown in Figure 3-37 to Figure 3-40. The finger guards, ACFs and VFs used within the model were those designed for 60mm ventilation openings. As the enclosure was designed to accommodate standardized parts, any make or model of the finger guards, ACFs and VFs should suffice; however, it is recommended that those mentioned within the parts list in Appendix D be used. The mechanical drawings of the assembled ESS inclusive of all fixtures and components is included within Appendix N.

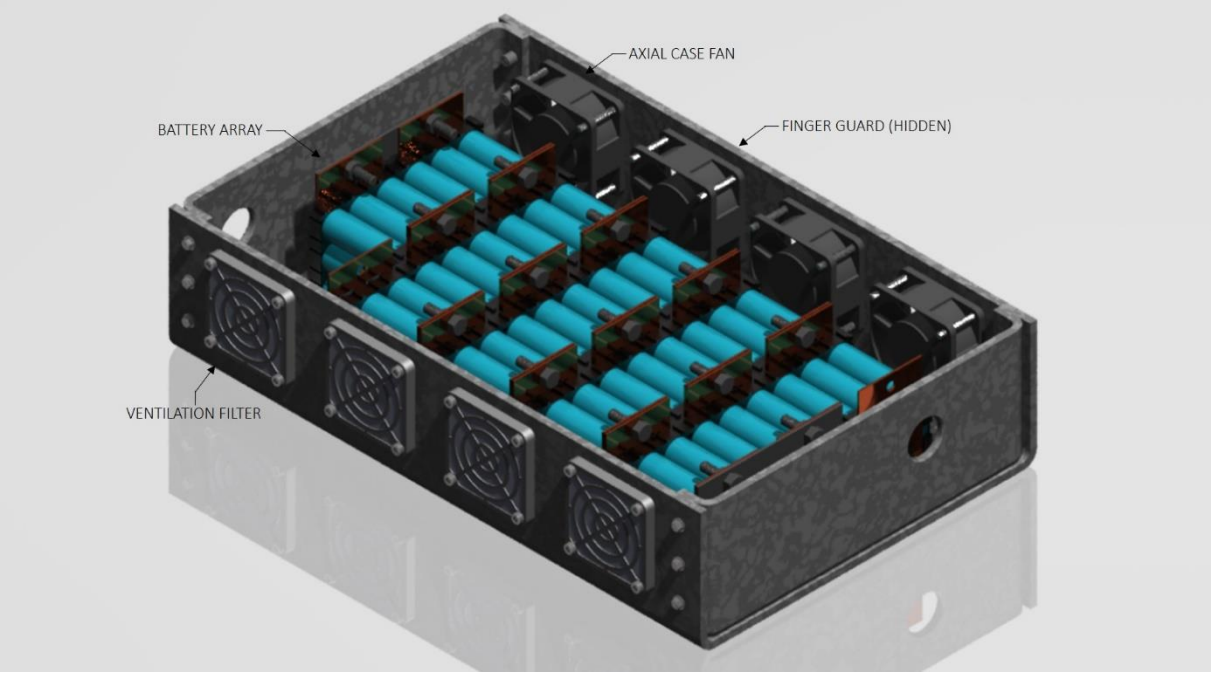

Figure 3-37. The isometric-view of the fully assembled ESS inclusive of the enclosure, BARR, finger guards, VFs, and ACFs.

Figure 3-38. The side-view of the ESS enclosure's inlets, showing the use of finger guards and ACFs.

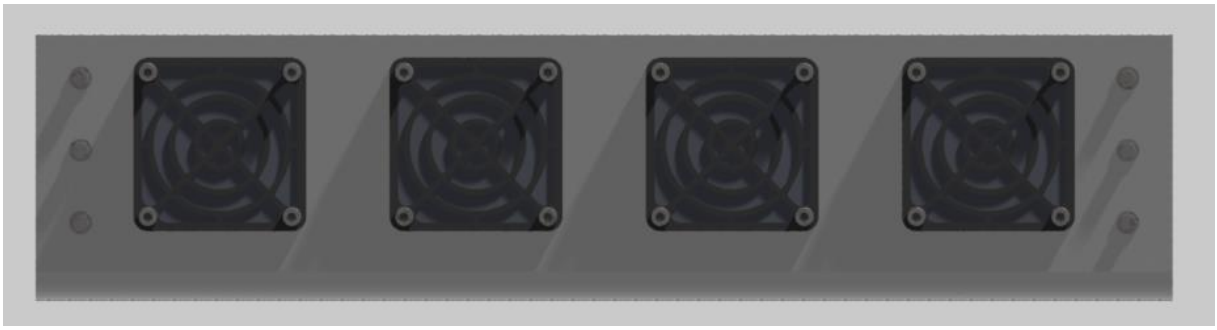

Figure 3-39. The side-view of the ESS enclosure's outlets, showing the use of VFs.

Figure 3-40. The top-view of the fully assembled ESS inclusive of the enclosure, BARR, finger guards, VFs, and ACFs.

3.6 Finite Element Stress Analysis

The enclosure design developed was subjected to a finite element stress analysis using the Autodesk Inventor package. The objective of this analysis was to predict the occurrence of any design failures, and ensure that the material and assembly methods selected would adhere to the requirements stated within Clause 2.3 of Table 1-2. The following sections detail the mesh generation, the settings used to obtain the results and the analysis of the results generated.

3.6.1 Mesh Generation, and Analysis Settings

The stress analysis was conducted on the 3D model of the ESS enclosure design with the fixtures and the BARR omitted; to significantly reduce the computational effort. An unstructured mesh consisting of 545,721 tetrahedral elements was generated for the 20 bodies that composes the ESS enclosure, as shown in Figure 3-41. A minimum mesh size of 0.01mm and average mesh size of 0.05mm were selected for the analysis, ensuring that regions of interest were represented with a fine mesh.

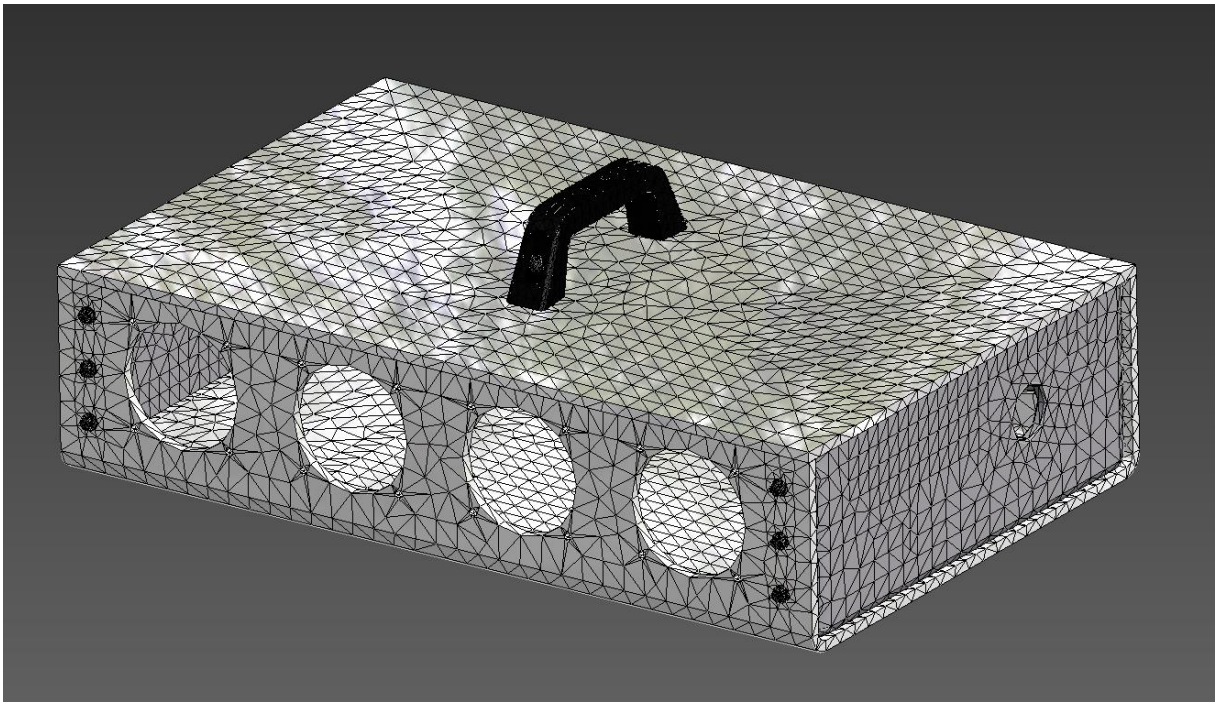

Figure 3-41. The isometric-view of the ESS enclosure mesh generated using Autodesk Inventor.

To confirm that the enclosure can withstand the crash accelerations mentioned within Clause 2.3 and support the weight of the batteries, Inventor was configured to subject the components of the enclosure to the load conditions defined within Table 3-13.

Table 3-13. The load conditions defined for the bodies and areas of interest.

Component	**Force (N)**
BARR	63.7
Crash Acceleration	**Force (N)**
Front Impact	130
Side Impact	97.5
Rear Impact	65
Vertical Impact	65

3.6.2 Stress Analysis Results

The displacement and Von Mises stress caused by each of the imposed load conditions upon the ESS enclosure is as given within Table 3-14. The simulation results of the displacement and Von Mises stresses were as shown in Figure 3-42 to Figure 3-51 on the following pages. The effect of the displacement was accentuated within the figures for ease of visual inspection.

Table 3-14. The results from the stress analysis of the load imposed upon the ESS enclosure and the resultant displacement.

Component	**Displacement (mm)**	**Von Mises Stress (MPa)**
BARR	0.01558	1.302
Crash Acceleration	**Displacement (mm)**	**Von Mises Stress (MPa)**
Front Impact	0.003679	1.192
Side Impact	0.002114	0.722
Rear Impact	0.001839	1.001
Vertical Impact	0.007744	1.931

From Table 3-14 and the figures, it can be validated that the design of the ESS enclosure meets all of the associated requirements. The displacement caused by the imposed loads were minuscule; consequently, insignificant enough to puncture the 18650 cells. The maximum Von Mises stresses observed on the ESS enclosure due to the imposed loads were significantly lower than the yield strength of aluminium at 275.159 MPa as defined within Inventor; consequently, no design failures occurred.

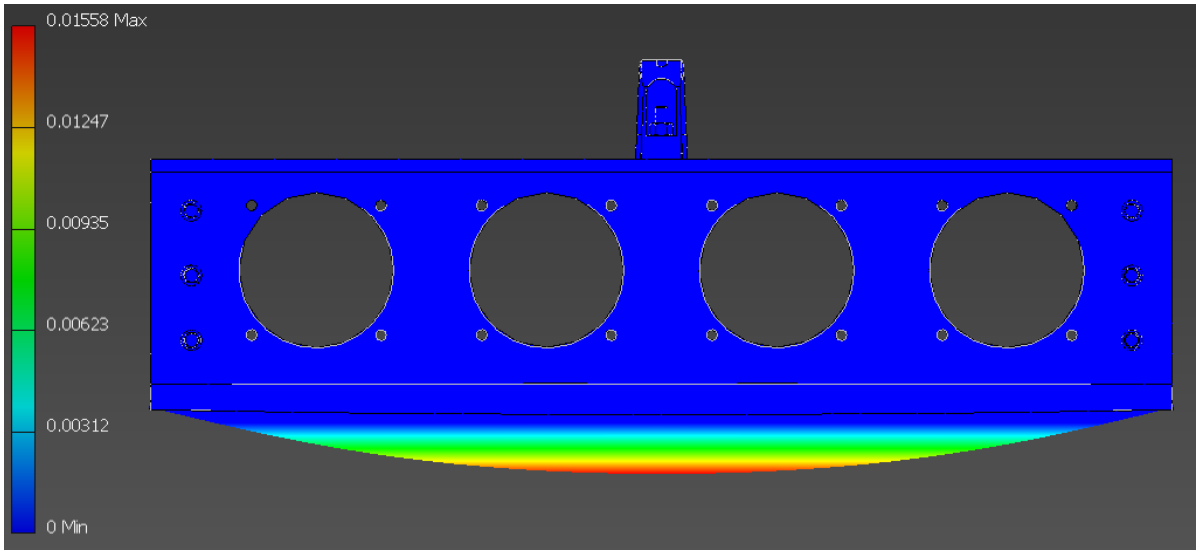

Figure 3-42. The displacement on the enclosure due to the weight of the BARR.

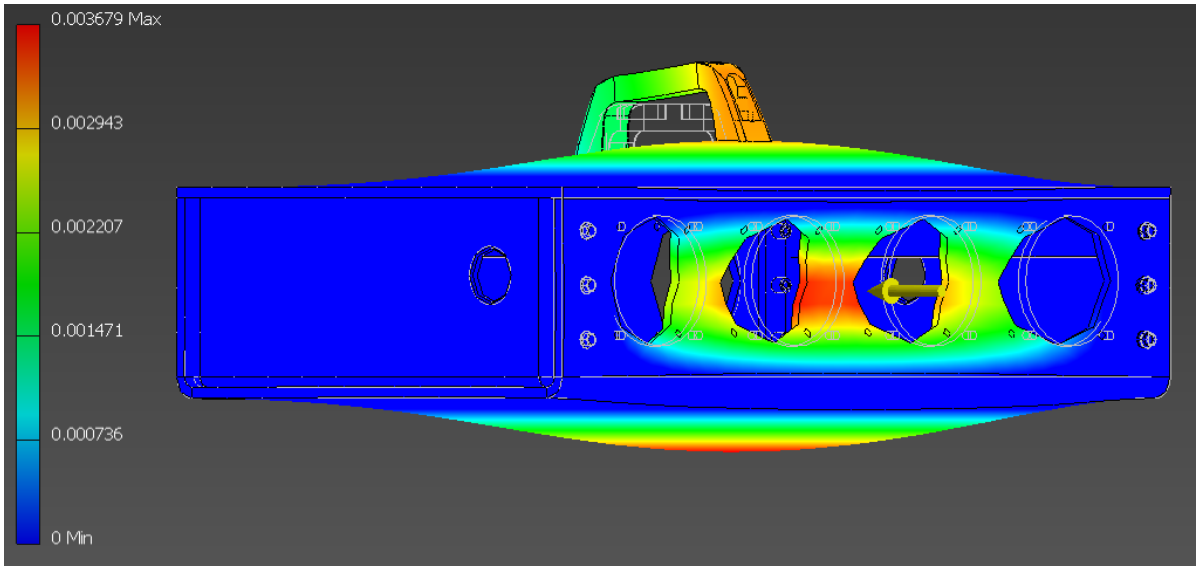

Figure 3-43. The displacement on the enclosure due to frontal impact.

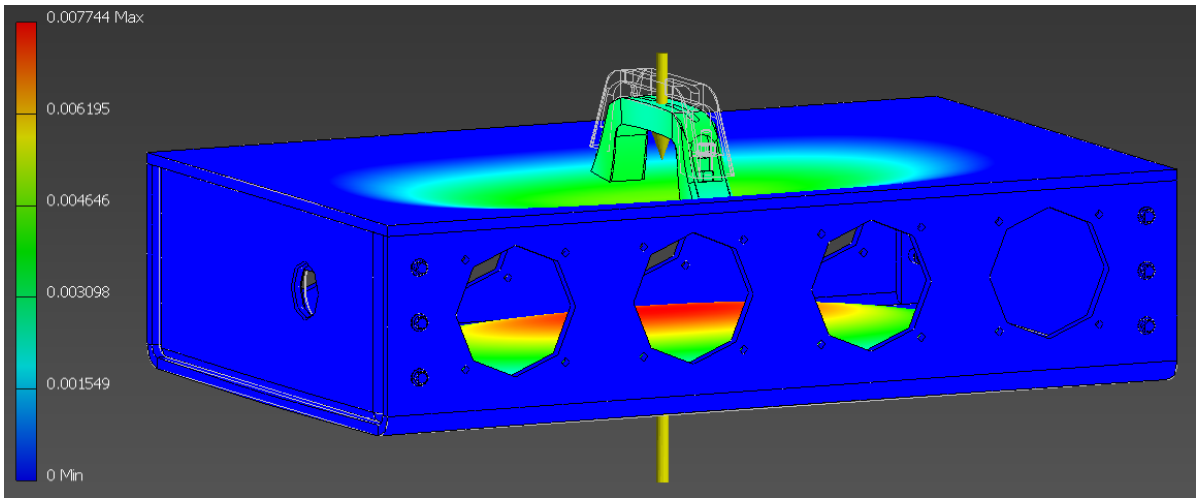

Figure 3-44. The displacement on the enclosure due to vertical impact.

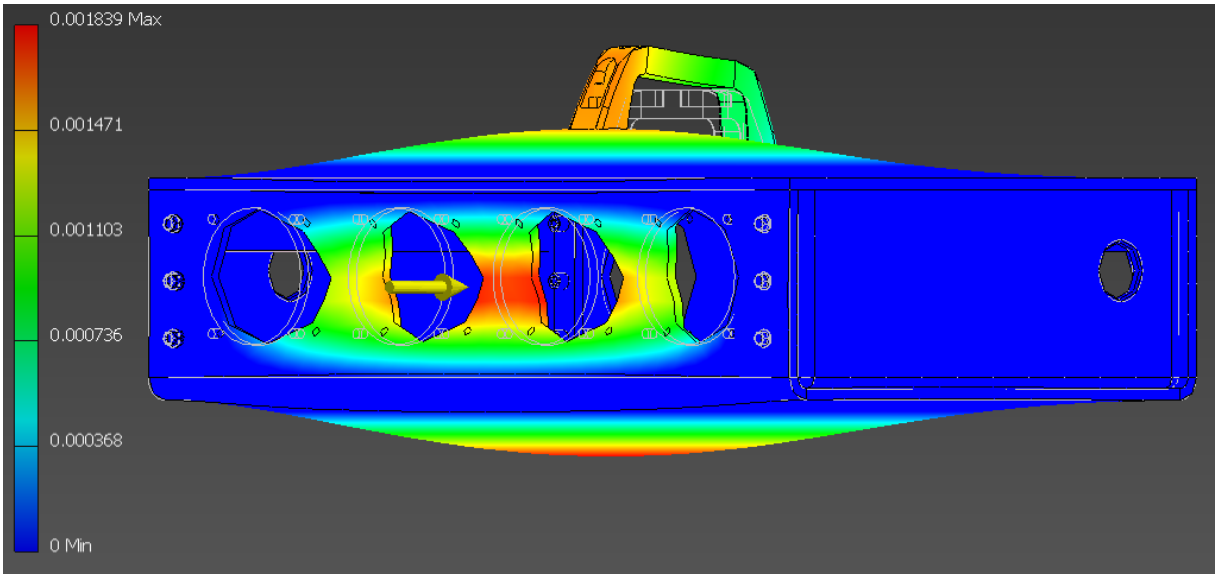

Figure 3-45. The displacement on the enclosure due to rear impact.

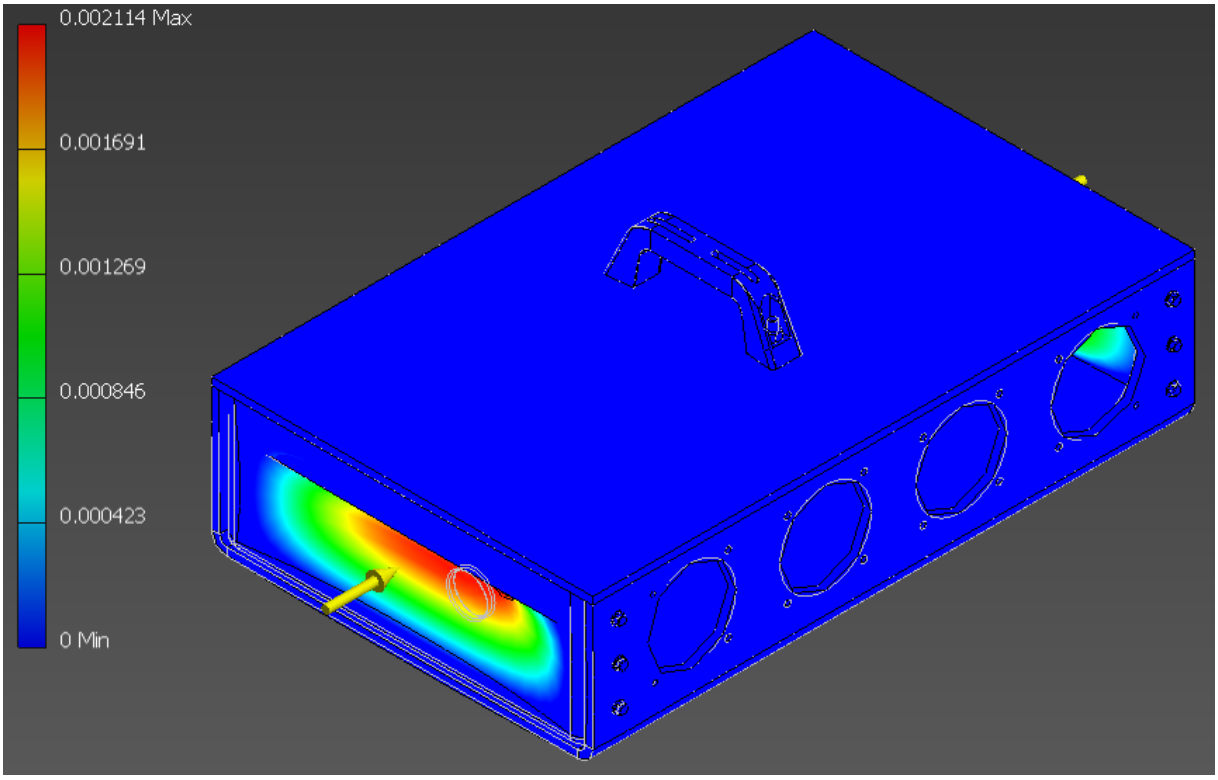

Figure 3-46. The displacement on the enclosure due to side impact.

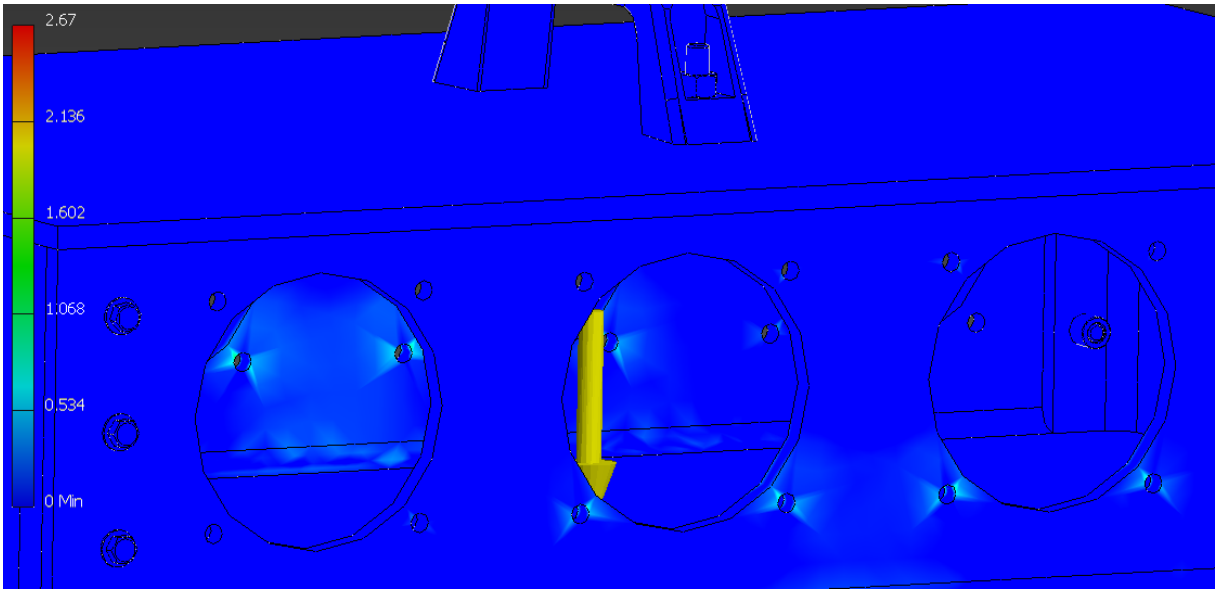

Figure 3-47. The Von Mises stresses on the enclosure due to the weight of the BARR.

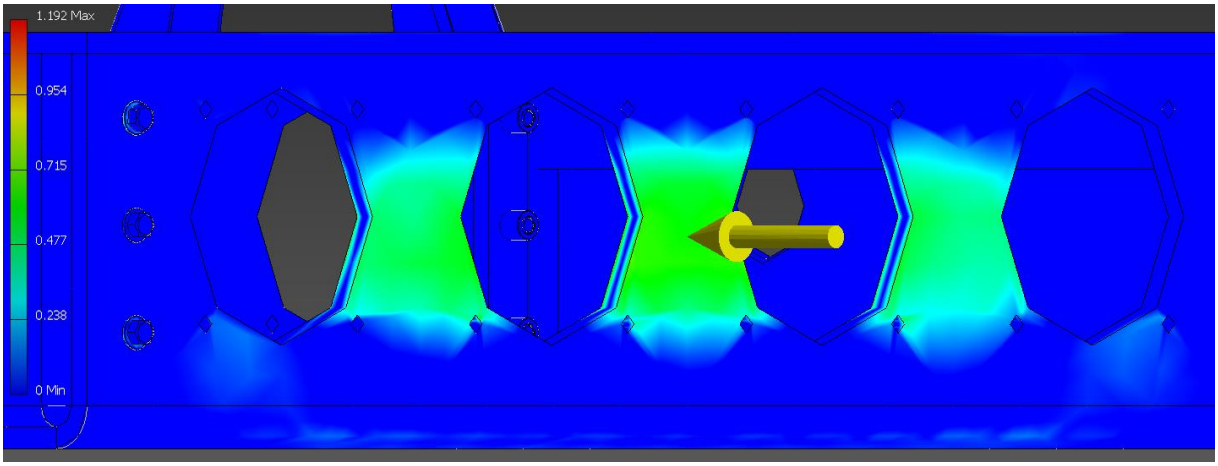

Figure 3-48. The Von Mises stresses on the enclosure due to frontal impact.

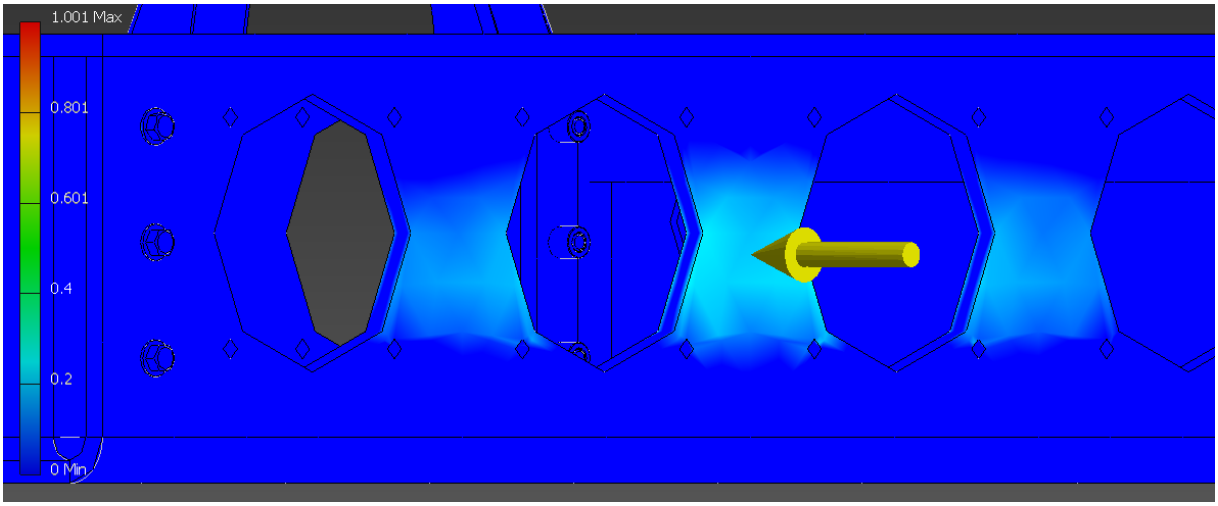

Figure 3-49. The Von Mises stresses on the enclosure due to rear impact.

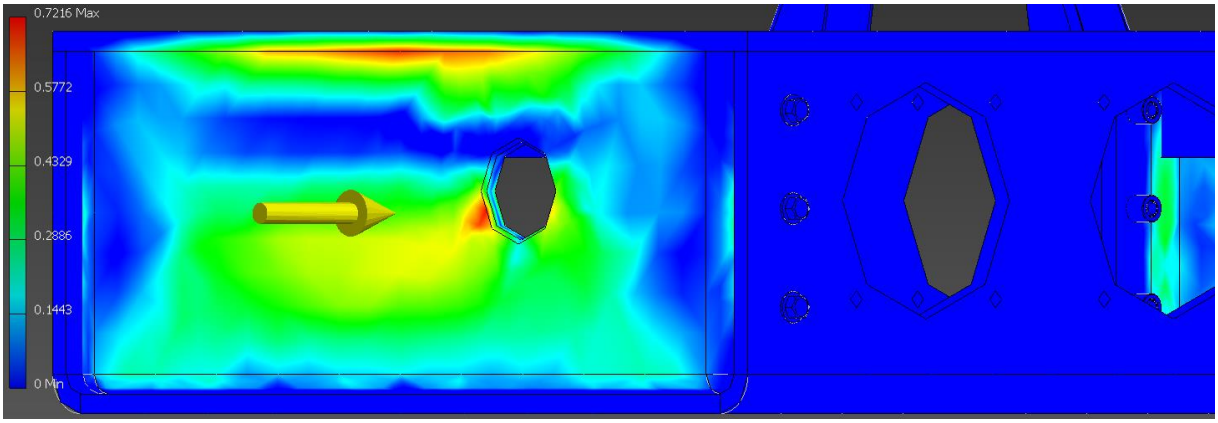

Figure 3-50. The Von Mises stresses on the enclosure due to side impact.

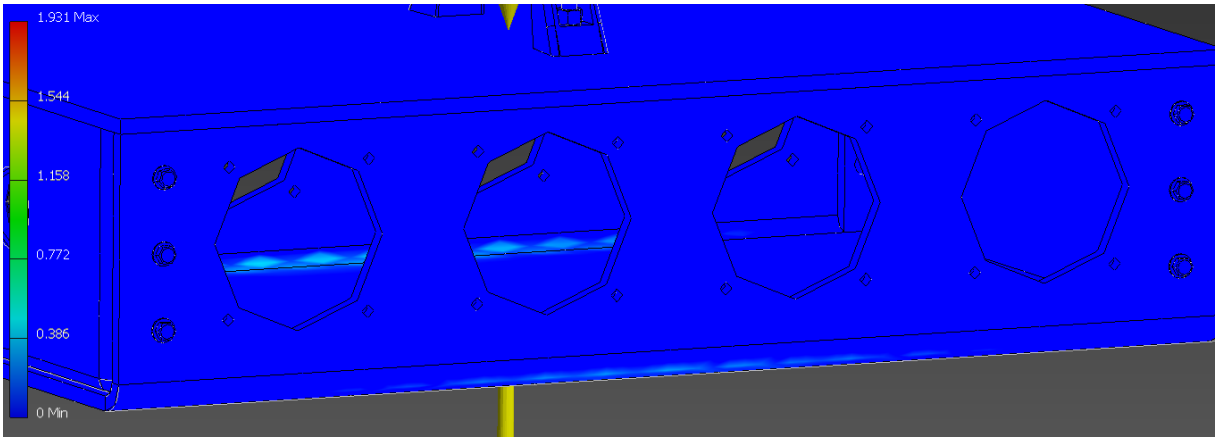

Figure 3-51. Von Mises stresses on the enclosure due to vertical impact.

4 Conclusion and Future Work

4.1 Conclusion

This thesis covers the design and thermal analysis of an ESS for FUSEV, which includes a literature review, competitor analysis, market study, component selection, battery module design, BARR design, CFD thermal analysis of the BARR, ESS enclosure design, and the FEM stress analysis of the ESS enclosure.

The battery modules were designed using Autodesk Inventor such that the capacity of the BARR is dependent on the number of 18650 cells interconnected in parallel within the battery modules; increasing the number of 18650 cells increases the BARR's capacity whereas decreasing the number of 18650 cells decreases the BARR's capacity. The BARR was designed using Inventor such that the bus voltage of the ESS is dependent on the number of battery modules interconnected in series within the BARR; increasing the number of battery modules increases the bus voltage whereas decreasing the number of battery modules decreases the bus voltage.

A CFD thermal analysis was conducted upon the BARR and ESS enclosure's internal volume using the FEM enabled by ANSYS Fluent. The configuration used within Fluent was validated through a baseline study conducted against the results of an experimentally verified CFD thermal analysis. A tailor-made methodology was developed for the thermal analysis conducted within this project that incorporates both the Fluent and Inventor environments. Using this methodology and by refining the problem though the incorporation of the imposed constraints, 16 design variations of the ESS enclosure were developed. The thermal analysis was conducted upon each of the variations whilst ensuring that the same configuration was used for each of the simulations. By tabulating the results of the analysis, it was ascertained that the enclosure design with 4 circular inlets and 4 circular outlets of 60 mm performed the best of all the design iterations. Specifically, with this design there was a decrease in cell temperature of 7.20% to 26.10%;

decrease in busbar temperature of 16.80% to 19.10%; decrease in nut and bolt temperature of 13.30% to 20.20%; and decrease in tabbing material temperature of 7.00% to 20.10% from the initial global temperature of 26.85 °C.

The ESS enclosure was designed using Inventor to incorporate the findings of the CFD thermal analysis, whilst being modular in design and easily manufacturable. The enclosure is to be constructed of aluminium-6061, due to its strength-to-weight ratio and its capacity to be folded into the desired shape. The enclosure was designed to be easily disassembled for access to the BARR in order to configure the ESS and for subcomponents of the enclosure to be easily replaced.

A FEM stress analysis was conducted upon the ESS enclosure using Inventor to ensure that it meets the design requirements and that no design failures occur under expected crash accelerations. It was determined that the displacement caused by the imposed loads upon the enclosure was not significant enough to puncture the 18650 cells. Additionally, it was determined that the Von Mises caused upon the enclosure was significantly lower than the yield strength of aluminium; consequently, no design failures occurred.

Through the progress made during the course of the project a further depth of knowledge regarding the ESS that was previously unknown by the team was gained and documented. Furthermore, by selecting programmable COTS products and developing modular designs that are flexible, ESS of any specifications that adheres to the rules and regulations of the WSC and ADRs can be built through an application of the fundamental concepts described within this thesis, whereby futureproofing the designs developed.

4.2 Summary of Key Contributions

In achieving the primary project objectives, the key contributions of this project to field of research is the results from the thermal analysis of an original ESS design, which considers not only the 18650 cells themselves but also the effects of all highly conductive materials that composes the BARR. Besides the contribution of this project in furthering research within this field, the work that was completed and documented within this thesis will allow for project continuity in the development of the ESS.

In particular, the literature review details the research and decisions made with regard to the selection of suitable battery chemistry, battery form factor, battery interconnectivity methods and the safety and performance concerns associated with the use of batteries. In addition to this, the literature review also provides an insight into the available TMS and thermal modelling techniques that can be used for the analysis of FUSEV's ESS. The competitor analysis details the design of the ESS developed of teams that had successfully completed the previous WSC. This was done to provide an indication of what underlying assumptions were made by these teams. This information is very valuable as their designs are representative of their experience with the WSC. The market study provides information regarding the currently available commercial off the shelf BMS, BC and batteries. A comparison of the products with input from FAST enabled the selection of the most appropriate products. The design of a modularized, adaptable and interoperable ESS was developed and a simulation of the thermal and stress analysis of the ESS was conducted. This involved the design and development of a battery module, battery array and ESS enclosure. The simulations were validated through a baseline study and incorporated into the above-mentioned ESS design.

All primary objectives were all achieved. However, due to monetary concerns and time constraints the extension objectives were not completed. Nevertheless, the components necessary for the completion of the extension objectives were ordered and are currently en route.

4.3 Future Work

The work completed during the course of this project has revealed opportunities for improvement and further research. Some of these opportunities include:

- **Improvement of CFD Model Using Experimental Data:** After obtaining all of the necessary parts and equipment it is intended that the BARR modules be subjected to charge, discharge, and thermal testing using the Cellpro Powerlab 8, Orion BMS and a thermal imaging camera, to obtain quantified experimental data. This data regarding the module's real world performance is to be integrated into the CFD model developed during this project to obtain a more accurate representation of the system built.

- **Development of a Dedicated Stand-Alone Thermal Management System:** While the BMS selected has the capacity to also function as a TMS, it is recommended that a dedicated stand-alone TMS be built. It is intended that this TMS works in conjunction with the one enabled by the BMS. This is to ensure that if one of the TMSs malfunctions the other serves as backup. Whereby ensuring that the BARR is constantly monitored during its operation to inform the team of any undesirable behaviour.

- **Further Research into Bonding Fiberglass with Aluminium:** The proposed solution should be investigated further to ensure that the adhesive can bond fiberglass to the aluminium with sufficient strength. It is recommended that the suppliers of the adhesive be consulted to determine its capacity for strength and its suitability for the intended purpose [90].

- **Further Research into Mechanism for Active 2D Convection Air Cooling:** The ESS designed employs 1D cooling due to the size constraints imposed by the battery bracket within the golf cart; however, for FUSEV's ESS there exists a possibility to employ 2D cooling. This will allow for greater coverage of cells throughout the enclosure, whereby allowing the ESS to dissipate heat quickly and ensure consistency in BARR temperature [51, 55, 91].

- **Development of an Aging Model for the 18650 Cells:** An aging model of the 18650 cells have to be developed to provide a realistic representation of the cell's deterioration due to temperature, voltage and current. This model once developed can be used to predict the calendar and or cycle life of the cells; which in turn can then be used to optimise the ESS to increase the calendar and or cycle life of the cells, to increase longevity of the ESS [92, 93].

Exploring these opportunities will help further the work that was completed during the course of this project; thereby enabling FAST to gain further knowledge regarding the design, development and modelling of the ESS and its subcomponents.

5 REFERENCES

1. Schneider, S. and L. Morton, *THE PRIMORDIAL BOND Exploring Connections between Man and Nature through the Humanities and Sciences*. (1981), Plenum Press: New York. p. viii, 7, 284.

2. Connors, J., *On the Subject of Solar Vehicles and the Benefits of the Technology*. 2007 International Conference on Clean Electrical Power, (2007): p. 700-705.

3. Lin, C., et al., *Battery management system with dual-balancing mechanism for LiFePO4 battery module*. TENCON 2011 - 2011 IEEE Region 10 Conference, Bali, (2011): p. 863-867.

4. Zhong, Q., et al., *Experimental study on relationship between SOC and OCV of lithium-ion batteries*. International Journal of Smart Grid and Clean Energy, (2014). **3**(2): p. 149-153.

5. Zhongcheng, F., Z. Wei, and Z. Hui, *Distributed Battery Management System Based on CAN Field-bus*. International Conference on Mechatronic Sciences, Electric Engineering and Computer (MEC), (2013): p. 1921-1924.

6. Muhida, R., et al., *Design of Environmental Friendly Hybrid Electric Vehicle*. International Conference on Computer and Communication Engineering, (2012): p. 554-548.

7. United States Environmental Protection Agency. *Global Greenhouse Gas Emissions Data*. (2016) [2 May 2016]; Available from: https://www3.epa.gov/climatechange/ghgemissions/global.html.

8. United States Environmental Protection Agency. *Greenhouse Gas Emissions: Sources of Greenhouse Gas Emissions*. (2016) [2 May 2016]; Available from: https://www3.epa.gov/climatechange/ghgemissions/sources/transportation.html.

9. United States Environmental Protection Agency. *Climate Change*. (2016) [3 May 2016]; Available from: https://www3.epa.gov/climatechange/basics/.

10. United Nations Department of Economic and Social Affairs Population Division, *World Population Monitoring, 2001: Population, Environment and Development*. (2001), New York: United Nations Publications. p.70.

11. Zachariadis, T., Cars and Carbon: Automobiles and European Climate Policy in a Global Context. (2012), Dordrecht: Springer. pp. 1,19.

12. Goldman, J. *Comparing Electric Vehicles: Hybrid vs. BEV vs. PHEV vs. FCEV - The Equation*. (2014) 3 May 2016]; Available from: http://blog.ucsusa.org/josh-goldman/comparing-electric-vehicles-hybrid-vs-bev-vs-phev-vs-fcev-411.

13. Yüzügüllü, E., *Synergies for Sustainable Energy*. (2013), Norwood: Artech House. pp. 134-136.

14. Nikowitz, M., Advanced Hybrid and Electric Vehicles: System Optimization and Vehicle Integration. (2016), Vienna: Springer. pp. 1-5.

15. Sioshansi, F.P., *Generating Electricity in a Carbon-Constrained World*. (2009), Burlington: Academic Press. pp. xii, 271-279.

16. World Solar Challenge. *History*. (2013) [4 May 2016]; Available from: http://www.worldsolarchallenge.org/about_wsc_2015/history.

17. World Solar Challenge. *Overview*. (2014) [5 MAY 2016]; Available from: http://www.worldsolarchallenge.org/about_wsc_2015/overview.

18. World Solar Challenge. *The Philosophy behind the Development of the Classes*. (2015) [5 MAY 2016]; Available from: http://www.worldsolarchallenge.org/team_info/2015_classes/philosophy.

19. MathWorks. *Setting a World Speed Record with a Student-Designed Solar Electric Vehicle*. (2015) [5 MAY 2016]; Available from: http://au.mathworks.com/company/newsletters/articles/setting-a-world-speed-record-with-a-student-designed-solar-electric-vehicle.html.

20. Intel IQ. *Student Solar Car Team Shows the Future is Powered by Sunshine*. (2016) [5 MAY 2016]; Available from: http://iq.intel.com/wp-content/uploads/sites/18/2016/01/World-Solar-Car-Challenge-map.jpg.

21. World Solar Challenge. *Challenger Class*. (2015) [5 MAY 2016]; Available from: http://www.worldsolarchallenge.org/team_info/2015_classes/challenger_class.

22. World Solar Challenge. *Cruiser Class*. (2015) [5 MAY 2016]; Available from: http://www.worldsolarchallenge.org/team_info/2015_classes/cruiser_class.

23. World Solar Challenge. *Adventure Class*. (2015) [5 MAY 2016]; Available from: http://www.worldsolarchallenge.org/team_info/2015_classes/adventure_class.

24. World Solar Challenge, *2017 WSC Regulations*. (2016): p. 22-24, 35-37, 53-57.

25. World Solar Challenge. *Cruiser Class: Outright Results*. (2015) [5 MAY 2015]; Available from: http://www.worldsolarchallenge.org/files/1485_cruiser_class_outright_results.pdf.

26. Department of Infrastructure and Regional Development, *National Guidelines for the Installation of Electric Drives in Motor Vehicles*, Department of Infrastructure and Regional Development, Editor. (2011). p. 29.

27. Liu, R.S., Electrochemical Technologies for Energy Storage and Conversion: Vol. 1. (2012): John Wiley & Sons. p. 58.

28. Fuhs, A., Hybrid Vehicles: and the Future of Personal Transportation. (2008), CRC Press. p. 504.

29. Hanifah, R., S.F. Toha, and S. Ahmad, *Electric Vehicle Battery Modelling and Performance Comparison in Relation to Range Anxiety*. Procedia Computer Science, (2015). **76**: p. 250-256.

30. Linden, D. and T.B. Reddy, *Handbook of Batteries*. (2002): McGraw-Hill. pp. 1.13, 22.4- 22.8, 26.1 - 26.12, 34.1-34.24, 37.14-37.15, 37.3.

31. Gogus, Y., *Energy Storage Systems - Volume II*. (2009): EOLSS Publishers. pp. 11, 50, 60, 108.

32. Jiang, J., S.P. Jiang, and C. Zhang, Fundamentals and Application of Lithium-ion Batteries in Electric Drive Vehicles. (2015): John Wiley & Sons. p. 285.

33. Yiu, K., *Battery Technologies for Electric Vehicles and Other Green Industrial Projects*. Power Electronics Systems and Applications (PESA), (2011)(4th International Conference on Power Electronics Systems and Applications): p. 1-2.

34. Berg, H., *Batteries for Electric Vehicles*. (2015): Cambridge University Press. pp. 58-59, 83, 102-107, 130.

35. Nitta, N., et al., *Li-ion battery materials: present and future*. Materials Today, (2015). **18**(5): p. 256-264.

36. Chen, A. *Sulfur-graphene oxide material for lithium-sulfur battery cathodes*. (2013) [cited 2016 [5 JUNE 2016]; Available from: http://eetd.lbl.gov/news/article/56320/sulfur-graphene-oxide-material-for-lithium-sulfur-battery-cathodes.

37. Battery University. *Comparison Table of Secondary Batteries*. (2016) [cited 2016 [13 MAY 2016]; Available from: http://batteryuniversity.com/learn/article/secondary_batteries.

38. Battery University. *Types of Lithium-ion*. (2016) [cited 2016 [12 MAY 2016]; Available from: http://batteryuniversity.com/learn/article/types_of_lithium_ion.

39. Battery University. *Future Batteries*. (2016) [cited 2016 [13 MAY 2016]; Available from: http://batteryuniversity.com/learn/article/experimental_rechargeable_batteries.

40. Battery University. *Types of Battery Cells*. (2016) [cited 2016 [15 MAY 2016]; Available from: http://batteryuniversity.com/learn/article/types_of_battery_cells.

41. VanZwol, J. *Use Li-Ion Batteries In Your Next Mobile Computer*. (2011) [cited 2016 19 JULY 2016]; Available from: http://electronicdesign.com/power/use-li-ion-batteries-your-next-mobile-computer.

42. Weicker, P., A Systems Approach to Lithium-Ion Battery Management. (2013): Artech House. 316.

43. Tourism Australia. *Darwin Weather, Temperature and Climate*. (2016) [cited 2016 19 MAY 2016]]; Available from: http://www.australia.com/en/facts/weather/darwin-weather.html.

44. Tourism Australia. *Adelaide Weather, Temperature and Climate*. (2016) [cited 2016 19 MAY 2016]]; Available from: http://www.australia.com/en/facts/weather/adelaide-weather.html.

45. Santhanagopalan, S., et al., *Design and Analysis of Large Lithium-Ion Battery Systems*. (2014): Artech House Publishers. pp. 68-79.

46. Pesaran, A., S. Burch, and M. Keyser, An Approach for Designing Thermal Management Systems for Electric and Hybrid Vehicle Battery Packs in Fourth Vehicle Thermal Management Systems Conference and Exhibition (1999), National Renewable Energy Laboratory London, UK. p. 1-16.

47. Tong, X.C., *Advanced Materials for Thermal Management of Electronic Packaging*. Vol. 30. (2011): Springer Science & Business Media. 373-384.

48. Saw, L.H., et al., Computational fluid dynamic and thermal analysis of Lithium-ion battery pack with air cooling. Applied Energy, (2016). **177**: p. pp. 783-792.

49. Cicconi, P., M. Germani, and D. Landi, *Modelling and thermal simulation of a PHEV battery module with cylindrical LFP cells.* EVS27 International Battery, Hybrid and Fuel Cell Electric Vehicle Symposium, (2013). **November**(17-20): p. 1-11.

50. IMechE, Vehicle thermal Management Systems Conference and Exhibition (VTMS10). (2011), Cambridge, UK: Elsevier Science. pp. 293-296.

51. Shabani, B. and M. Biju, *Theoretical Modelling Methods for Thermal Management of Batteries.* Energies, (2015). **8**(9): p. 10153-10177.

52. Bergman, T.L., et al., *Fundamentals of Heat and Mass Transfer*. (2011): John Wiley & Sons. p. 284.

53. Fathi, M., Integrated Systems: Innovations and Applications. (2015): Springer. 257.

54. Rao, S.S., *The Finite Element Method in Engineering*. 4 ed. (2011): Butterworth-Heinemann. pp. 3, 10.

55. Moukalled, F., L. Mangani, and M. Darwish, The Finite Volume Method in Computational Fluid Dynamics: An Advanced Introduction with OpenFOAM® and Matlab. (2015): Springer. p. 791

56. Huria, T., et al., High fidelity electrical model with thermal dependence for characterization and simulation of high power lithium battery cells. Electric Vehicle Conference (IEVC), 2012 IEEE International, (2012): p. 1-8.

57. Groenen, B., *World Solar Challenge Vehicle Specifications Request*, A. Mankavil, Editor. (2016), Eindhoven.

58. Carr, I., *World Solar Challenge Vehicle Specifications Request*, A. Mankavil, Editor. (2016), Sunswift.

59. Lange, N., *World Solar Challenge Vehicle Specifications Request*, A. Mankavil, Editor. (2016), Hochschule Bochum.

60. LG Chem Product Specification Rechargeable Lithium Ion Battery Model : INR18650 MH1 3200mAh (2014). pp. 4-5.

61. LG Chem Product Specification Rechargeable Lithium Ion Battery Model : INR18650HG2 3000mAh. (2014). pp. 4-5.

62. LG Chem Product Specification Rechargeable Lithium Ion Battery Model : ICR18650E1 12.0Wh. (2012). pp. 4-5.

63. Panasonic *Lithium Ion NCR18650B*. (2012). p. 1.

64. Panasonic *Spec Sheet for NCR18650BF*. n.d., pp. 1-2.

65. Panasonic *Specifications for NCR18650GA*. n.d., pp. 1-2.

66. Panasonic *Specifications of NCR18650BD*. (2013). pp. 6-7.

67. Panasonic *Lithium Ion NCR18650A*. (2012). pp. 2-3.

68. Panasonic Specifications of Lithium Ion NCR18650BE. n.d., pp. 6-7.

69. Samsung Specification of Product for Lithium-Ion Rechargeable Cell Model : ICR18650-30B. (2010). pp.2-3.

70. Samsung Specification of Product for Lithium-ion Rechargeable Cell Model : ICR18650-30A (2007). pp. 2-3.

71. Tritium. *IQ Battery Management System*. (2016) [cited 2016 8 AUG]; Available from: http://tritium.com.au/products/iq-battery-management-system/.

72. Ewert Energy Systems. *Orion BMS – Standard Size*. (2015) [cited 2016 8 AUG]; Available from: http://www.orionbms.com/products/orion-bms-standard/.

73. Elithion. *Lithiumate Pro*. (2016) [cited 2016 9 AUG]; Available from: http://elithion.com/lithiumate_pro.php.

74. Manzanita Micro. *Owners Manual - Rudman Regulator Mark 3x12 Digital Lithium Ion BMS* (2013) [cited 2016 10 AUG]; Available from: http://www.manzanitamicro.com/downloads/category/2-bms1?download=88%3Amk3x12ld.

75. Ventec. *Ventec iBMS 8-18S packs in series*. (2016) [cited 2016 9 AUG]; Available from: http://ventec-ibms.com/en/embedded-bms-solutions/ventec-ibms-8-18s-packs-in-series/.

76. ThunderStruck Motors. *TSM2500 Series High Efficiency Intelligent Charger*. (2014) [cited 2016 17 AUG]; Available from: http://www.thunderstruck-ev.com/images/ThunderStruck%20TS2.5C%20ManualV1.06.pdf.

77. Manzanita Micro. *PFC20-X*. (2012) [cited 2016 18 AUG]; Available from: http://www.manzanitamicro.com/downloads/category/15-chargers?download=69%3Apfc20-30-40-spec-sheet.

78. Zivan. *Battery charger NG5-7-9*. (2003) [cited 2016 17 AUG]; Available from: http://www.zivanusa.com/pdf/NG5-7-9.pdf.

79. Eltek Valere. *EV Power Charger 3 kW Traction Battery Charger Module*. n.d. [cited 2016 18 AUG]; Available from: http://www.eltek.com/photoalbum/view2/P3NpemU9b3JnJmlkPTQ4NDY5MQ.

80. Elcon Charger. *PFC 2500 Battery Charger*. n.d. [cited 2016 17 AUG]; Available from: http://evolveelectrics.com/PDF/Elcon/PFC2500%20Manual.pdf.

81. Trojan Battery Company *T-875 with Bayonet*. (2016). p. 2.

82. Dyer, C.K., et al., *Encyclopedia of Electrochemical Power Sources*. (2013): Elsevier Science. pp.499-502.

83. Mills, A. and S. Al-Hallaj, *Simulation of passive thermal management system for lithium-ion battery packs*. Journal of Power Sources, 2005. **141**(2): p. 307-315.

84. AZO Materials. *Stainless Steel - Grade 304 (UNS S30400)*. (2016) [cited 2016 02 AUG]; Available from: http://www.azom.com/properties.aspx?ArticleID=965.

85. MATBASE. *Brass*. (2016) [cited 2016 03 SEP]; Available from: https://www.matbase.com/material-categories/metals/non-ferrous-metals/wrought-copper/material-properties-of-cuzn30-brass.html#properties.

86. MATBASE. *PBT*. (2016) [cited 2016 03 SEP]; Available from: https://www.matbase.com/material-categories/natural-and-synthetic-polymers/engineering-polymers/material-properties-of-polybutylene-terephthalate-pbt.html#properties.

87. MATBASE. *ABS Heat Resistant*. (2016) [cited 2016 02 SEP]; Available from: https://www.matbase.com/material-categories/natural-and-synthetic-polymers/commodity-polymers/material-properties-of-acrylonitrile-butadiene-styrene-heat-resistant-abs-heat-resistant.html#description.

88. AZO Materials. *E-Glass Fibre*. (2016) [cited 2016 02 SEP]; Available from: http://www.azom.com/properties.aspx?ArticleID=764.

89. EAL. *Cyberbond 2243 Instant Adhesive, Flexible / High Temperature*. (2016) [cited 2016 28 OCT]; Available from: http://www.eal.com.au/products/cyberbond-2243-instant-adhesive-flexible-high-temperature/.

90. Pethrick, R.A., Composite to metal bonding in aerospace and other applications., in Welding and Joining of Aerospace Materials. (2012), Woodhead Publishing. p. 288-319.

91. Yu, K., et al., Thermal analysis and two-directional air flow thermal management for lithium-ion battery pack. Journal of Power Sources, (2014). **270**: p. 193-200.

92. Ecker, M., et al., Calendar and cycle life study of Li(NiMnCo)O2-based 18650 lithium-ion batteries. Journal of Power Sources, (2014). **248**: p. 839-851.

93. Schmalstieg, J., et al., *A holistic aging model for Li(NiMnCo)O2 based 18650 lithium-ion batteries.* Journal of Power Sources, (2014). **257**: p. 325-334.

6 APPENDICES

APPENDIX A - BATTERY ARRAY PARTS LIST

Table 6-1. The parts list for manufacturing FUSEV's BARR.

Manufacturer	Model	Part Number	Description	Supplier	Contact Number	Unit Cost ($ AUD)	No. of Units	Total Cost ($ AUD)
Panasonic	NCR18650BF	88002-630BF	3.6V Nominal, 18650 Battery	Masters-Instruments (VIC)	(03) 9872 6422	10.54	126	1328.04
OEM	SPACER-2x18650	20008-303	Expandable Plastic Spacer-2x18650 Cell Module	Masters-Instruments (VIC)	(03) 9872 6422	0.72	63	45.36
OEM	25' Spooled Nickel Strip	SN125N54	0.125"W x 0.005"T x 25'L Spooled Nickel Strip	Sunstone Engineering Corporation	(02) 9999 2949	21.23	1	21.23
OEM	M6x25 Brass Hex Bolt	DMHM025R	Brass Bolt	Boltmasters	-	3.6171	30	108.513
OEM	M6 Brass Hex Full Nut	DNHMR	Brass Nut	Boltmasters	-	3.4164	30	102.492

Total Cost: $ 1605.64 AUD

Table 6-2. The parts list for preassembled battery modules for the BARR.

Manufacturer	Model	Part Number	Description	Supplier	Contact Number	Unit Cost ($ AUD)	No. of Units	Total Cost ($ AUD)
Masters-Instruments (VIC)	-	-	9/NCR18650BF 1S36P	Masters-Instruments (VIC)	(03) 9872 6422	81	14	1134.00
Masters-Instruments (VIC)	-	-	36/NCR18650BF 1S36P	Masters-Instruments (VIC)	(03) 9872 6422	321.60	1	321.60

Total Cost: $ 1455.60 AUD

APPENDIX B - BATTERY MANAGEMENT SYSTEM PARTS LIST

Table 6-3. The parts list for the Orion BMS and associated components.

Manufacturer	Model	Part Number	Description	Supplier	Contact Number	Unit Cost ($ AUD)	No. of Units	Total Cost ($ AUD)
Ewert Energy Systems	ORION BMS 48 Cell	ORION48	Orion BMS 48 Cell Unit	Ewert Energy Systems	(630) 868-3173	1128.37	1	1128.37
Ewert Energy Systems	Pre-Wired Harnesses	CWH486	BMS Wiring Harness, 48 Cell, 6ft Wire. Includes HV Pack Voltage Wiring Harness.	Ewert Energy Systems	(630) 868-3173	65.05	1	65.05
Ewert Energy Systems	Pre-Wired Harnesses	CWHMIO2	Main Connector Wiring Harness 6ft (CAN1 Wires - 12ft CAN2 Wires - 4ft)	Ewert Energy Systems	(630) 868-3173	32.52	1	32.52
Ewert Energy Systems	-	CS24500	500A Dual Range Current Sensor	Ewert Energy Systems	(630) 868-3173	86.29	1	86.29

Manufacturer	Model	Part Number	Description	Supplier	Contact Number	Unit Cost ($ AUD)	No. of Units	Total Cost ($ AUD)
Ewert Energy Systems	-	CWHCURTH	4 Thermistors Pre-Wired into Current Sensor Connector	Ewert Energy Systems	(630) 868-3173	32.52	1	32.52
Ewert Energy Systems	CANdapter CAN-To-USB Converter	CANDAPTER	CANdapter CAN to USB converter	Ewert Energy Systems	(630) 868-3173	79.65	2	159.3

Total Cost: $ 1504.05 AUD

APPENDIX C - BATTERY CHARGER PARTS LIST

Table 6-4. The parts list for the Eltek Valere BC and associated components.

Manufacturer	Model	Part Number	Description	Supplier	Contact Number	Unit Cost ($ AUD)	No. of Units	Total Cost ($ AUD)
Eltek Valere	220/3000 HE EV Power Charger - IP67 G2	67.111.0	EV Power Chargers 3kW HE	EVolve Electrics	(720) 837-7866	1618.24	1	1618.24
Eltek Valere	Charger - w/ Chill Plate	-	Chill Plate	EVolve Electrics	(720) 837-7866	410.44	1	410.44

Total Cost: $ 2028.68 AUD

APPENDIX D - ESS ENCLOSURE PARTS LIST

Table 6-5. The parts list for the ESS enclosure, inclusive of all fixtures.

Manufacturer	Model	Part Number	Description	Supplier	Contact Number	Unit Cost ($ AUD)	No. of Units	Total Cost ($ AUD)
Romak	Bolts & Nuts Metal Thread M4x35mm	0914550	M4 x 35mm Zinc Plated Metal Thread Screw (Phillips Round Head)	Bunnings	(08) 8152 6500	0.33	16	5.28
Romak	Bolts & Nuts Metal Thread M4x15mm	091350	M4 x 15mm Zinc Plated Metal Thread Screw (Phillips Round Head)	Bunnings	(08) 8152 6500	0.18	28	5.04
Romak	Bolts & Nuts Metal Thread M5x15mm	092250	M5 x 25mm Zinc Plated Hex Head Set Screw	Bunnings	(08) 8152 6500	0.41	2	0.82
Romak	Bolts & Nuts Nut Hexagon M4	097150	M4 Zinc Plated Nylon Lock Nut	Bunnings	(08) 8152 6500	0.41	44	18.04
Romak	Bolts & Nuts Nut Hexagon M5	096350	M5 Zinc Plated Hexagon Nut	Bunnings	(08) 8152 6500	0.16	2	0.32

Manufacturer	Model	Part Number	Description	Supplier	Contact Number	Unit Cost ($ AUD)	No. of Units	Total Cost ($ AUD)
Champion	MAS_900043194	BS0480	M5 Rivet Nut Insert	Masters	1300 337 707	1.40	12	16.80
Champion	MAS_900042996	BS0920	29/32X1-1/4 Rubber Wiring Grommets	Masters	1300 337 707	1.40	2	2.80
Sunon	EB60251S2-0000-999	F1045	60mm 12VDC Sleeve Bearing Fan	Altronics	1300 797 007	9.90	4	39.60
Sunon	06D1D2D3	F1044	60mm Plastic Fan Guard with Filter	Altronics	1300 797 007	3.95	4	15.80
Sunon	B-9	F1042	60mm Metal Fan Guard	Altronics	1300 797 007	2.70	4	10.80
Prestige	16mm Black Plastic Round D Handle	1044253	16mm Black Plastic Round D Handle	Bunnings	(08) 8152 6500	1.56	1	1.56

Total Cost: $ 124.31 AUD (total cost does not include cost of enclosure material or milling)

APPENDIX E - MECHANICAL DRAWINGS OF THE FUSEV'S 1S9P BATTERY MODULE

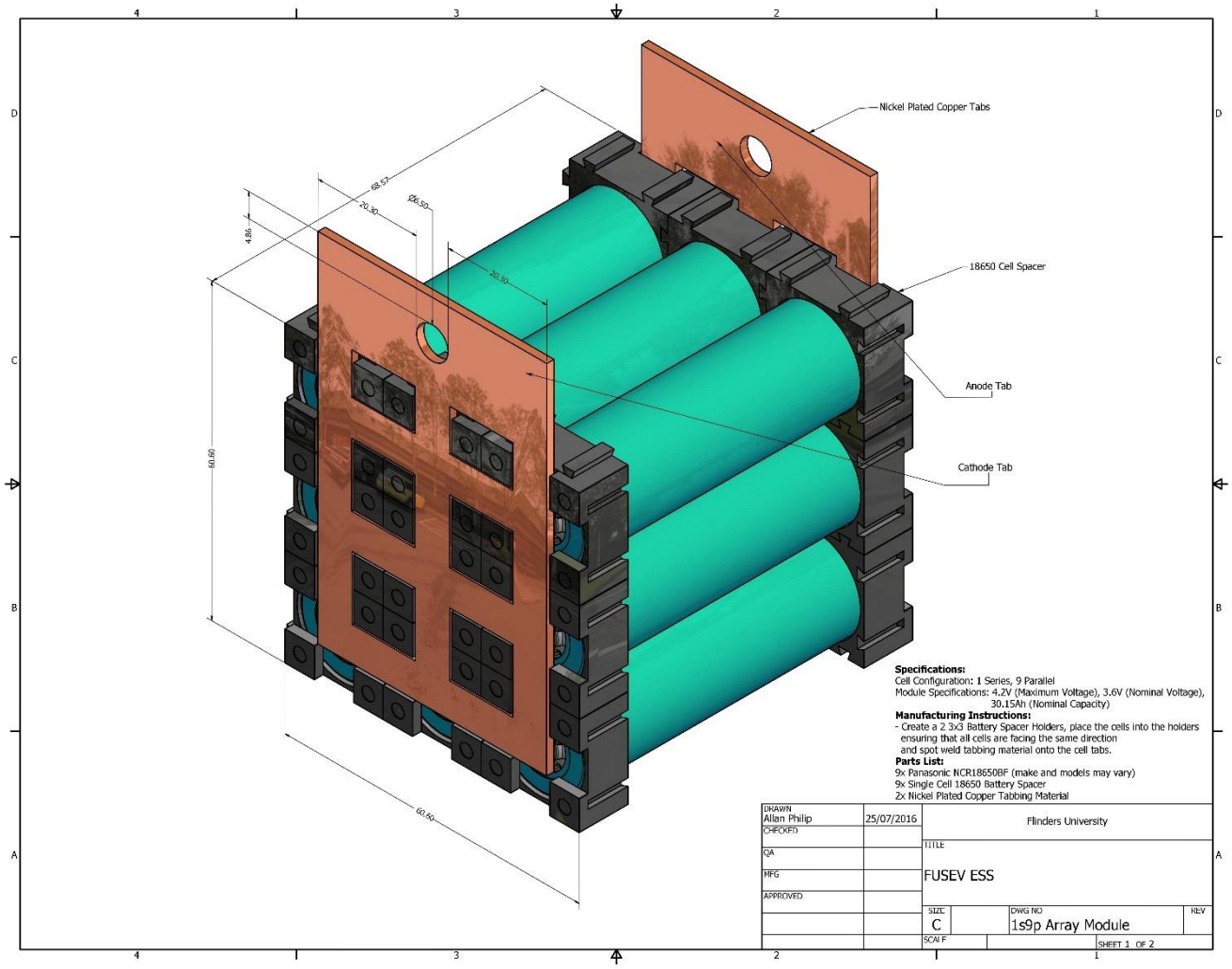

Figure 6-1. The mechanical drawing of the FUSEV's 1s9p battery module.

APPENDIX F - MECHANICAL DRAWINGS OF THE 1S9P MODULE'S TABBING MATERIAL

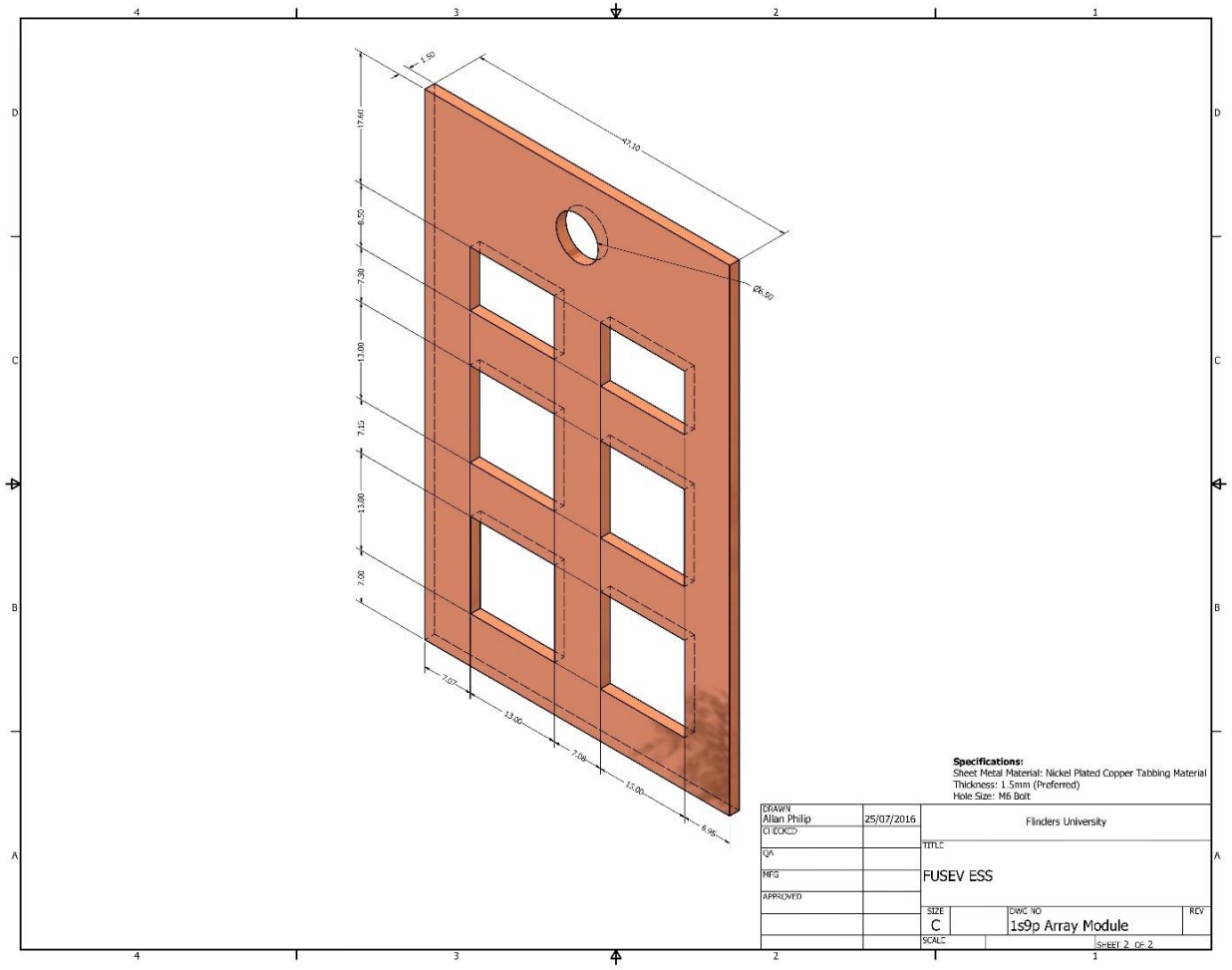

Figure 6-2. The mechanical drawing of the 1s9p module's tabbing material.

APPENDIX G - MECHANICAL DRAWINGS OF THE FUSEV'S 14S9P BATTERY ARRAY

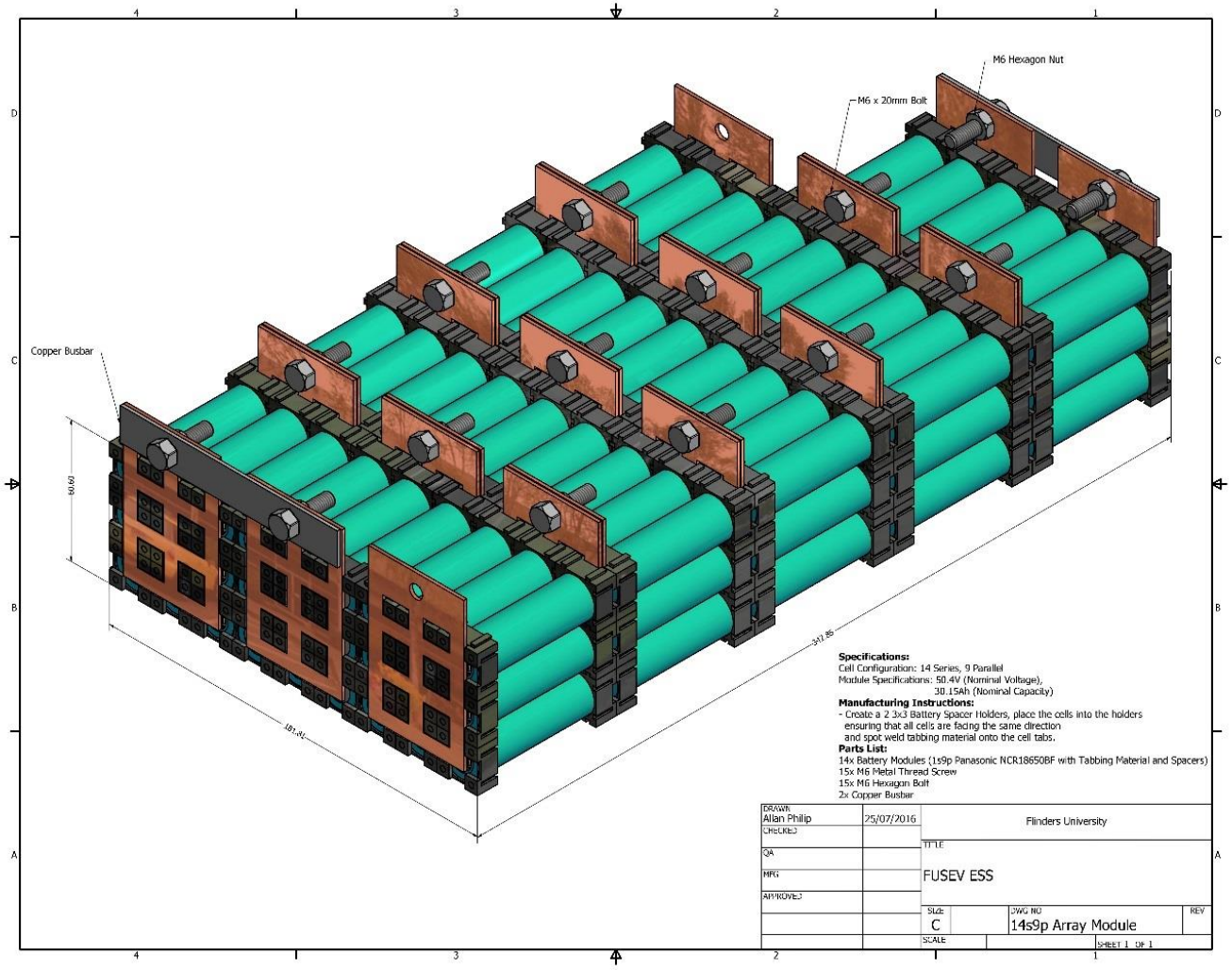

Figure 6-3 The mechanical drawing of the FUSEV's 14s9p BARR.

APPENDIX H - RESULTS OF THE THERMAL ANALYSIS CONDUCTED USING ANSYS

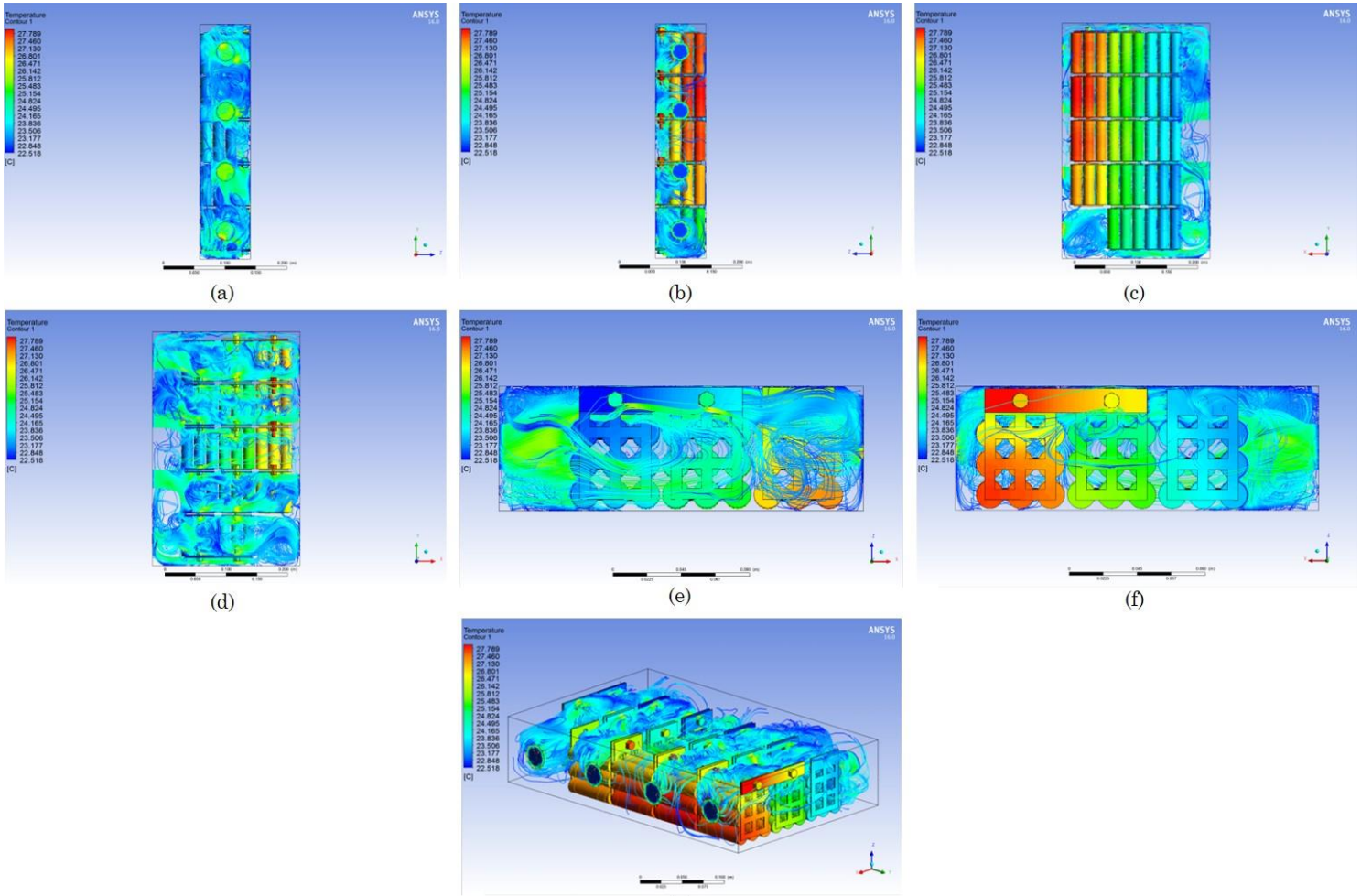

Figure 6-4. Thermal analysis of the 1st ESS enclosure design iteration with an inlet of 30 mm and outlet of 30 mm. (a) Inlet-view, (b) outlet-view, (c) base-view, (d) top-view, (e) rear-view, (f) front-view and (g) isometric-view of the ESS enclosure.

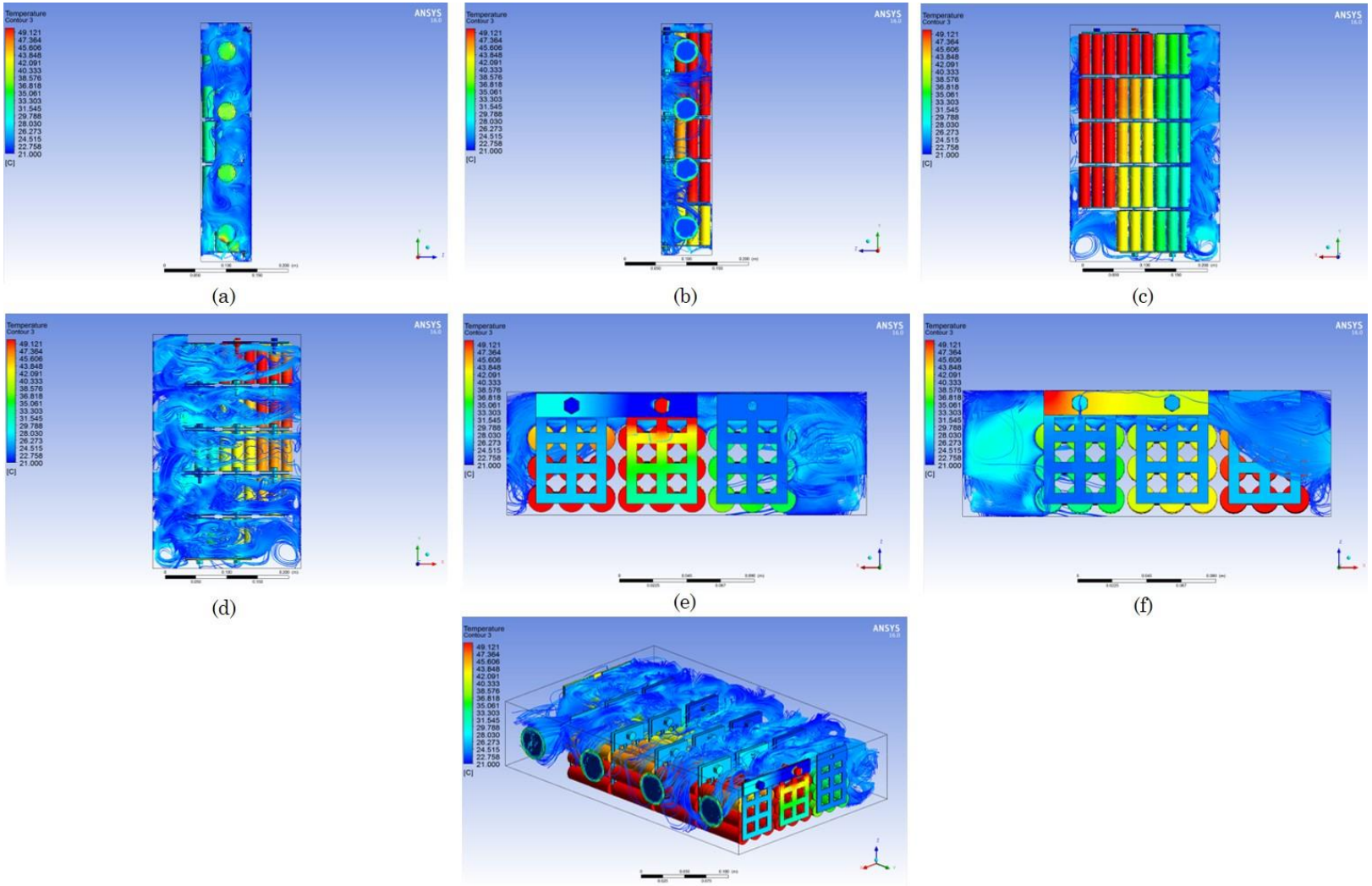

Figure 6-5. Thermal analysis of the 2nd ESS enclosure design iteration with an inlet of 30 mm and outlet of 40 mm. (a) Inlet-view, (b) outlet-view, (c) base-view, (d) top-view, (e) rear-view, (f) front-view and (g) isometric-view of the ESS enclosure.

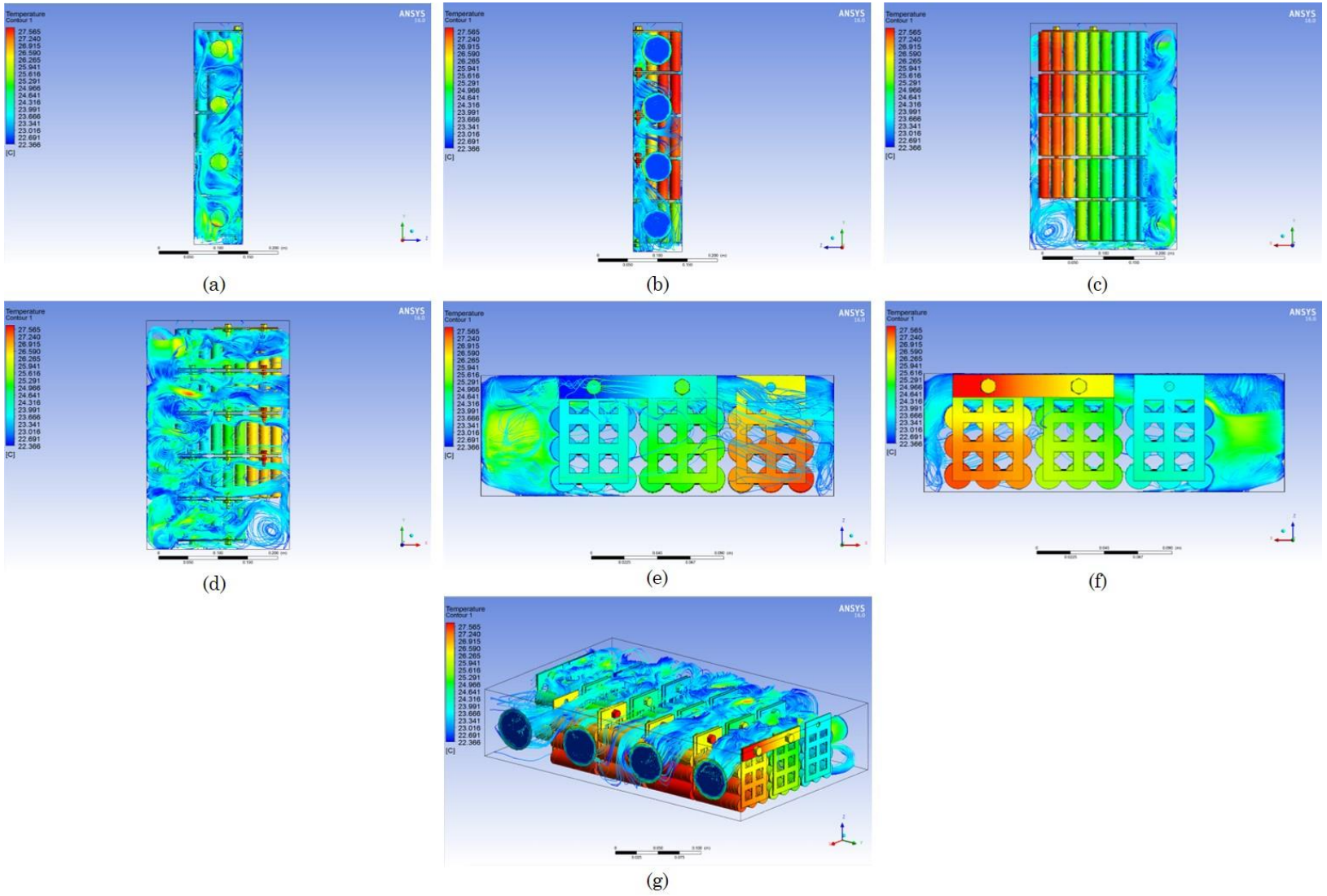

Figure 6-6. Thermal analysis of the 3rd ESS enclosure design iteration with an inlet of 30 mm and outlet of 50 mm. (a) Inlet-view, (b) outlet-view, (c) base-view, (d) top-view, (e) rear-view, (f) front-view and (g) isometric-view of the ESS enclosure.

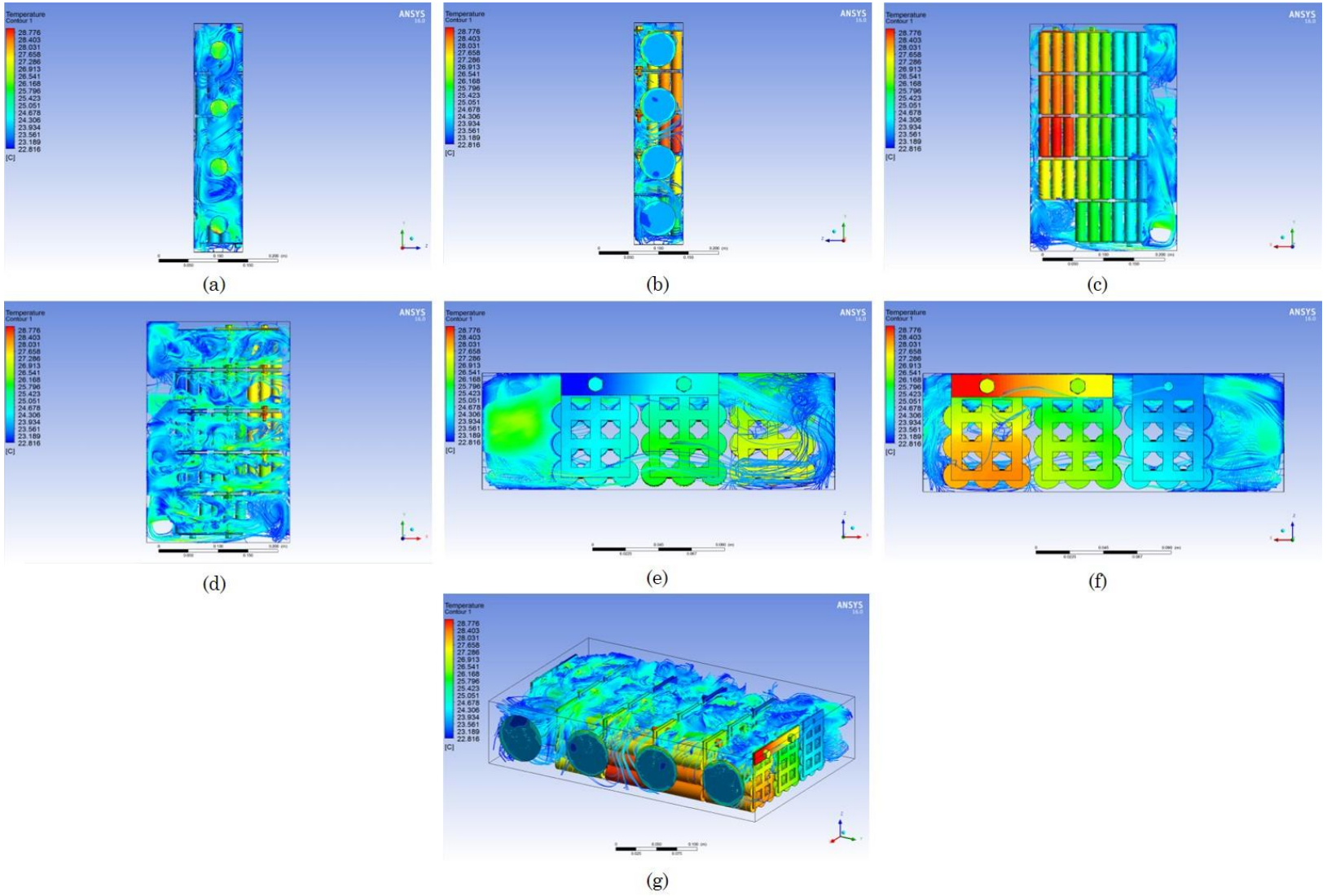

Figure 6-7. Thermal analysis of the 4th ESS enclosure design iteration with an inlet of 30 mm and outlet of 60 mm. (a) Inlet-view, (b) outlet-view, (c) base-view, (d) top-view, (e) rear-view, (f) front-view and (g) isometric-view of the ESS enclosure.

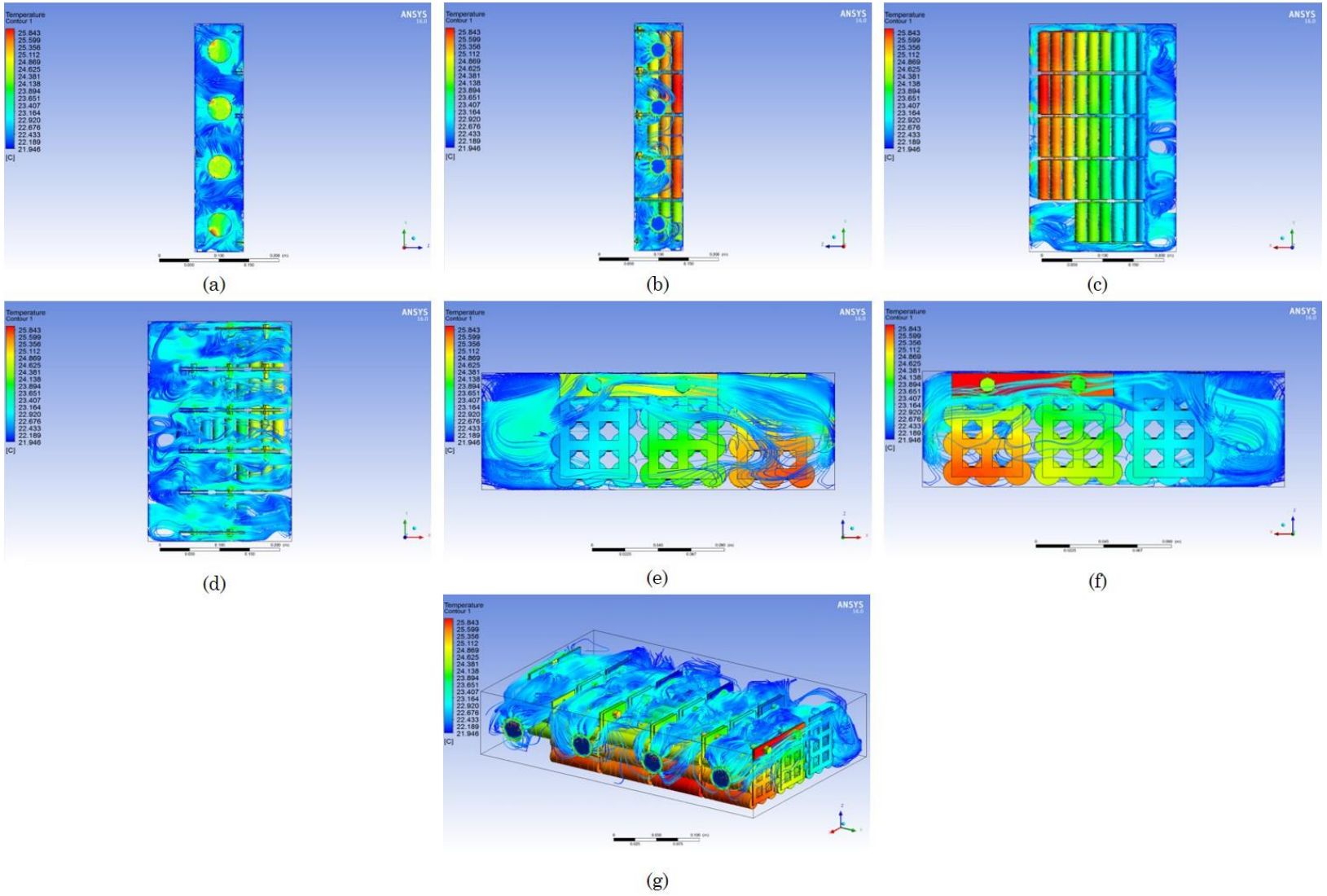

Figure 6-8. Thermal analysis of the 5th ESS enclosure design iteration with an inlet of 40 mm and outlet of 30 mm. (a) Inlet-view, (b) outlet-view, (c) base-view, (d) top-view, (e) rear-view, (f) front-view and (g) isometric-view of the ESS enclosure.

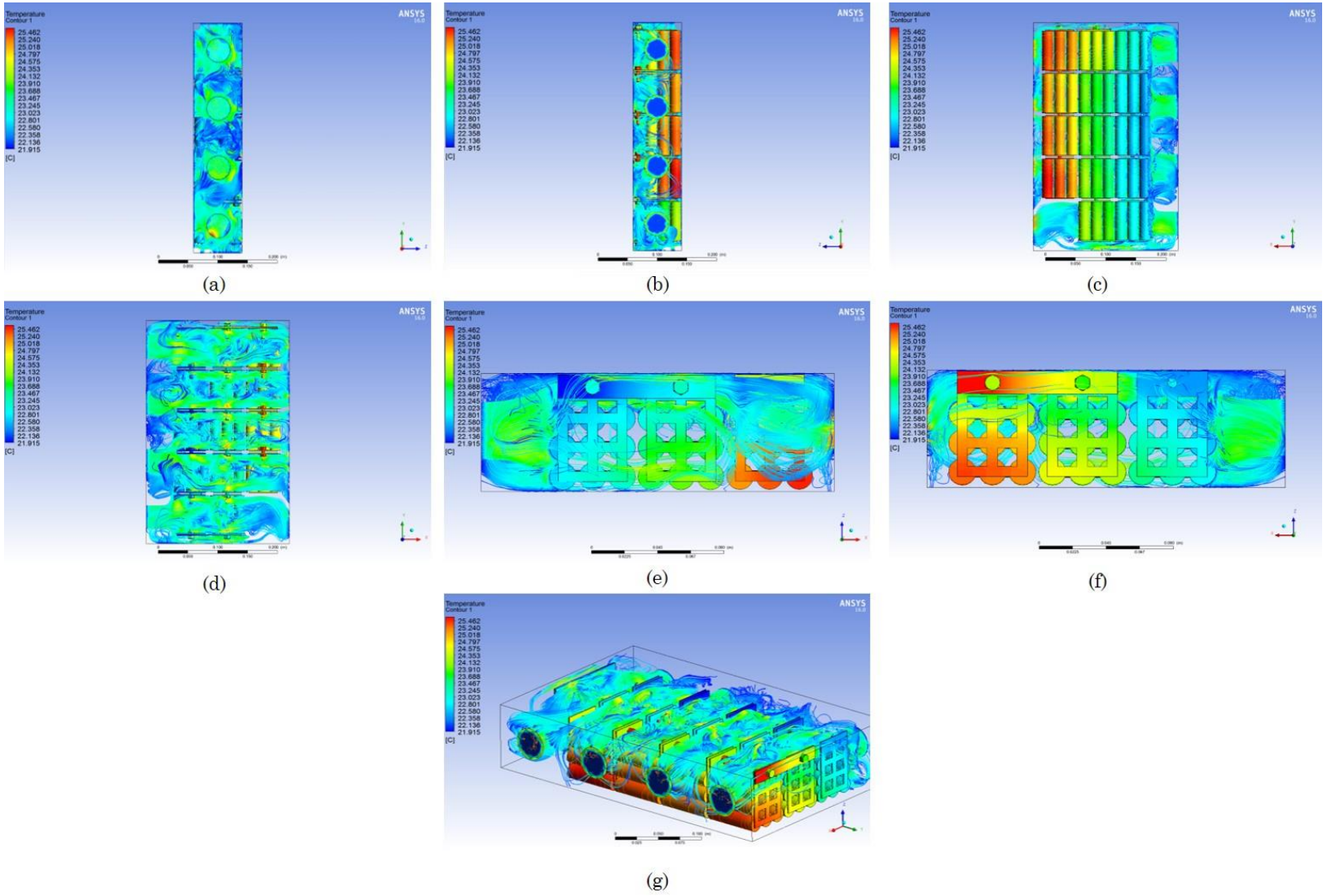

Figure 6-9. Thermal analysis of the 6th ESS enclosure design iteration with an inlet of 40 mm and outlet of 40 mm. (a) Inlet-view, (b) outlet-view, (c) base-view, (d) top-view, (e) rear-view, (f) front-view and (g) isometric-view of the ESS enclosure.

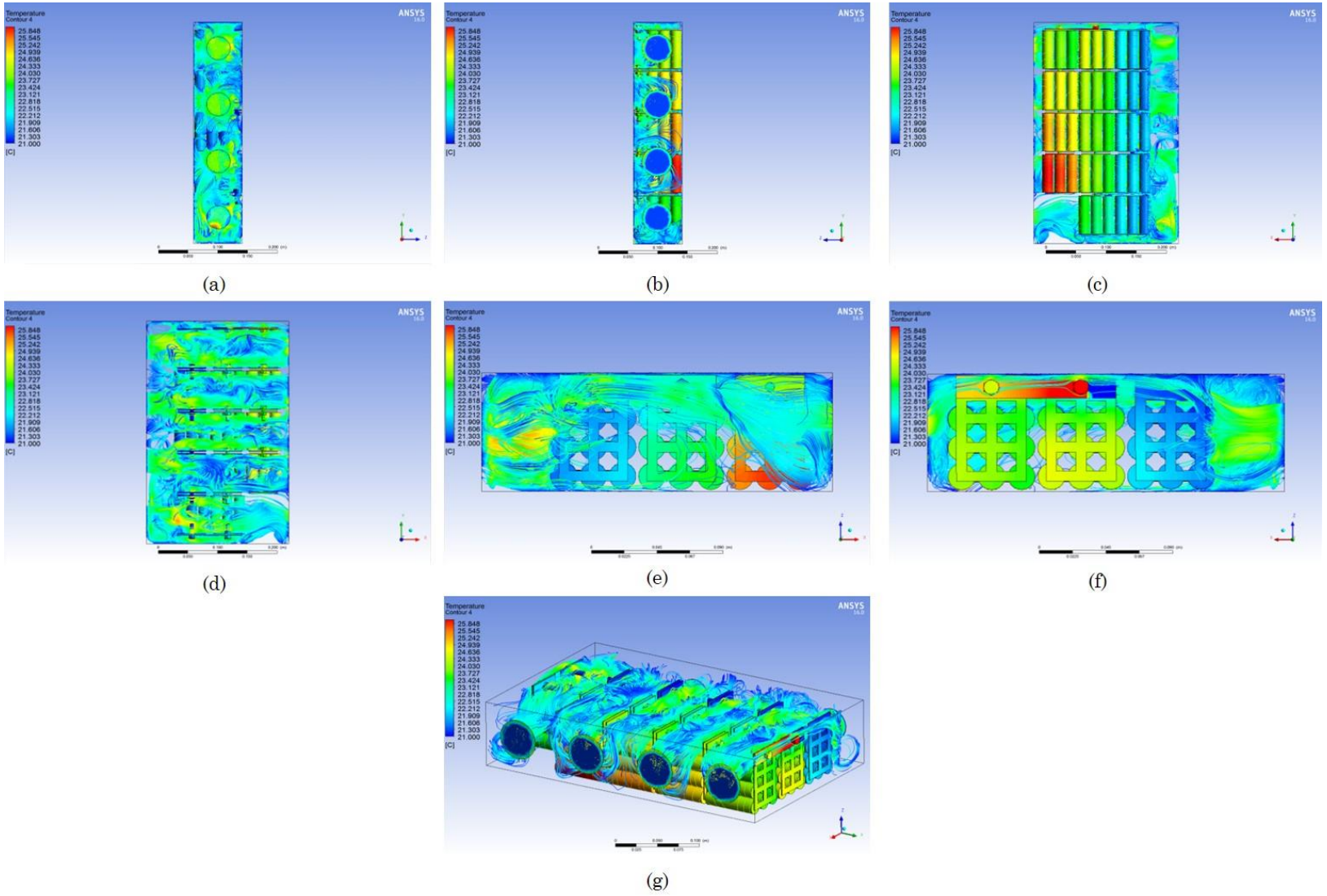

Figure 6-10. Thermal analysis of the 7th ESS enclosure design iteration with an inlet of 40 mm and outlet of 50 mm. (a) Inlet-view, (b) outlet-view, (c) base-view, (d) top-view, (e) rear-view, (f) front-view and (g) isometric-view of the ESS enclosure.

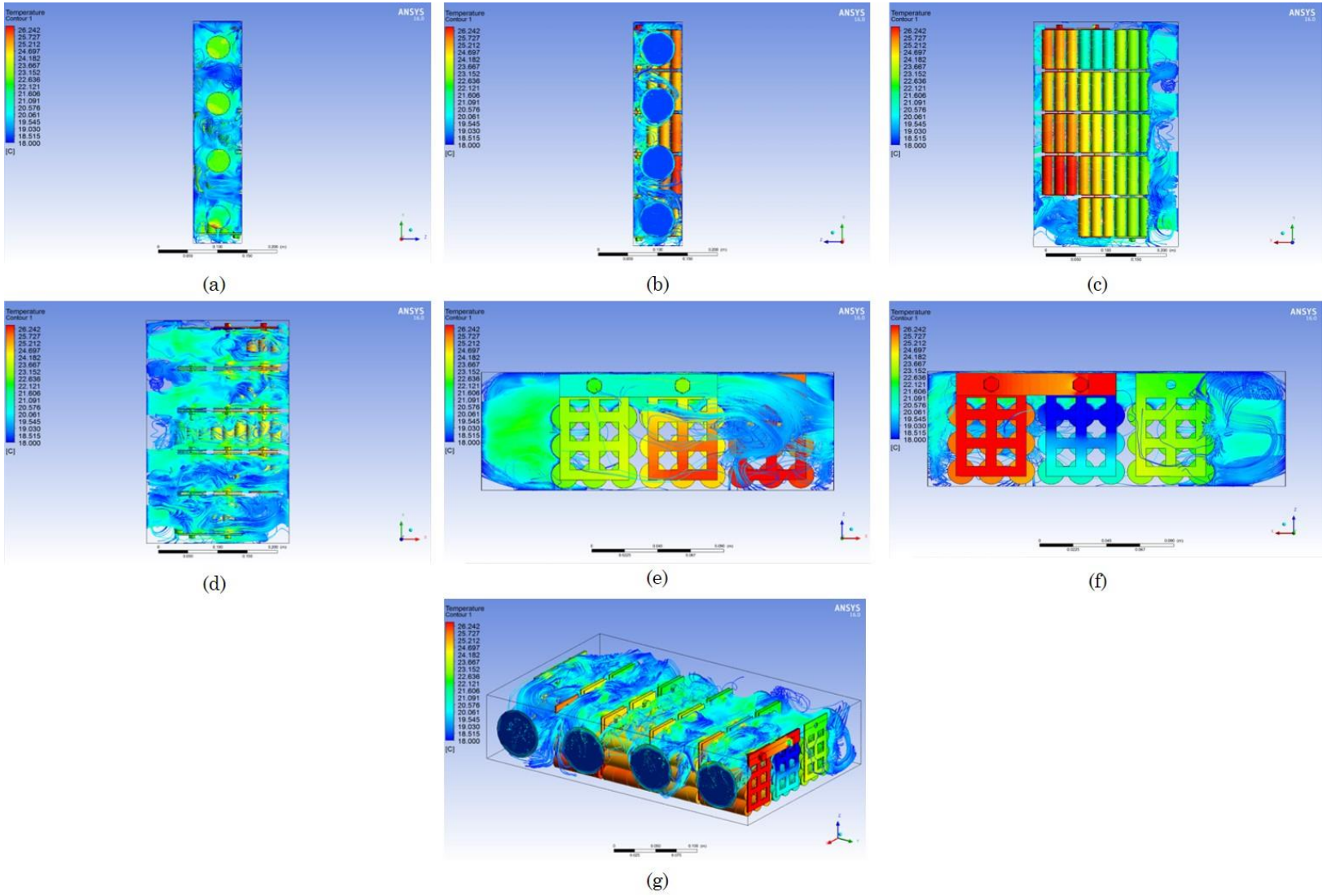

Figure 6-11. Thermal analysis of the 8th ESS enclosure design iteration with an inlet of 40 mm and outlet of 60 mm. (a) Inlet-view, (b) outlet-view, (c) base-view, (d) top-view, (e) rear-view, (f) front-view and (g) isometric-view of the ESS enclosure.

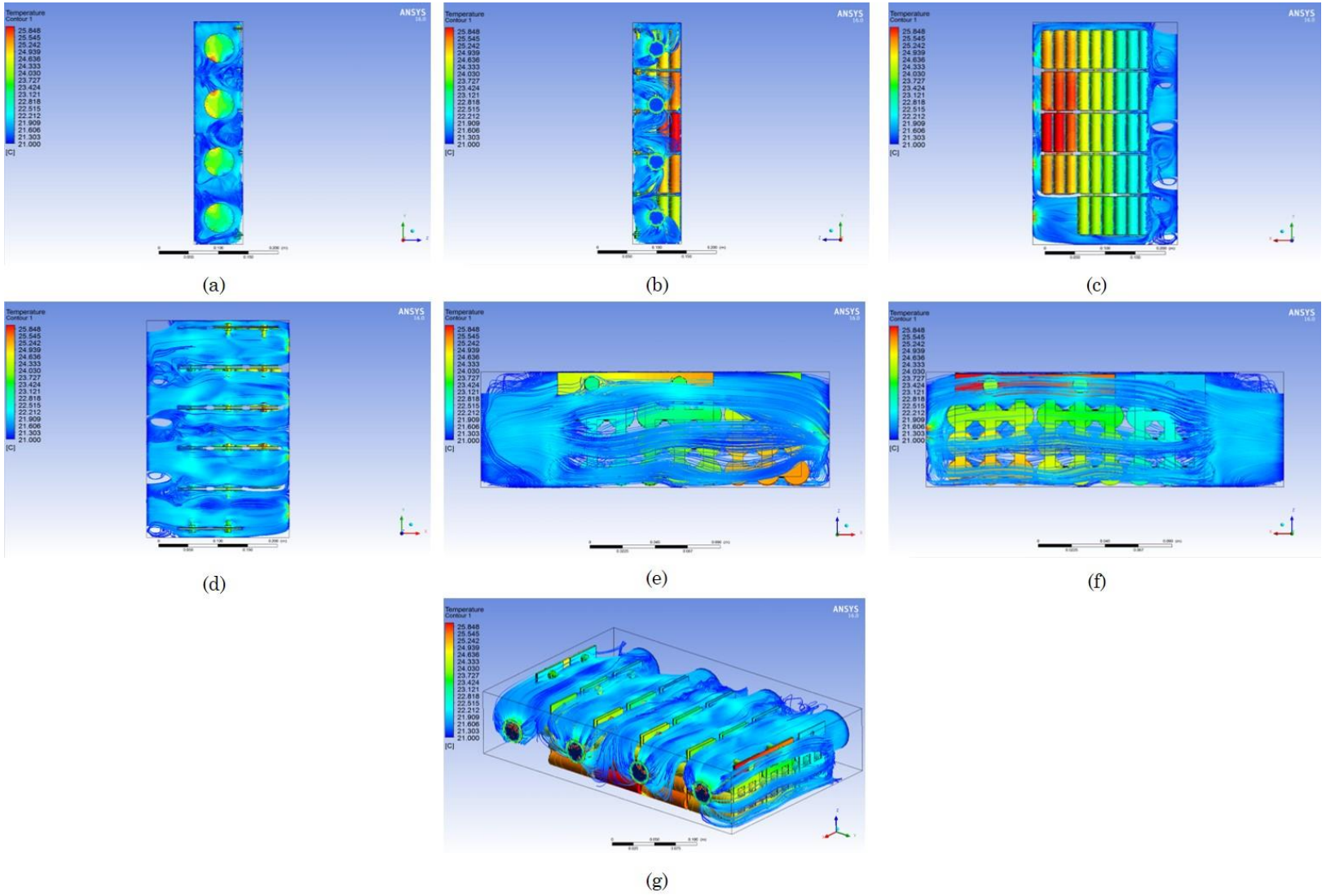

Figure 6-12. Thermal analysis of the 9th ESS enclosure design iteration with an inlet of 50 mm and outlet of 30 mm. (a) Inlet-view, (b) outlet-view, (c) base-view, (d) top-view, (e) rear-view, (f) front-view and (g) isometric-view of the ESS enclosure.

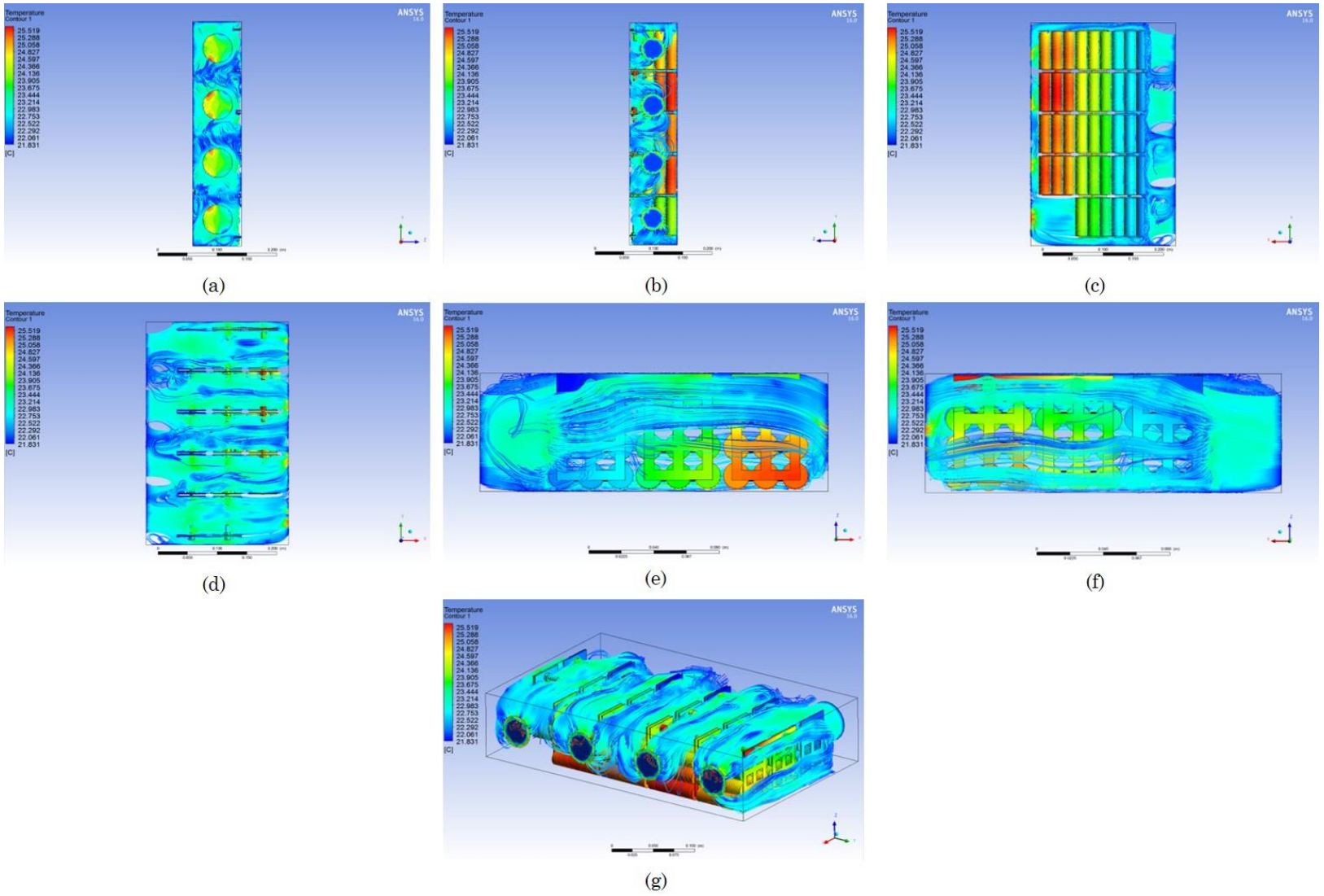

Figure 6-13. Thermal analysis of the 10th ESS enclosure design iteration with an inlet of 50 mm and outlet of 40 mm. (a) Inlet-view, (b) outlet-view, (c) base-view, (d) top-view, (e) rear-view, (f) front-view and (g) isometric-view of the ESS enclosure.

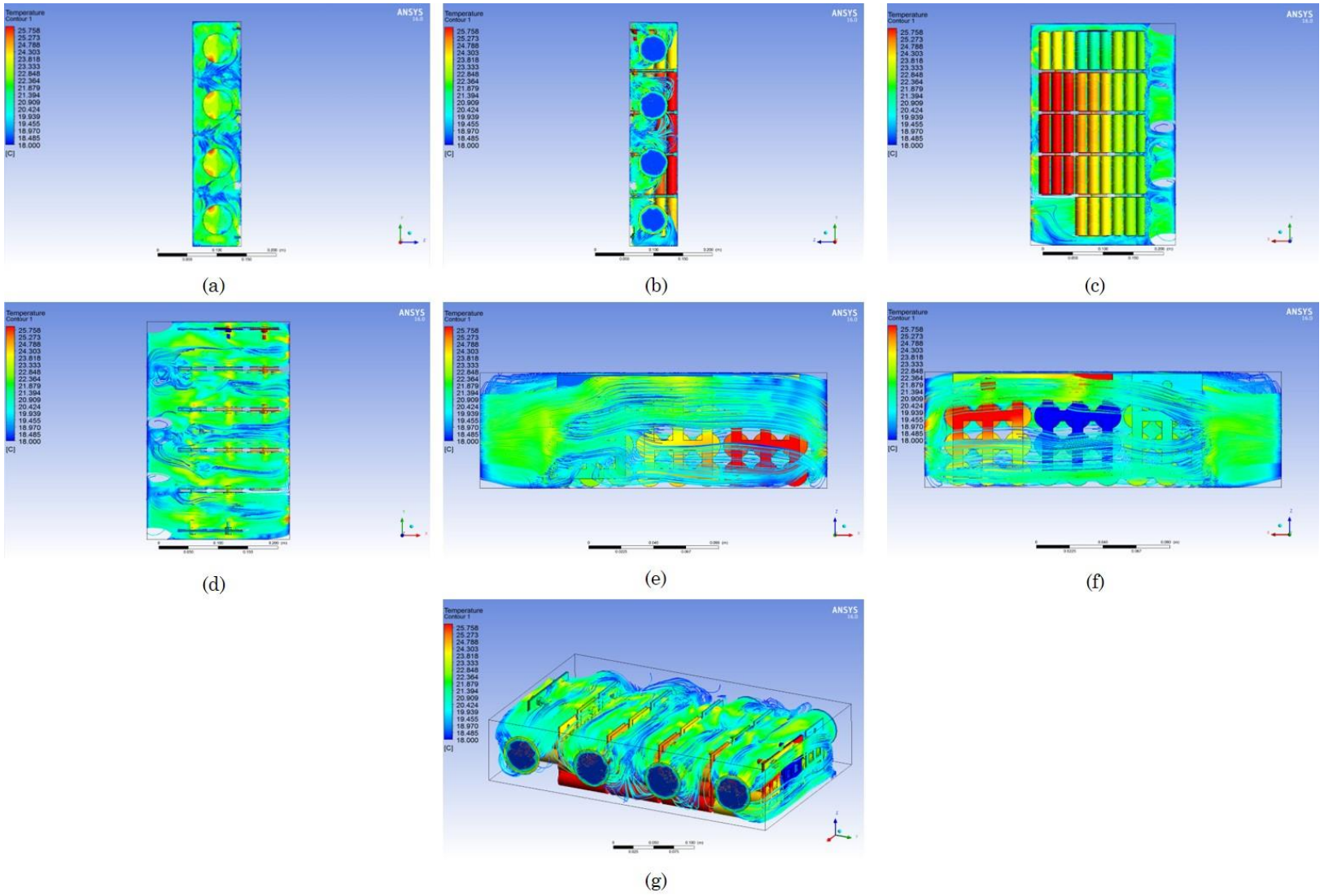

Figure 6-14. Thermal analysis of the 11th ESS enclosure design iteration with an inlet of 50 mm and outlet of 50 mm. (a) Inlet-view, (b) outlet-view, (c) base-view, (d) top-view, (e) rear-view, (f) front-view and (g) isometric-view of the ESS enclosure.

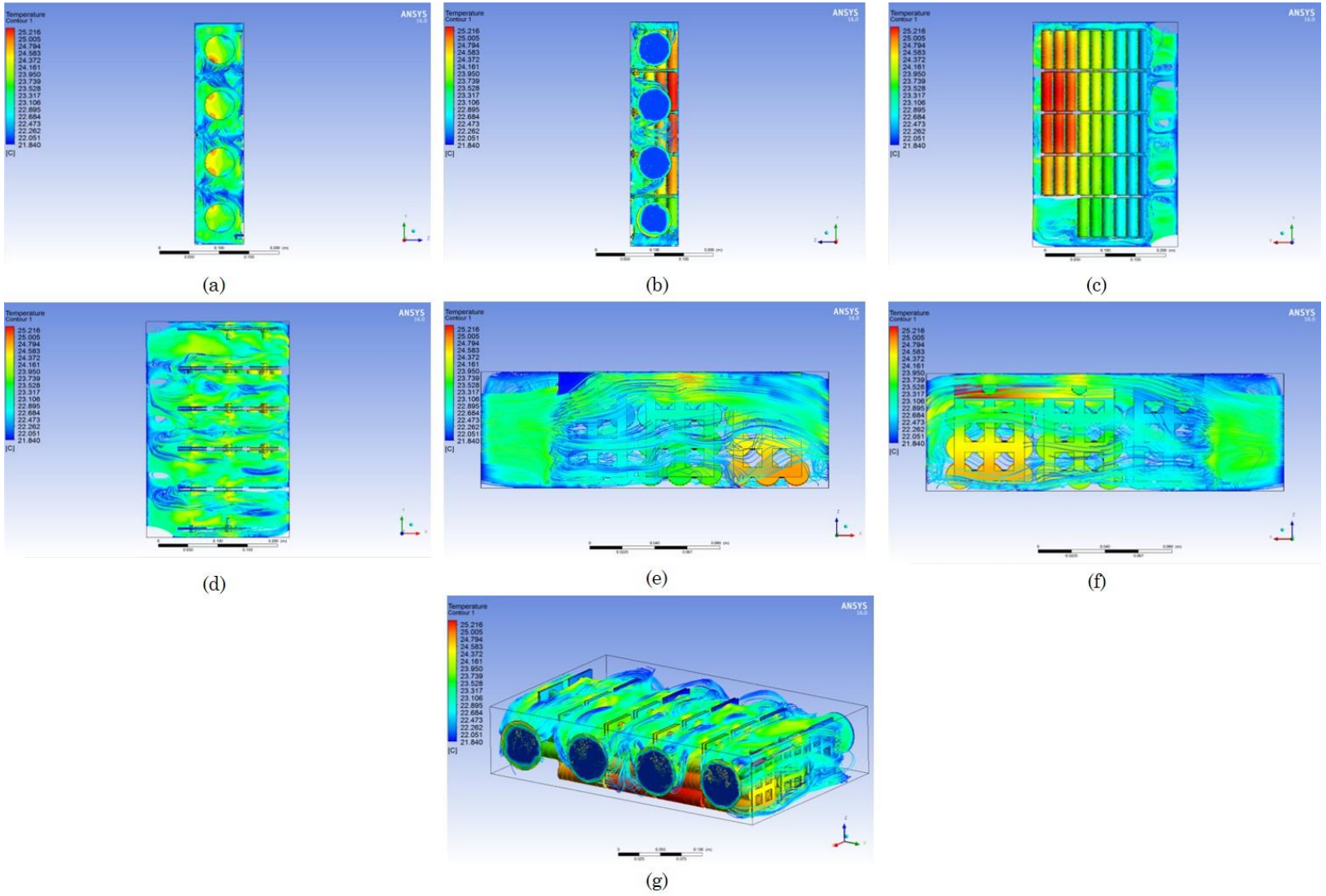

Figure 6-15. Thermal analysis of the 12th ESS enclosure design iteration with an inlet of 50 mm and outlet of 60 mm. (a) Inlet-view, (b) outlet-view, (c) base-view, (d) top-view, (e) rear-view, (f) front-view and (g) isometric-view of the ESS enclosure.

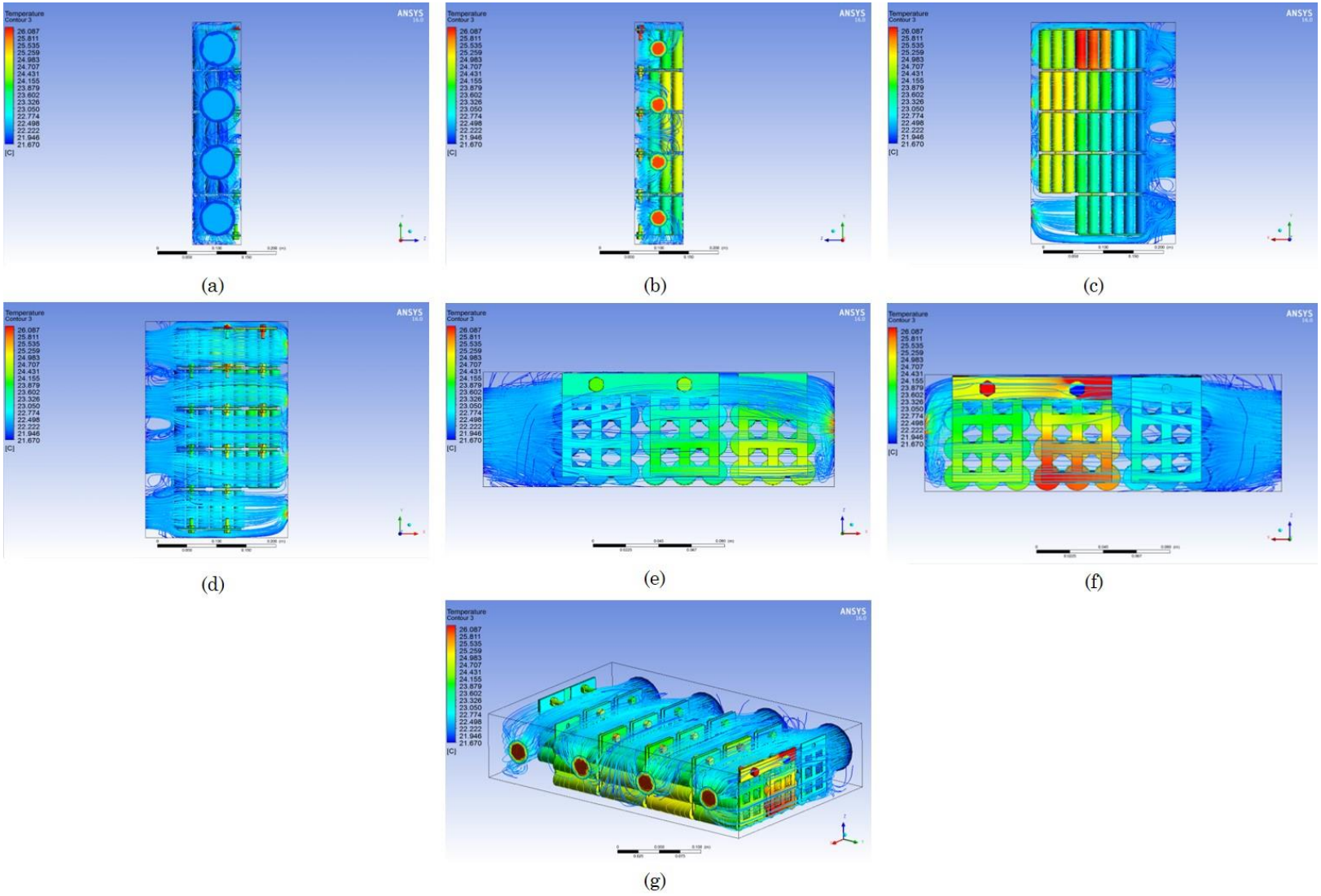

Figure 6-16. Thermal analysis of the 13th ESS enclosure design iteration with an inlet of 60 mm and outlet of 30 mm. (a) Inlet-view, (b) outlet-view, (c) base-view, (d) top-view, (e) rear-view, (f) front-view and (g) isometric-view of the ESS enclosure.

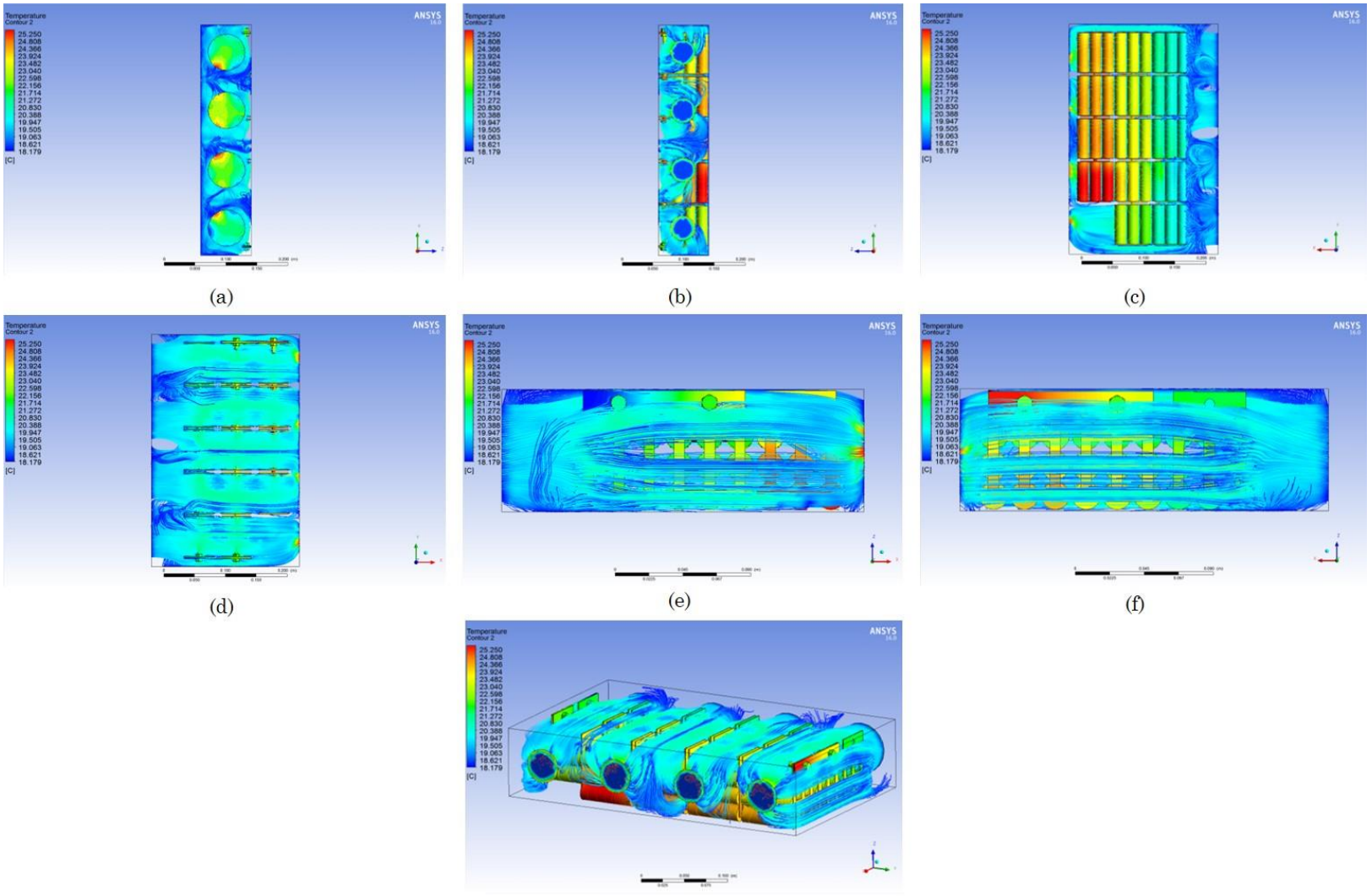

Figure 6-17. Thermal analysis of the 14th ESS enclosure design iteration with an inlet of 60 mm and outlet of 40 mm. (a) Inlet-view, (b) outlet-view, (c) base-view, (d) top-view, (e) rear-view, (f) front-view and (g) isometric-view of the ESS enclosure.

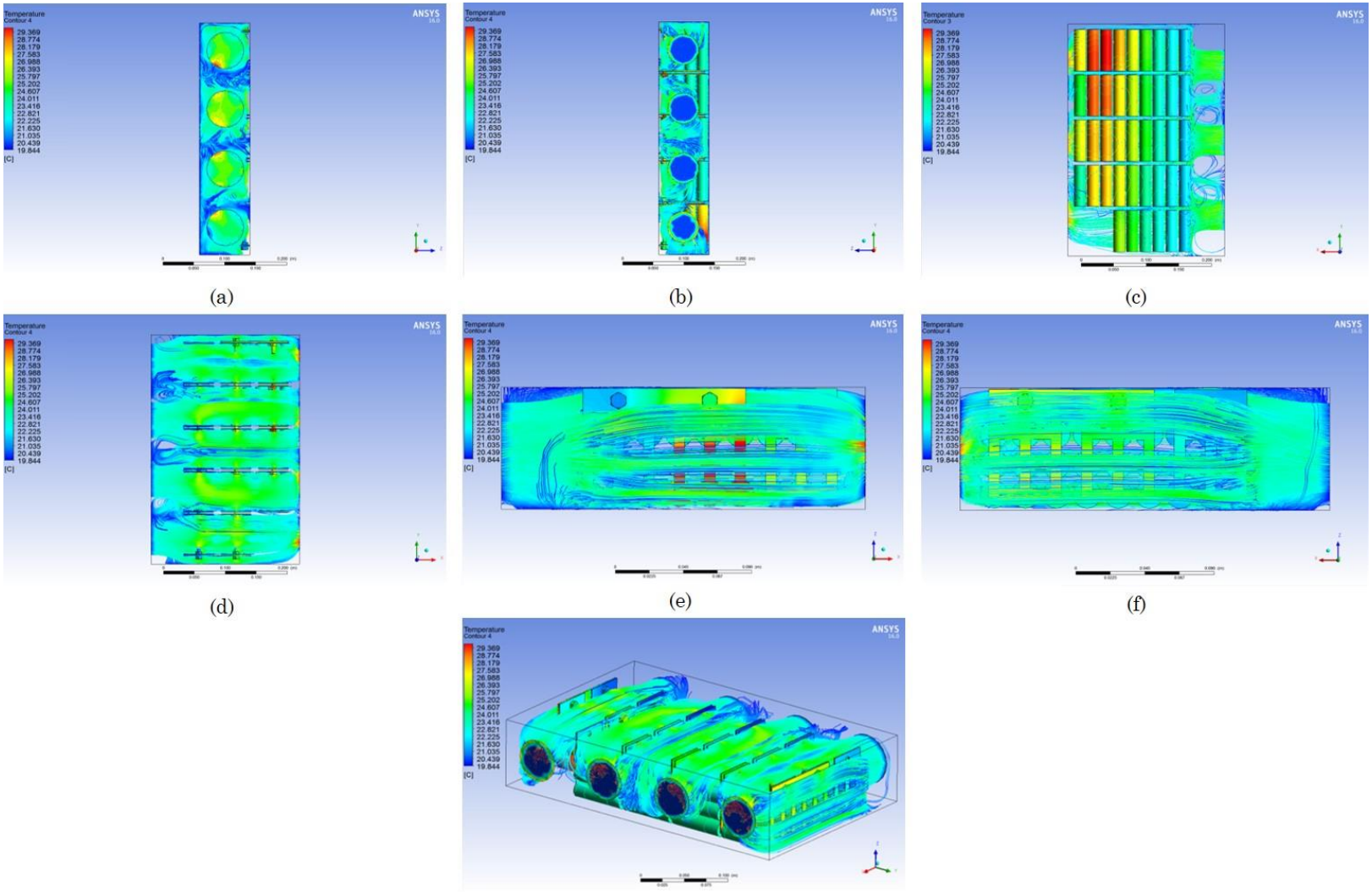

Figure 6-18. Thermal analysis of the 15th ESS enclosure design iteration with an inlet of 60 mm and outlet of 50 mm. (a) Inlet-view, (b) outlet-view, (c) base-view, (d) top-view, (e) rear-view, (f) front-view and (g) isometric-view of the ESS enclosure.

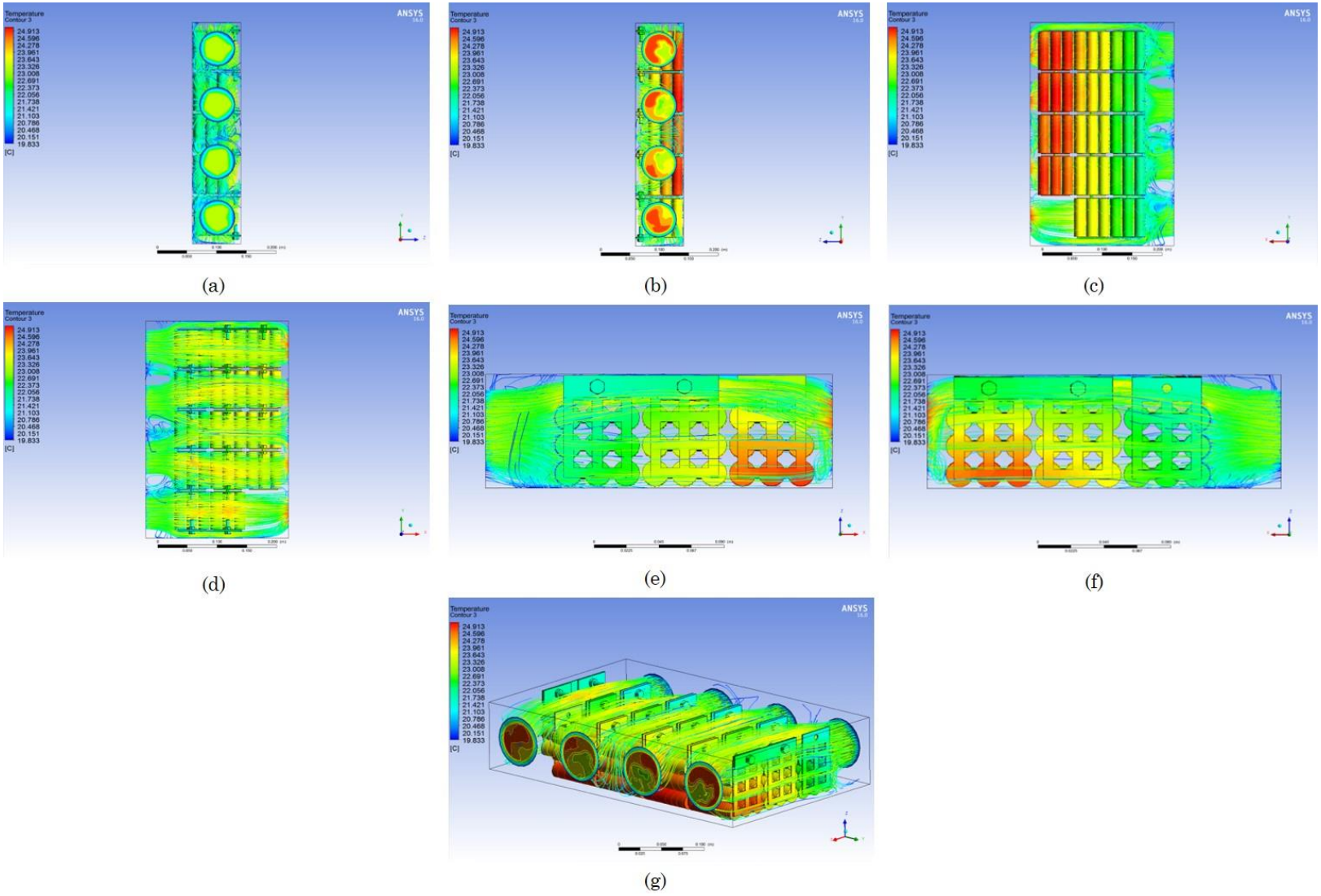

Figure 6-19. Thermal analysis of the 16th ESS enclosure design iteration with an inlet of 60 mm and outlet of 60 mm. (a) Inlet-view, (b) outlet-view, (c) base-view, (d) top-view, (e) rear-view, (f) front-view and (g) isometric-view of the ESS enclosure.

APPENDIX I - MECHANICAL DRAWINGS OF THE ESS ENCLOSURE'S BASE PLATE

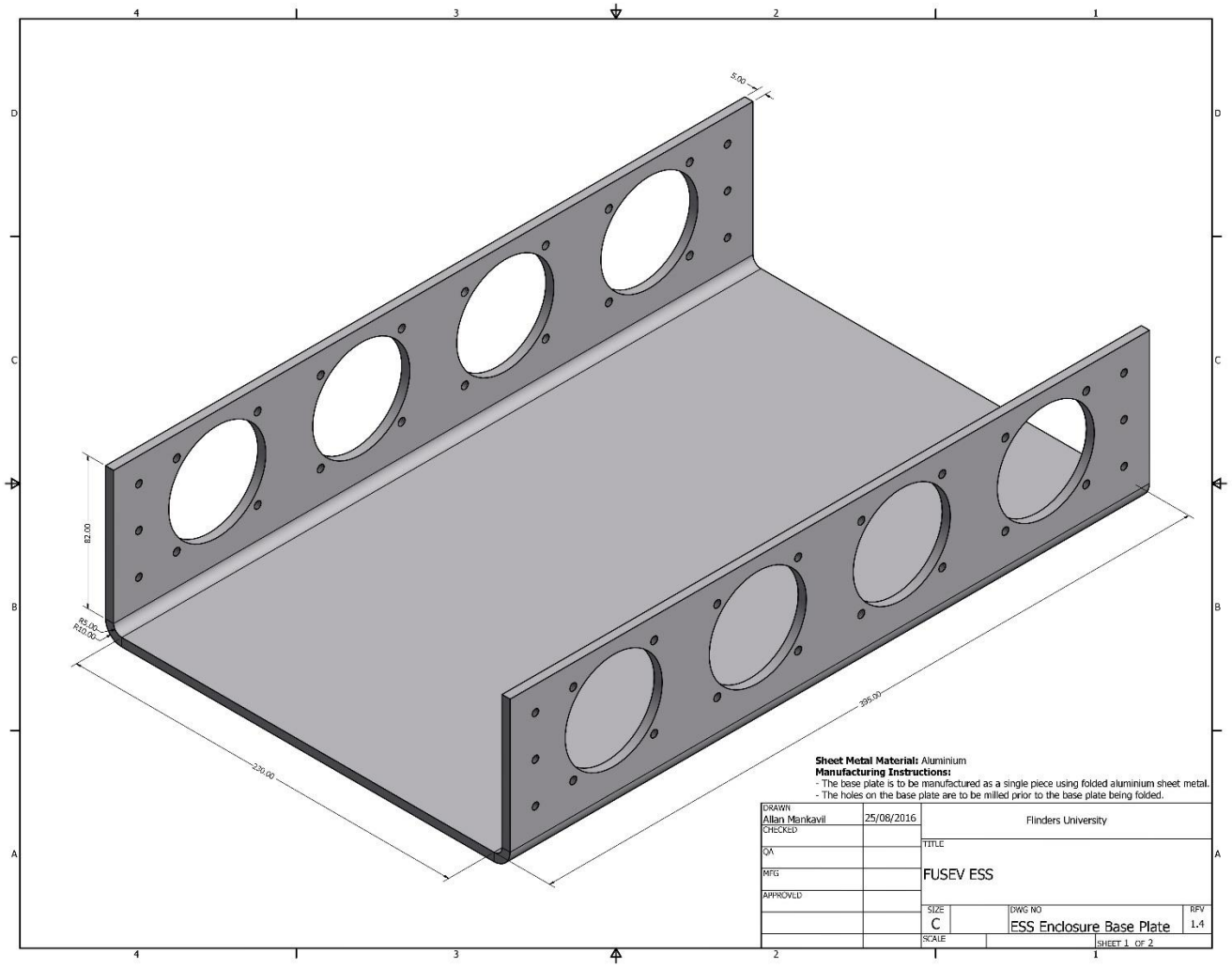

Figure 6-20. The mechanical drawing of the ESS Enclosure's folded Base Plate.

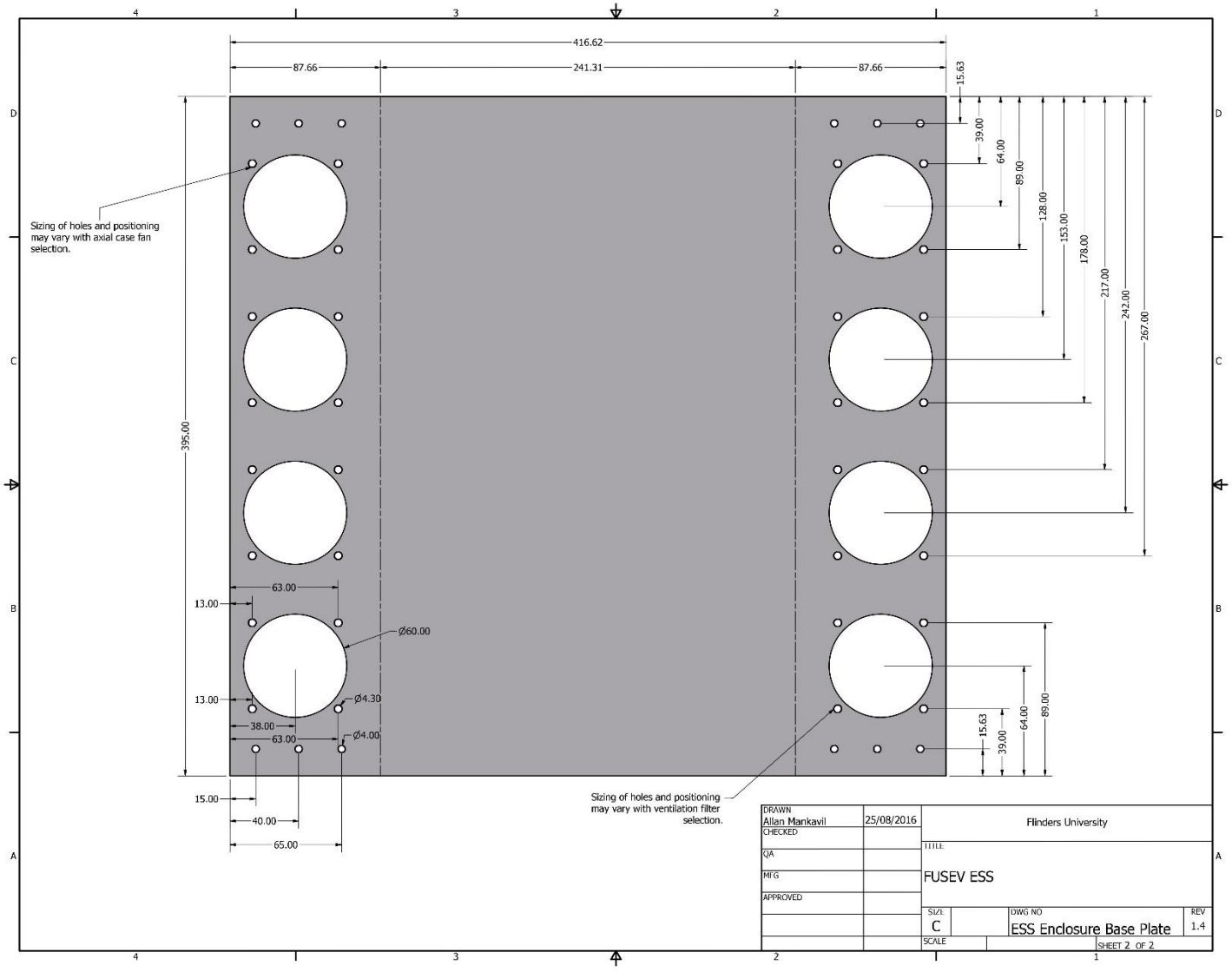

Figure 6-21. The mechanical drawing of the ESS Enclosure's unfolded Base Plate.

APPENDIX J - MECHANICAL DRAWINGS OF THE ESS ENCLOSURE'S REAR PLATE

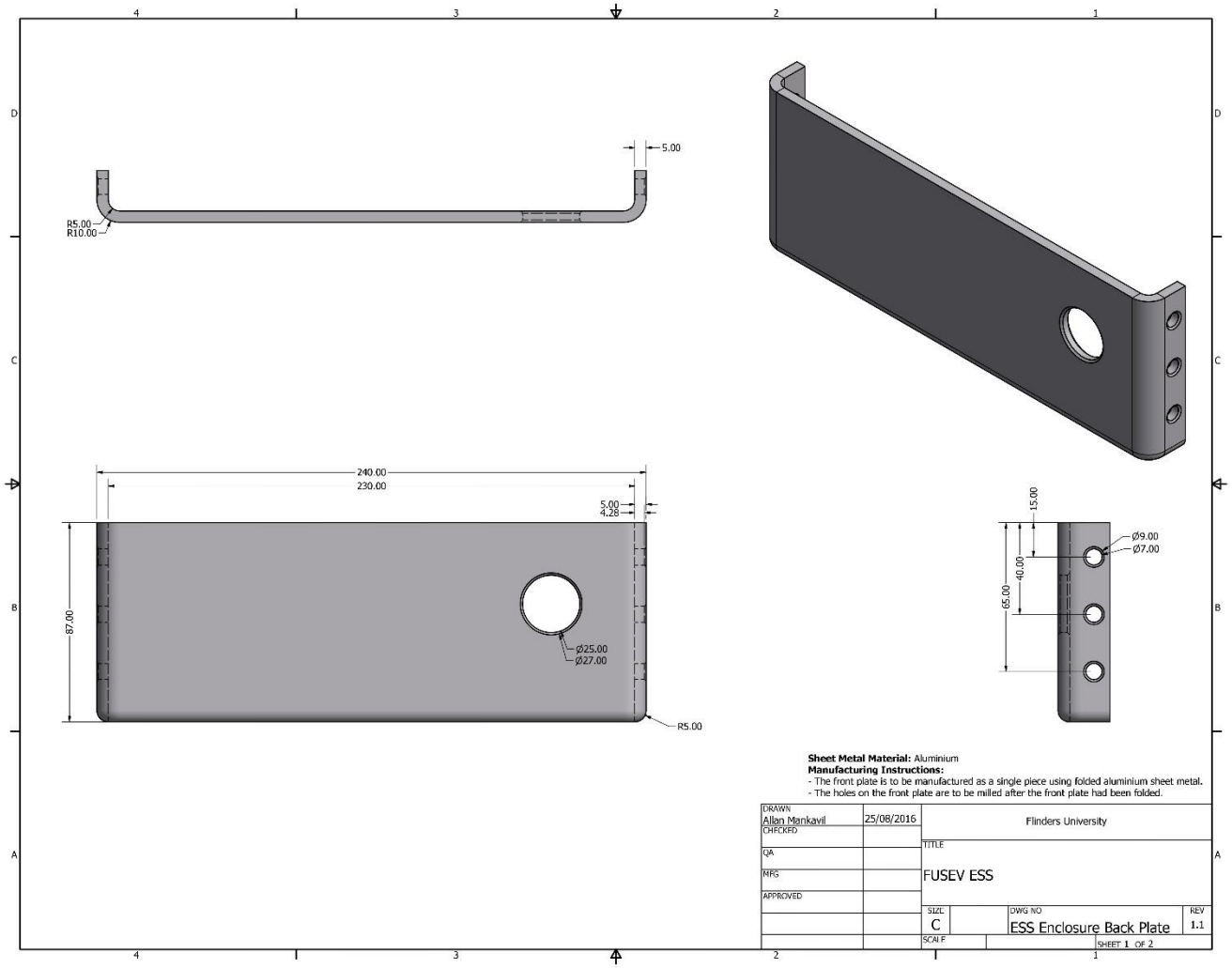

Figure 6-22. The mechanical drawing of the ESS Enclosure's folded Rear Plate.

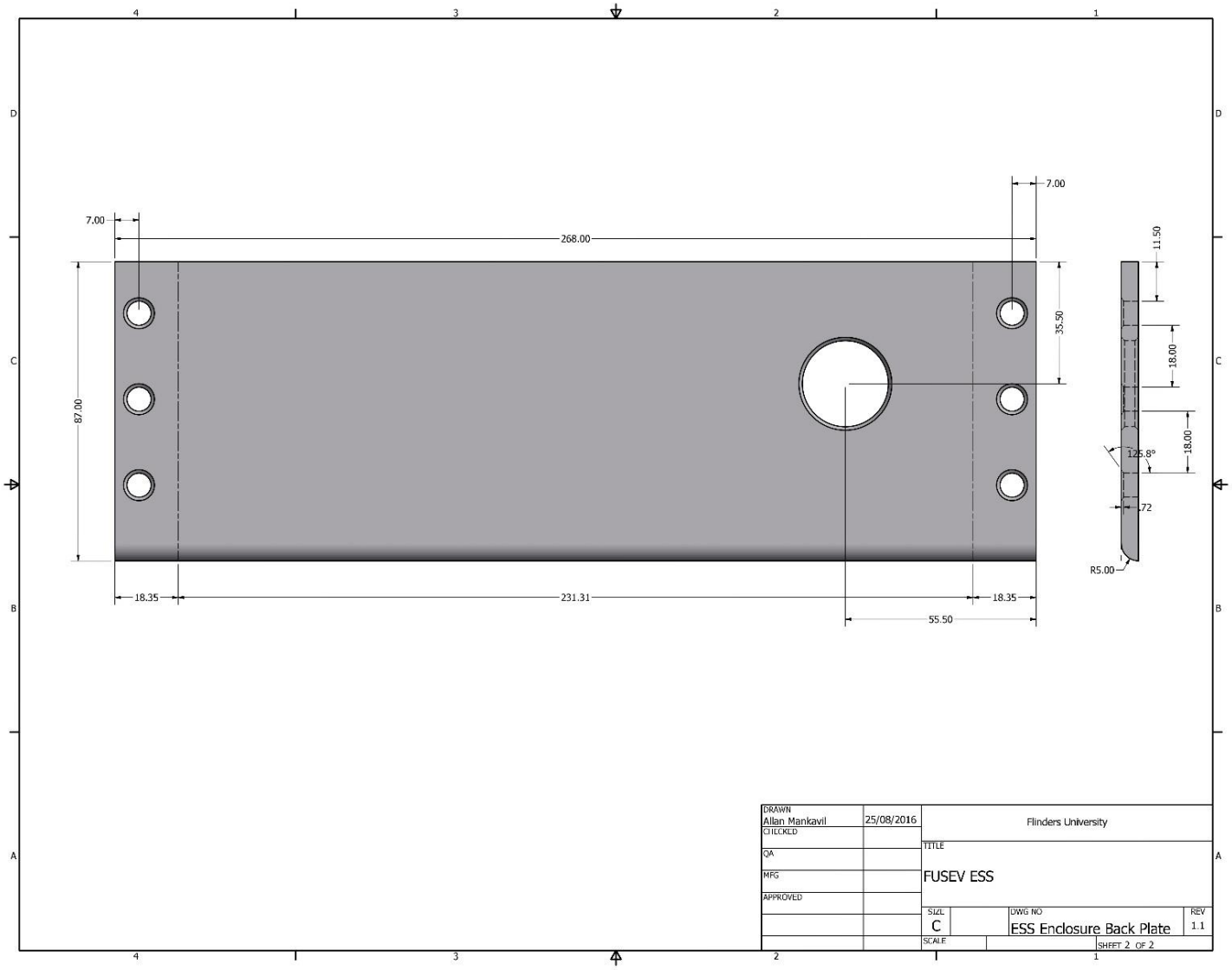

Figure 6-23. The mechanical drawing of the ESS Enclosure's unfolded Rear Plate.

APPENDIX K - MECHANICAL DRAWINGS OF THE ESS ENCLOSURE'S FRONT PLATE

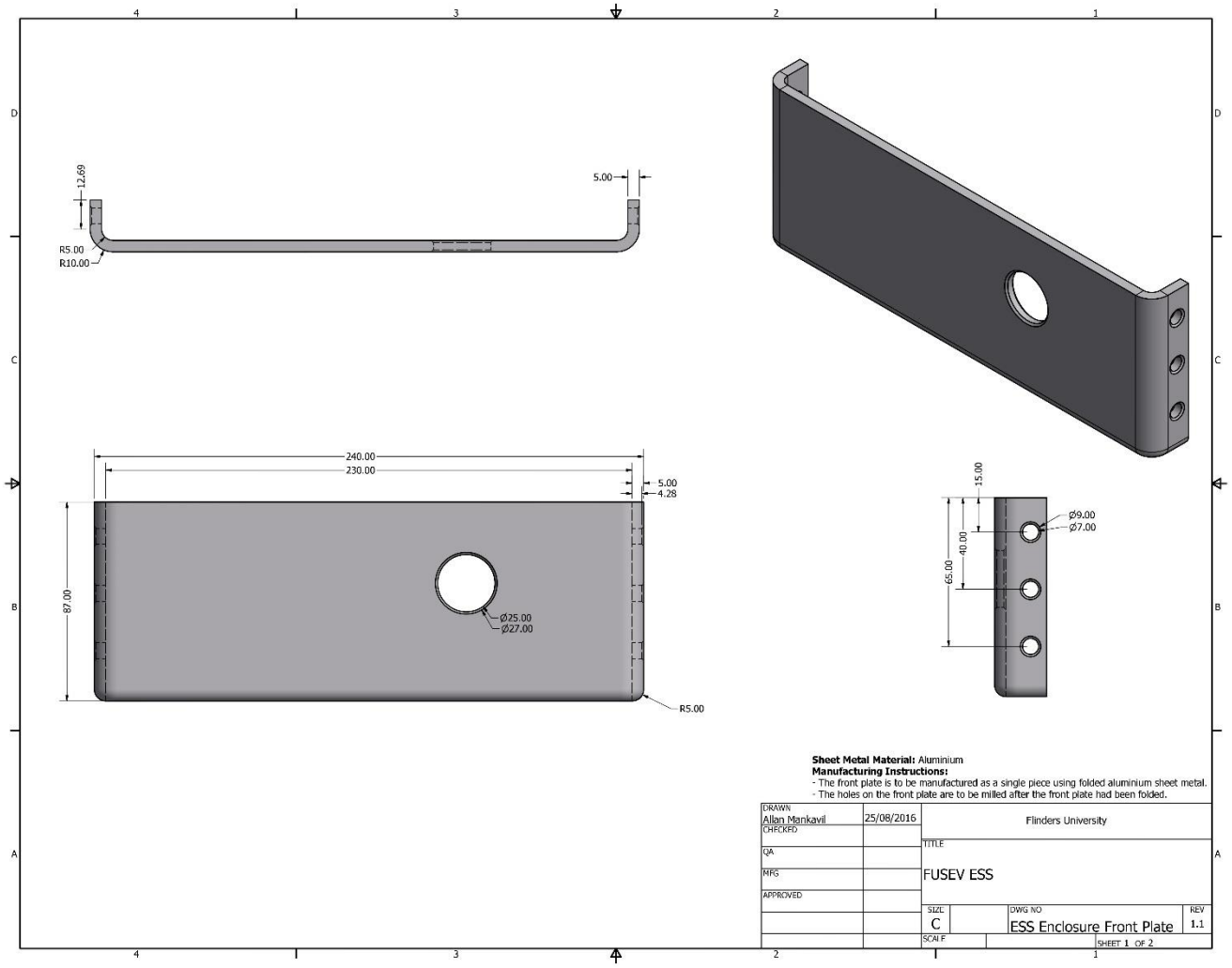

Figure 6-24. The mechanical drawing of the ESS Enclosure's folded Front Plate.

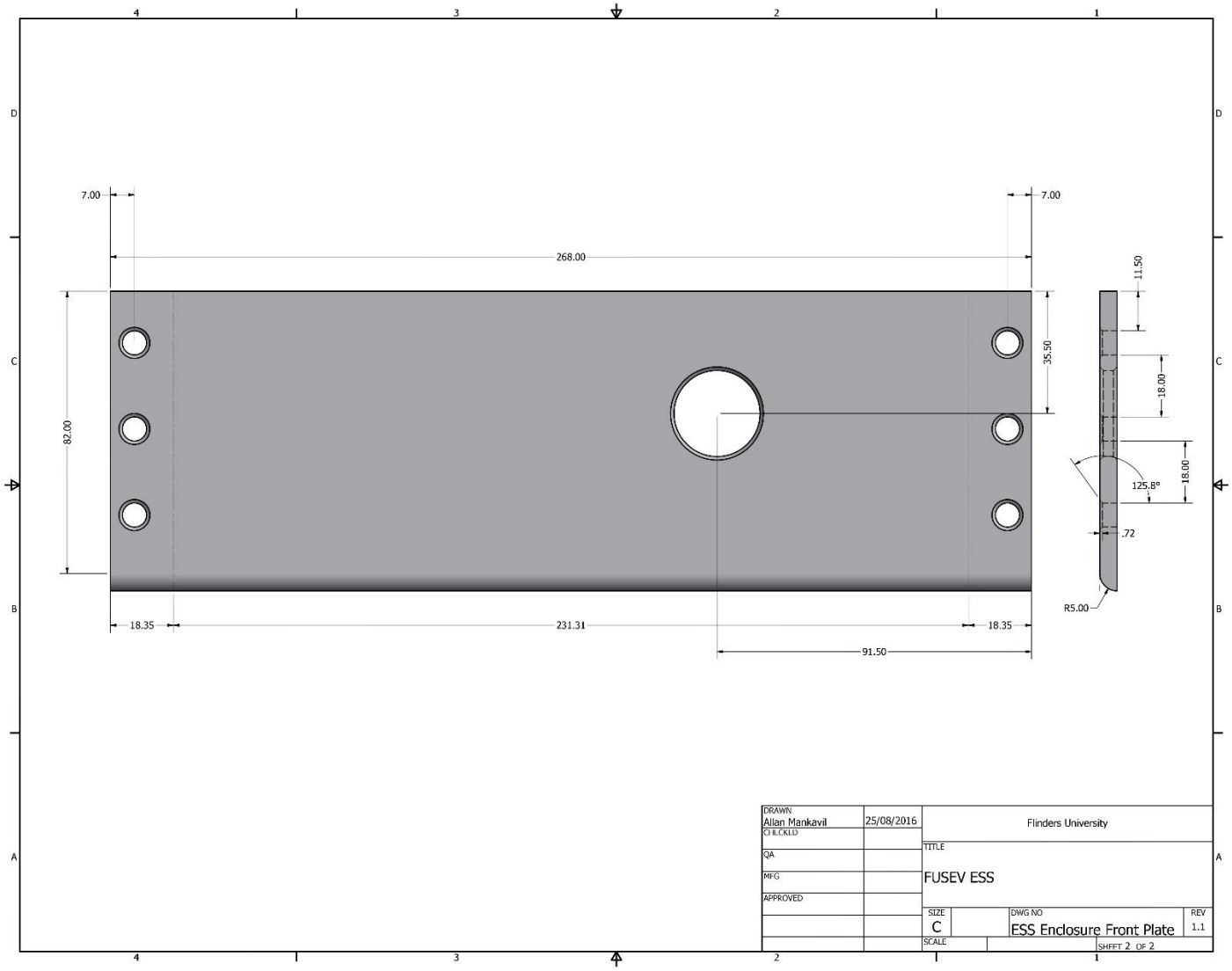

Figure 6-25. The mechanical drawing of the ESS Enclosure's unfolded Front Plate.

APPENDIX L - MECHANICAL DRAWINGS OF THE ESS ENCLOSURE'S TOP PLATE

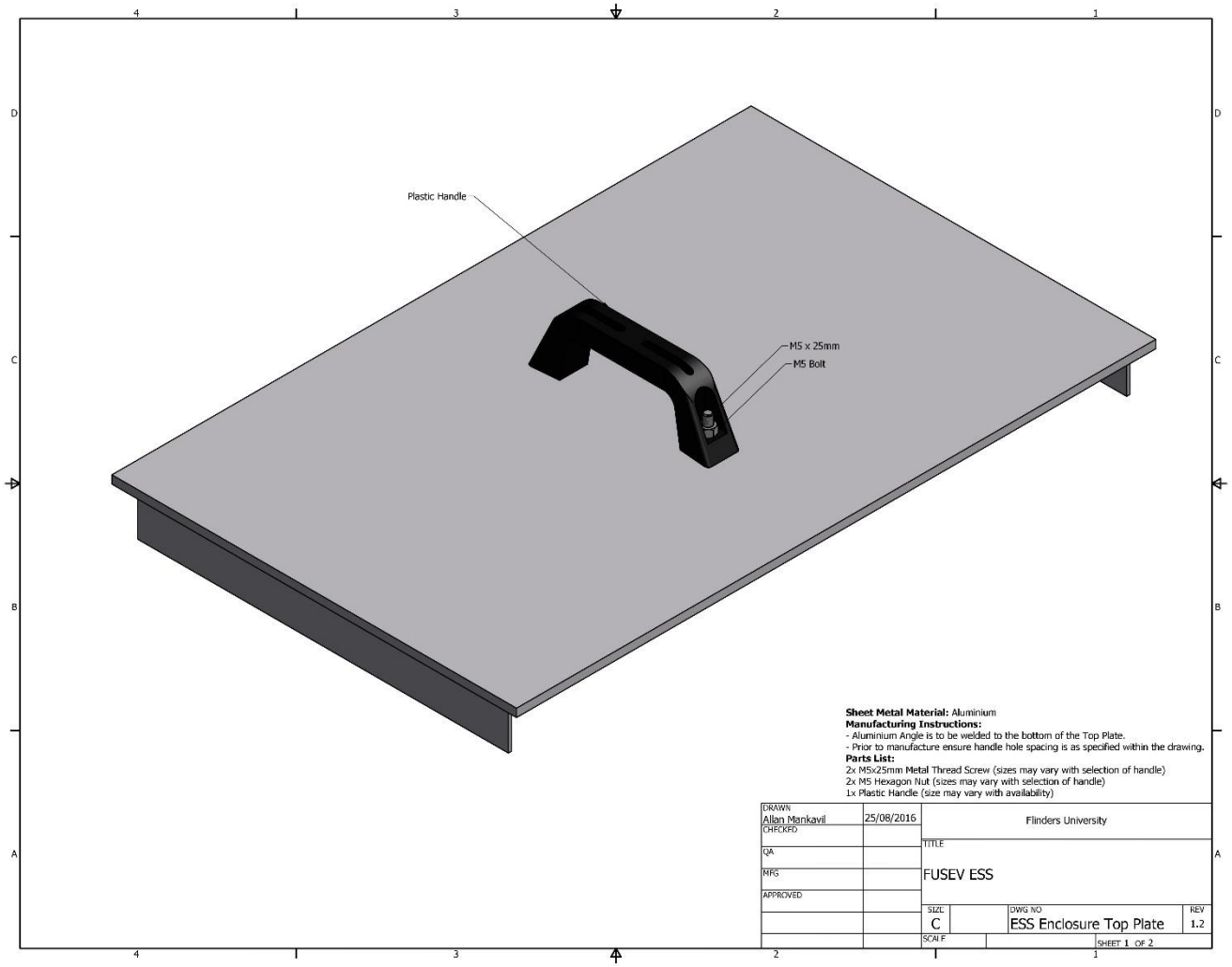

Figure 6-26. The mechanical drawing of the ESS Enclosure's Assembled Top Plate.

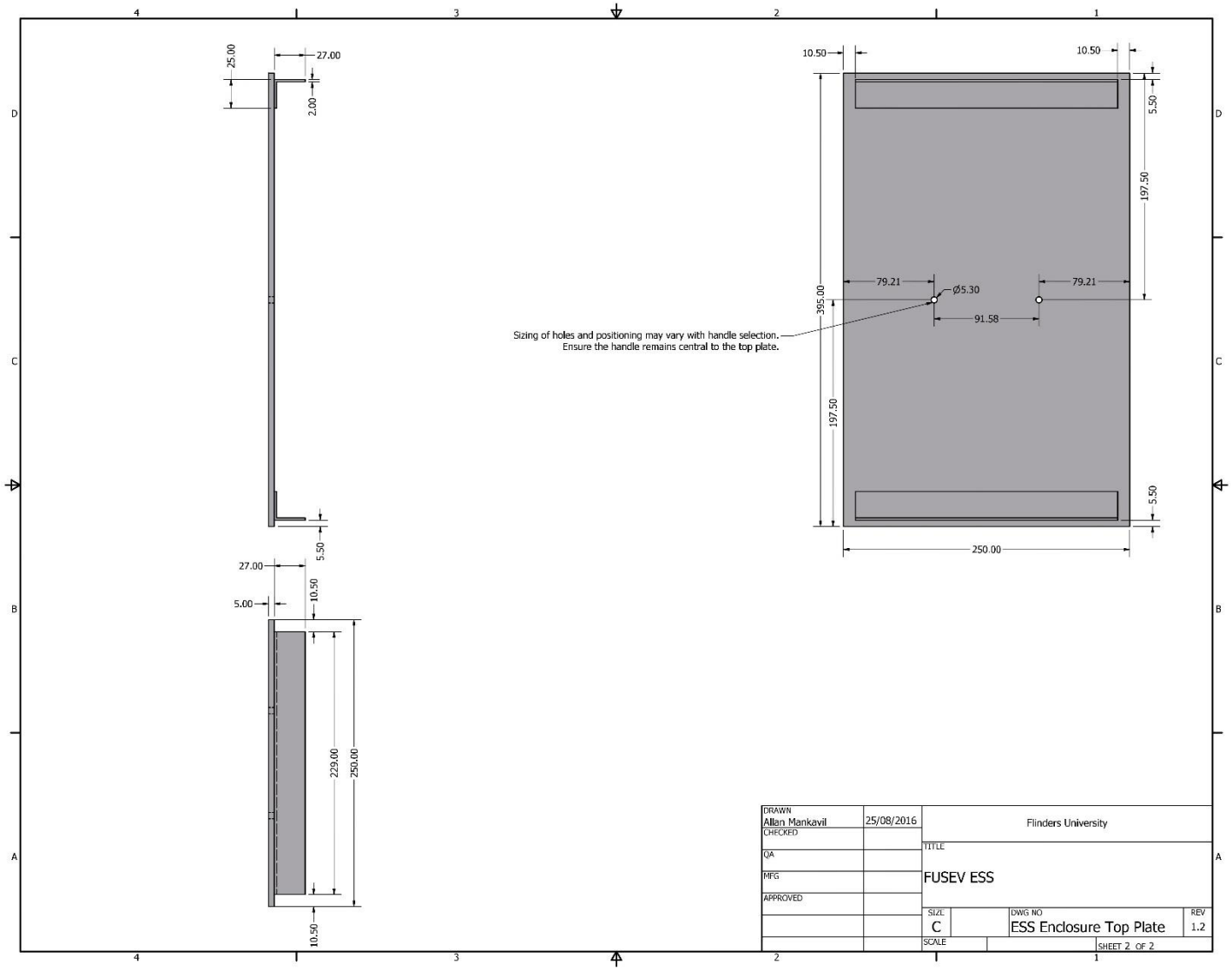

Figure 6-27. The mechanical drawing of the ESS Enclosure's Top Plate.

APPENDIX M - MECHANICAL DRAWINGS OF THE ASSEMBLED ESS ENCLOSURE

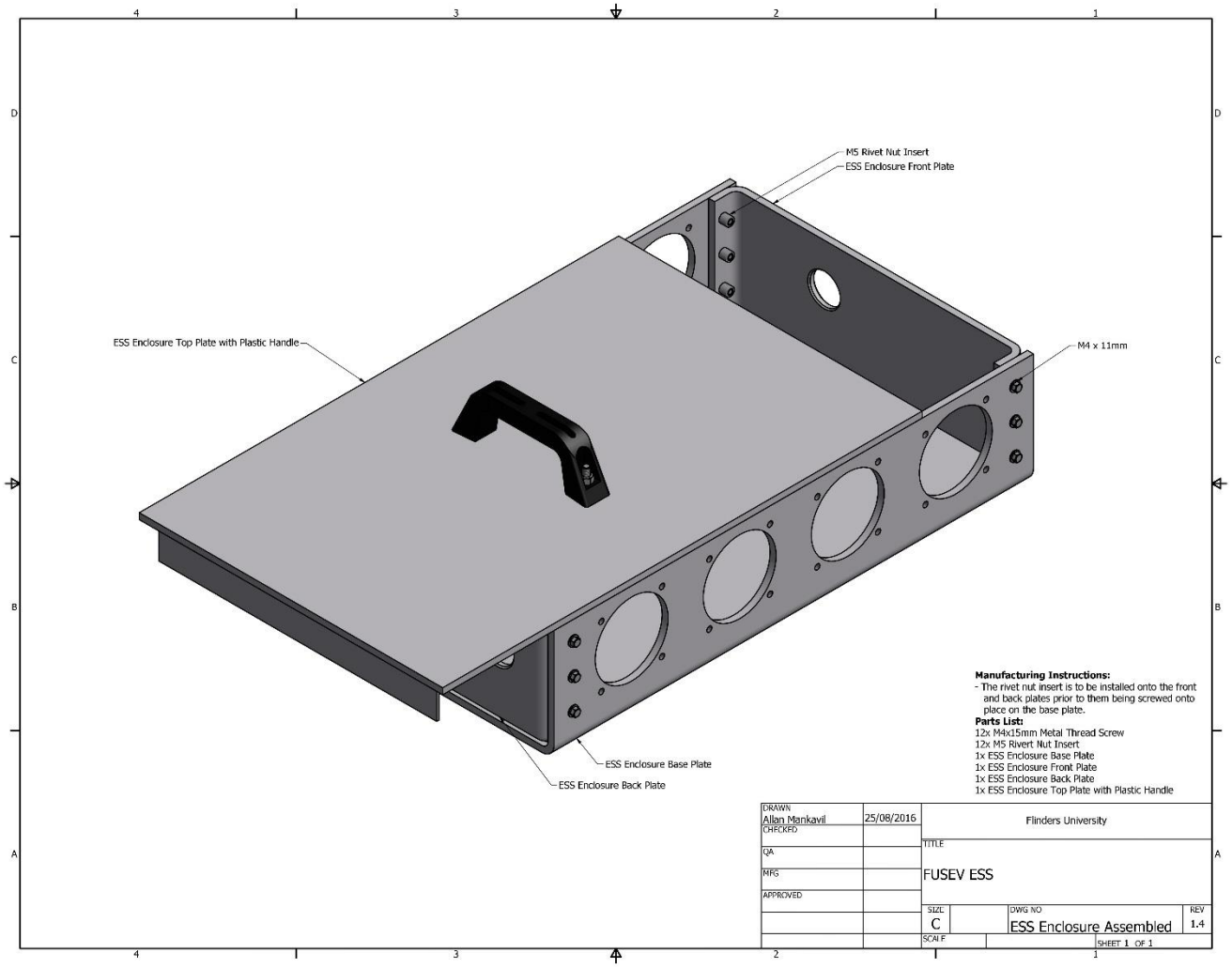

Figure 6-28. The mechanical drawing of the Assembled ESS Enclosure.

APPENDIX N - MECHANICAL DRAWINGS OF THE ASSEMBLED ESS WITH BARR AND FIXTURES

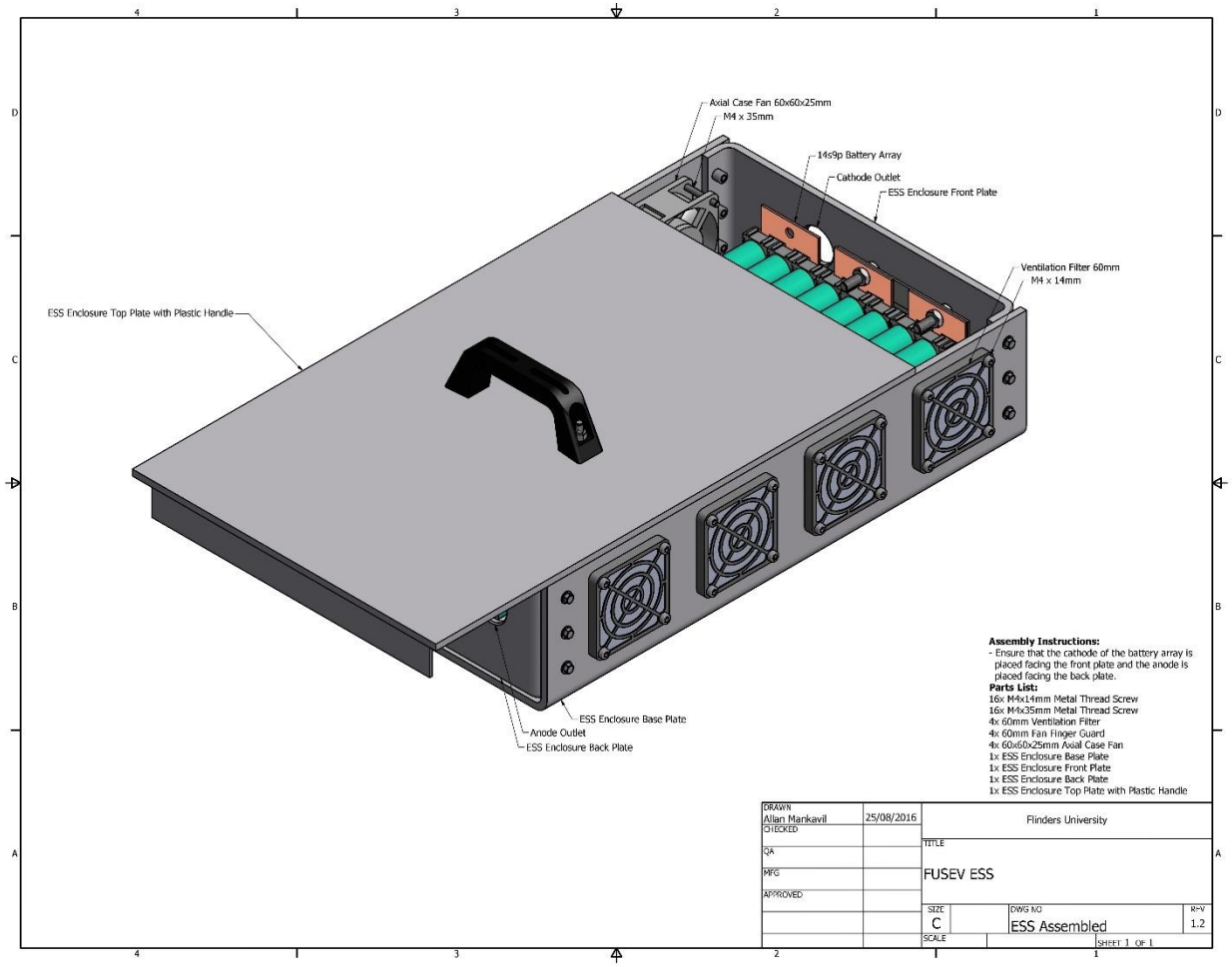

Figure 6-29. The mechanical drawing of the Assembled ESS Enclosure with BARR and Fixtures.

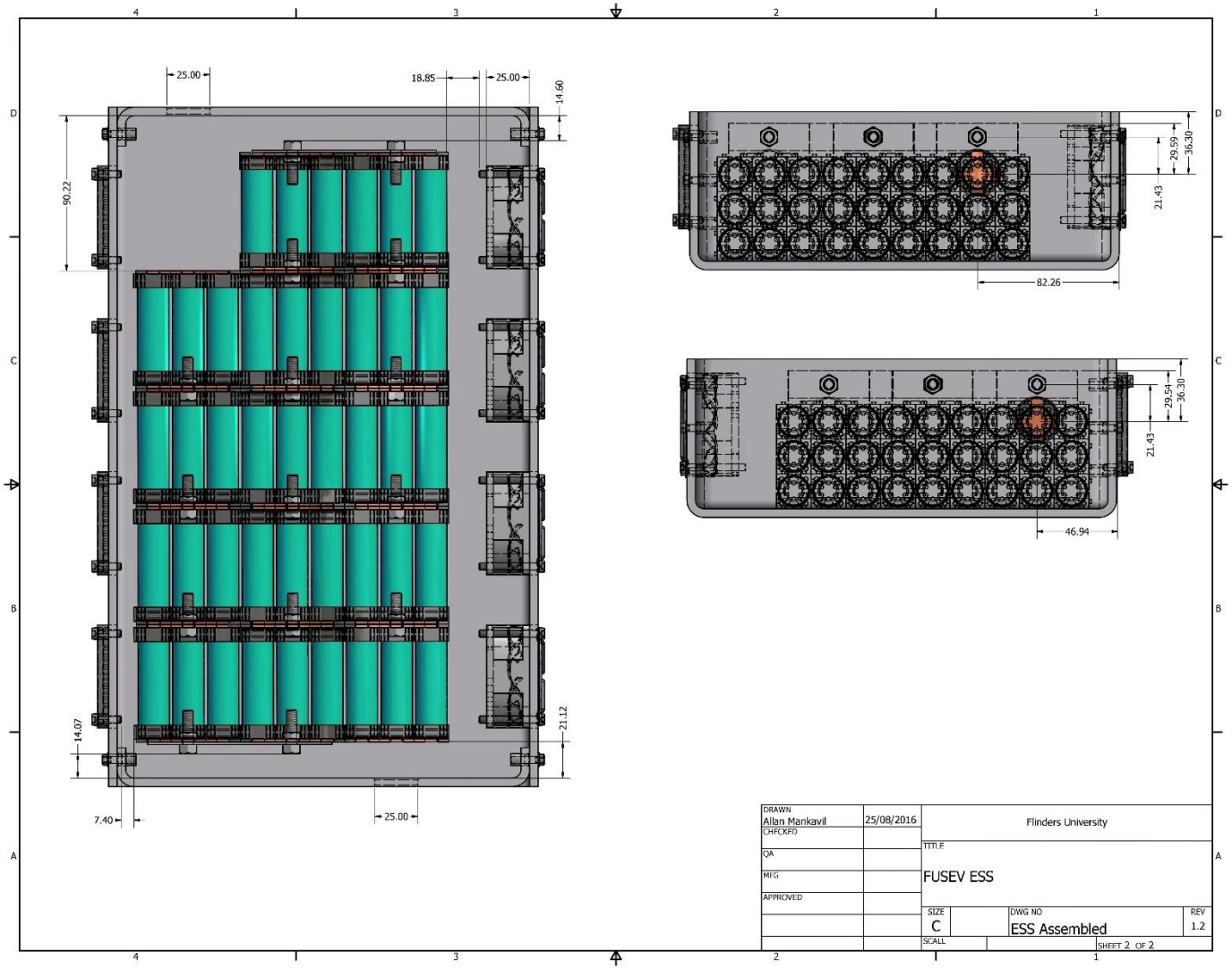

Figure 6-30. The mechanical drawing of the ESS Enclosure with BARR and Fixtures, showing internal component placement and installation.

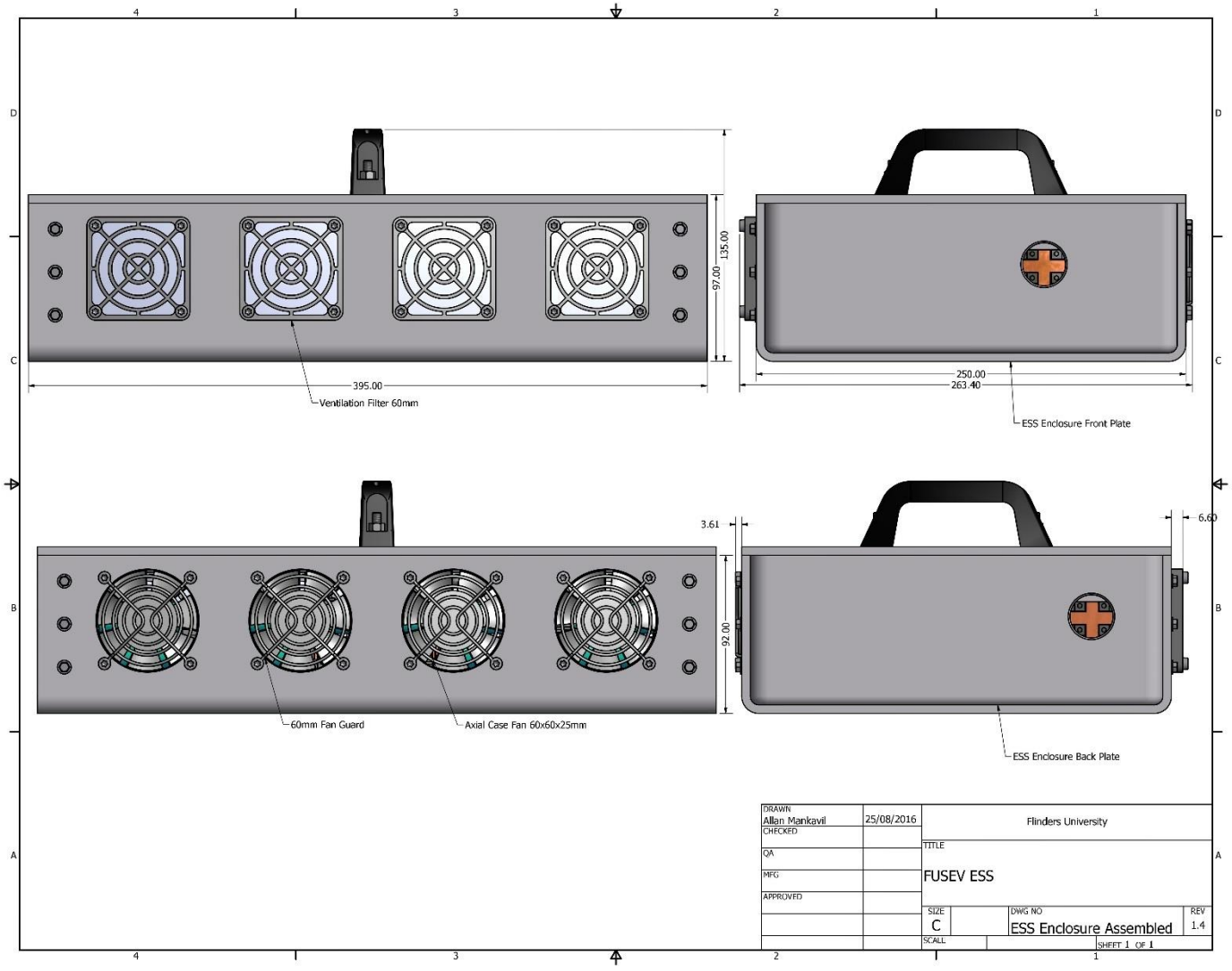

Figure 6-31. The mechanical drawing of the ESS Enclosure with BARR and Fixtures, showing external component placement and installation.